Heavy Flavor Dynamics in Relativistic Heavy-ion Collisions

by

Shanshan Cao

Department of Physics
Duke University

Date: _____

Approved:

_____
Steffen Bass, Supervisor

_____
Glenn Edwards

_____
Haiyan Gao

_____
Alfred Goshaw

_____
Berndt Müller

Dissertation submitted in partial fulfillment of the requirements for the degree of
Doctor of Philosophy in the Department of Physics
in the Graduate School of Duke University
2014

Abstract

Heavy Flavor Dynamics in Relativistic Heavy-ion Collisions

by

Shanshan Cao

Department of Physics
Duke University

Date: _____

Approved:

_____
Steffen Bass, Supervisor

_____
Glenn Edwards

_____
Haiyan Gao

_____
Alfred Goshaw

_____
Berndt Müller

An abstract of a dissertation submitted in partial fulfillment of the requirements for the degree of Doctor of Philosophy in the Department of Physics in the Graduate School of Duke University
2014

Abstract

Heavy flavor hadrons serve as valuable probes of the transport properties of the quark-gluon plasma (QGP) created in relativistic heavy-ion collisions. In this dissertation, we introduce a comprehensive framework that describes the full-time evolution of heavy flavor in heavy-ion collisions, including its initial production, in-medium evolution inside the QGP matter, hadronization process from heavy quarks to their respective mesonic bound states and the subsequent interactions between heavy mesons and the hadron gas.

The in-medium energy loss of heavy quarks is studied within the framework of a Langevin equation coupled to hydrodynamic models that simulate the space-time evolution of the hot and dense QGP matter. We improve the classical Langevin approach such that, apart from quasi-elastic scatterings between heavy quarks and the medium background, radiative energy loss is incorporated as well by treating gluon radiation as a recoil force term. The subsequent hadronization of emitted heavy quarks is simulated via a hybrid fragmentation plus recombination model. The propagation of produced heavy mesons in the hadronic phase is described using the ultra-relativistic quantum molecular dynamics (UrQMD) model. Our calculation shows that while collisional energy loss dominates the heavy quark motion inside the QGP in the low transverse momentum (p_{T}) regime, contributions from gluon radiation are found to be significant at high p_{T}. The recombination mechanism is important for the heavy flavor meson production at intermediate energies. The

hadronic final state interactions further enhance the suppression and the collective flow of heavy mesons we observe. Within our newly developed framework, we present numerical results for the nuclear modification and the elliptic flow of D mesons, which are consistent with measurements at both the CERN Large Hadron Collider (LHC) and the BNL Relativistic Heavy-Ion Collider (RHIC); predictions for B mesons are also provided.

In addition, various transport properties of heavy quarks are investigated within our numerical framework, such as the thermalization process of heavy quarks inside the QGP, and how the initial configuration of the QGP as well as its properties affect the final state spectra and the elliptic flow of heavy mesons and their decay electrons. The effects of initial state fluctuations in heavy-ion collisions are also studied and found to enhance the heavy quark energy loss in a (2+1)-dimensional boost invariant scenario. Furthermore, a new set of observables – heavy-flavor-tagged angular correlation functions – are explored and found to be potential candidates for distinguishing different energy loss mechanisms of heavy quarks inside the QGP.

Dedicated to my dear parents

Contents

List of Figures

Acknowledgements

First and foremost, I would like to thank my advisor Prof. Steffen Bass for his patient education and generous support for my study and research at Duke. He is not only a physicist but an artist as well who is able to present complicated scientific concepts in concise words and vivid pictures. And his passion and sense of humor keep an active and enjoyable working environment of our research group. Without his help, the accomplishment of this dissertation would be impossible.

Meanwhile, I am grateful to Prof. Berndt Müller. His broad knowledge and deep insight of this field provide me a great many helpful suggestions when I am in difficulties. And his encouragement and cultivation of independent thinking will definitely benefit my future research. Every discussion with him is inspiring and fruitful and I really regret not having grabbed even more opportunities to discuss with him over the past five years.

Apart from these two senior professors, the person I should thank most is Prof. Guang-You Qin, a former postdoc at Duke for three years. When I first came to this group, I knew almost nothing about either heavy-ion physics or computational programming and it is him who is always kind and patient to answer my questions and work together with me to build up this theoretical framework of heavy flavor step by step.

Furthermore, I sincerely thank our collaborators in the Ohio State University group – Prof. Ulrich Heinz, Prof. Hui-Chao Song, Dr. Zhi Qiu, and Dr. Chun Shen

– for teaching me knowledge of hydrodynamics and providing me their state-of-art numerical code of VISHnew which significantly speeds up my own study. And I also thank our collaborators in the Texas A&M group – Prof. Che Ming Ko, Prof. Rainer Fries and Kyong Chol Han – for helping me set up the model of heavy-light quark coalescence without which our framework would be incomplete. In fact, none of these cooperations would be so smooth and convenient without the existence of the JET Collaboration and I would like to express my thanks to it here.

I thank all of my former and current colleagues in the Duke QCD Group – Prof. Hannah Pertersen, Dr. Marlene Nahrgang, Dr. Nasser Demir, Dr. Hung-Ming Tsai, Dr. Christopher Coleman-Smith, Dr. Di-Lun Yang, Fritz Kretzschmar, Jonnah Bernhard, Scott Moreland, Xiao-Jun Yao and Ying-Ru Xu – for their generous help and enlightening discussions. Moreover, I am really fortunate to meet a large Chinese "family" at Duke that shares great experiences with me here. I would like to thank all the family members especially Jiani Huang, Yang Yang, Yu Song, Jun Yan and Chenglin Cao, without whom it would be much harder for me to survive the PhD life.

In the end, my most intense gratitude goes to my dear parents. It is their selfless love and support that make all my achievements here possible.

1

Introduction

Probably ever since the birth of mankind, people have been wondering who we are, where we are from and what the universe is composed of. It seems that we choose to believe the world is made of several simple elements despite its complicated outlook. Around the eighth century B.C., ancient oriental sages believed that the world is composed of five elements – gold, wood, water, fire and earth. About three hundred years later, the Greek philosophers Leucippus and Democritus proposed a more refined concept named "atoms" which are solid, homogeneous, indivisible, and unchangeable fundamental elements making up all the matter.

With the development of the modern science, nowadays it has been accepted that there exist 25 species of elementary particles: 6 quarks and 6 leptons that act as bricks of macroscopic matter; 12 bosons – photon, W^+, W^-, Z^0 and 8 different bi-colored gluons – that mediate the electroweak and strong forces between the bricks; and the most recently confirmed Higgs boson that is responsible for the generation of masses of all these elementary particles [1, 2, 3]. Meanwhile, the interactions between these elements are categorized into three fundamental forces: the *electromagnetic force* which satisfies $U(1)$ symmetry and is described by Quantum Electromagnetic

Dynamics (QED), the *weak force* which satisfies $SU(2)$ symmetry and can be unified with QED under $U(1) \times SU(2)$ symmetry – its spontaneous breaking plus the Higgs mechanism produce mass and yield the electroweak theory, and the *strong force* which satisfies $SU(3)$ symmetry and is described by Quantum Chromodynamics (QCD). This is the general picture of the "standard model" of particle physics today. Note that the strong force has not been successfully unified with the other two and gravity has not been included at the moment.

While QED has been very well studied and provided predictions that lead to an extremely precise (a precision of 10^{-8}) measurement of the fine structure constant α_{em} based on the anomalous magnetic dipole moment, QCD on the other hand, is much more complicated and the related calculations still remain largely unknown especially in the low energy region. In this dissertation, we would like to explore the properties of a particular type of QCD system that is extremely hot and dense and may exist in our early universe microseconds after the Big Bang. To investigate such nuclear matter on earth, we collide beams of ultrarelativistic heavy nuclei and observe the produced particles. In particular, we will utilize heavy quarks (charm and bottom quarks) to probe the properties of this QCD system and gain insights on both the mechanisms of the strong interaction and the evolution history of our infant universe.

1.1 Nuclear Matter under Extreme Conditions

1.1.1 The QCD Phase Diagram

QCD is an exact theory that governs the interactions between color charges (quarks and gluons) via the strong force. The two crucial properties of QCD are quark confinement and asymptotic freedom. Each quark carries a color, and quark confinement dictates that only color neutral particles can exist in vacuum, i.e., there is no free

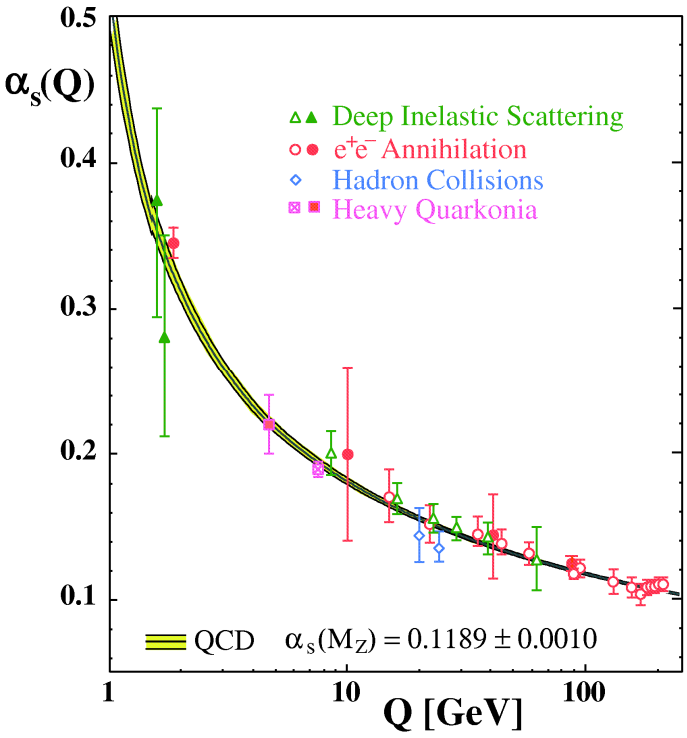

FIGURE 1.1: Measurements of the strong coupling constant α_s as a function of the energy scale Q. This figure is taken from Ref. [4].

quark. As shown by Eq.(1.1), to leading order in perturbative QCD (pQCD),

$$\alpha_s(k) \equiv \frac{g(k)^2}{4\pi} = \frac{4\pi}{11 - 2N_f/3} \left(\ln \frac{k^2}{\Lambda^2} \right)^{-1}, \tag{1.1}$$

the coupling strength of QCD is large at small scale of momentum transfer but becomes small with the increase of such momentum scale. This is known as the asymptotic freedom of QCD [5, 6]. Here, k denotes the momentum scale, N_f is the number of quark flavors and Λ is a constant fixed by experiment. Calculations to higher orders can be found in Refs. [7, 8]. In Fig.1.1 we show a summary of experimental measurements of this α_s taken from Ref. [4] in which open symbols represent the (resummed) next-to-leading order (NLO), and filled symbols next-to-NLO (NNLO) QCD calculations used in each analysis, compared with the QCD

predictions (shown by curves) for the combined world average value of $\alpha_s(M_{Z^0}) = 0.1189 \pm 0.0010$ ($M_{Z^0} = 91.1876 \pm 0.0021$ GeV), in 4-loop approximation and using 3-loop threshold matching at the pole masses of heavy quarks chosen as M_c =1.5 GeV and M_b = 4.7 GeV. For the calculations in the dissertation, we only keep α_s to leading order and the details of our parametrization are discussed in Appendix A.

As for all the dynamic systems, the information of QCD is encoded in its Lagrangian:

$$\mathcal{L}_{\mathrm{QCD}} = -\frac{1}{4} F^a_{\mu\nu} F^{\mu\nu}_a - \sum_f \bar{\psi}^f_\alpha \left(i\gamma^\mu \partial_\mu + m_f - g\gamma^\mu A_\mu \right)^{\alpha\beta} \psi^f_\beta, \tag{1.2}$$

in which

$$F^a_{\mu\nu} = \partial_\mu A^a_\nu - \partial_\nu A^a_\mu - g f^a_{bc} A^b_\mu A^c_\nu. \tag{1.3}$$

Here, A^a_μ represents a gluon field with color a, and ψ^f_α represents a quark field with flavor f and color α. μ, $\nu = 0, 1, 2, 3$ denote the Lorentz index. γ^μ's are the Dirac matrices, and $\bar{\psi} \equiv \psi^\dagger \gamma^0$. Finally, f^{abc} is the structure constant of $SU(3)$ Lie algebra, and m_f denotes quark mass. The coupling strength of the strong interaction g is a function of momentum transfer and can be evaluated perturbatively, such as the first order approximation given by Eq.(1.1).

With this QCD Lagrangian, the partition function of the strongly interacting system can be constructed as follows:

$$Z(T, V) = \int DAD\psi D\bar{\psi} \exp\left[-\int_V d^3x \int_0^{1/T} d\tau \mathcal{L}_{\mathrm{QCD}} \left(A, \psi, \bar{\psi} \right) \right], \tag{1.4}$$

where $\tau \equiv i x_0$ is the imaginary time and is integrated over from zero to the inverse of the temperature parameter. The calculation of this integral can be carried out on a lattice via numerical technics, which is known as lattice QCD [9]. With a proper calculation of the partition function, the thermodynamic quantities of the system

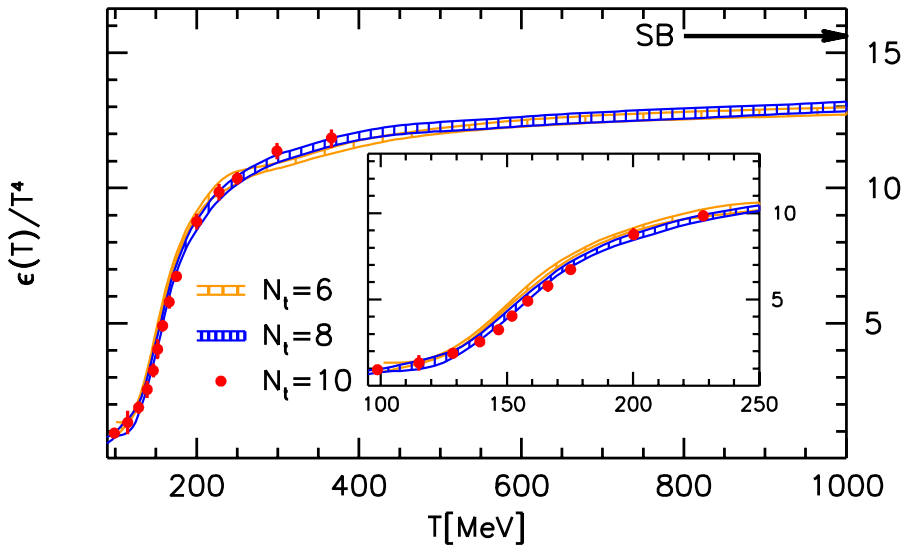

FIGURE 1.2: Equation of state calculated by Lattice QCD: energy density normalized by T^4 vs. T on $N_t = 6, 8$ and 10 lattices. The arrow represents the Stefan-Boltzmann limit $\epsilon_{SB} = 3p_{SB}$. This figure is taken from Ref. [9].

can be obtained. For instance, we have energy density and pressure as follows:

$$\epsilon = \frac{T^2}{V}\left(\frac{\partial \ln Z}{\partial T}\right)_V, \qquad P = T\left(\frac{\partial \ln Z}{\partial V}\right)_T. \tag{1.5}$$

In Fig.1.2 we show the energy density normalized by T^4 as a function of temperature obtained from a lattice QCD calculation [9]. The comparison between $N_t = 6$, 8 and 10 verifies the convergence of the numerical integral of Eq.(1.4) on the lattice with a discretization of 6 points in the temperature direction. The spatial part of Eq.(1.4) is discretized with at least $18 \times 18 \times 18$ lattice points. In Fig.1.2 one observes a rapid increase of the energy density of matter around a critical temperature of T_c =160 MeV. Meanwhile, if we were to model QCD matter as a non-interacting ultra-relativistic boson gas, thermodynamic calculation yields an equation of state as $\epsilon = g_{\rm DOF}\pi^2 T^4/30$. This is known as the Stefan-Boltzmann formula, in which $g_{\rm DOF}$ denotes the degree of freedom of the constituent particles. Therefore, the lattice result

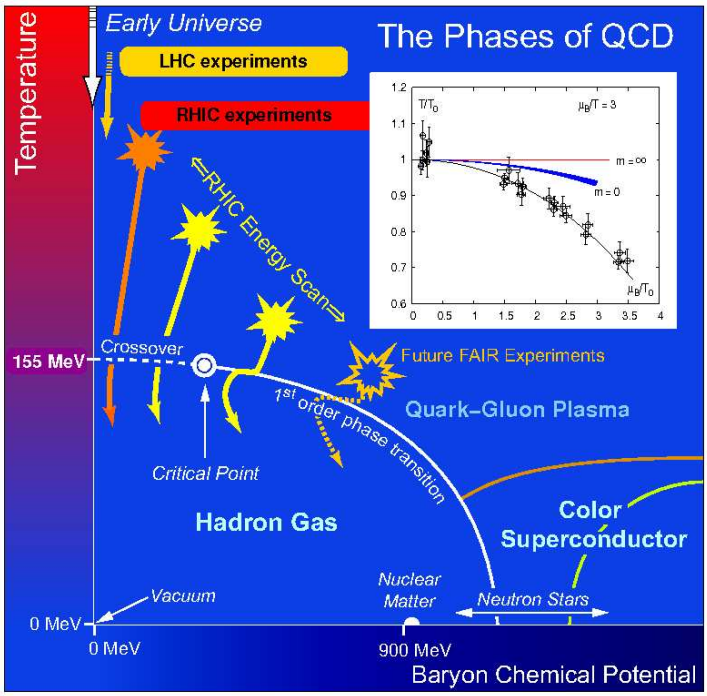

FIGURE 1.3: Illustration of the QCD phase diagram. The credit of this figure belongs to the USQCD website and 2007 NSAC report.

shown in Fig.1.2 implies a quick rise of the intrinsic degrees of freedom of the QCD system around T_c which corresponds to a fast cross-over from one state of matter to another. In fact, the lattice result is in good agreement with the Stefan-Boltzmann approximation if one assumes a hadron resonance gas for the nuclear matter below T_c and a quark-gluon gas above T_c. Thus the critical temperature T_c corresponds to a boundary between a hadron gas and a color-deconfined state of quarks and gluons which is termed as a quark-gluon plasma (QGP) [10].

In Fig.1.3, we show an illustration of the QCD phase diagram labeled with energy regimes explored by different experiments. There are three major states for the QCD system. At low baryon chemical potential μ and low temperature T, the QCD matter exists in the form of hadron gas in which the quarks and gluons are confined

inside hadrons. With an increase of temperature and density, the nuclear matter will transition into a color-deconfined quark-gluon plasma state. Note that there exists a critical point in the phase diagram, above which the transition from the hadronic state to the QGP state is an ordinary first order phase transition, but below that it is a fast cross-over without classical critical behavior. Details of the difference between cross-over and rigorous phase transition are reflected by the behavior of the order parameters like the Polyakov loop and the effective quark mass as discussed in [11]. Note that the search for the location of the critical point is one of the most important tasks of the beam energy scan experiment at RHIC and exciting results are expected in the next few years. Apart from the hadronic state and the quark-gluon plasma state, another interesting state of a QCD system is that of a color superconductor which resides in the large chemical potential region at low temperature. In this regime, color charges, like quarks and gluons, can form cooper pairs and stop from being scattered by the lattice, just as normal electric charges do to form a normal superconductor. However, unlike the repulsive Coulomb force between electrons in a metal, the strong interaction between color charges is already attractive, and therefore, phonons – due to the charge-lattice interaction – are not necessary for the formation of cooper pairs inside a QCD system. This in fact makes superconductivity in QCD more "robust" than that in metals in the sense that (1) for extremely dense QCD matter where perturbative approach is applicable one may derive the gap parameter and other properties of color superconducting quark matter rigorously and (2) the ratio of the gap parameter to the Fermi energy in a strongly interacting QCD matter could be much larger than that in conventional BCS superconducting metals [12]. However, the temperature of this state should be low enough so that the bound state of color charge pairs are not destroyed by thermal fluctuations. This color-superconducting state is beyond the current capabilities of experimental observation in laboratories and might be studied via neutron stars.

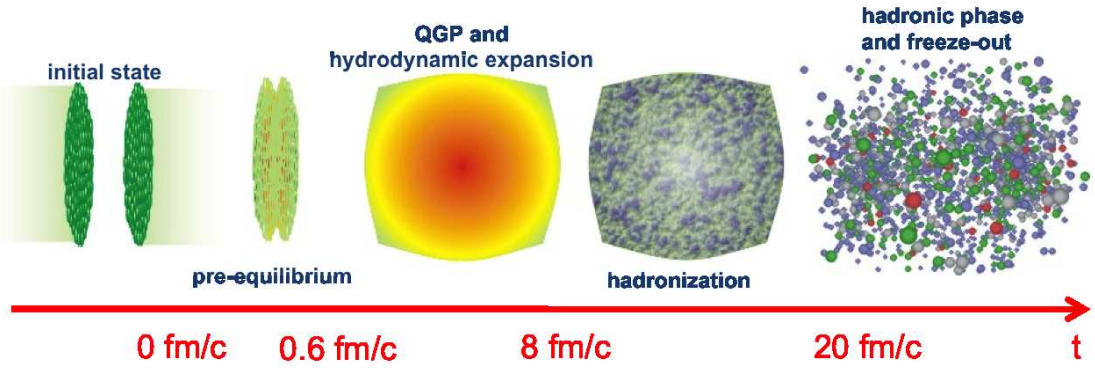

FIGURE 1.4: Cartoon of different stages of nuclear matter in heavy-ion collisions. The credit of this figure belongs to Steffen Bass.

In this dissertation, we will concentrate on the relatively low μ region of the phase diagram that is explored by LHC experiments and high energy RHIC experiments.

1.1.2 Exploring Hot and Dense Matter with Heavy-ion Collisions

To investigate the QGP state of the QCD phase diagram in the lab, the only currently known way is to collide beams of ultrarelativistic heavy-ions to create this extremely hot (a temperature in excess of 10^{12} K) and dense (an energy density above 1 GeV/fm^3) nuclear matter. The two experimental facilities in operation at which we can probe the QGP are the Relativistic Heavy-Ion Collider (RHIC) at the Brookhaven National Laboratory (BNL) and the Large Hadron Collider (LHC) at the European Organization for Nuclear Research (CERN). At RHIC, Gold (Au), Copper (Cu) or Uranium (U) nuclei can be accelerated to a center of mass energy of $\sqrt{s_{\rm NN}} = 200$ GeV per nucleon pair to produce the QGP matter, and at LHC Lead (Pb) nuclei are accelerated to even higher energy – currently $\sqrt{s_{\rm NN}} = 2.76$ TeV. It is now generally accepted that a strongly interacting QGP matter is created in these energetic nuclear collisions.

In heavy-ion collisions, the hot and compressed nuclear matter evolves through several stages as demonstrated in Fig.1.4 with a time scale estimated for Au-Au

collisions with $\sqrt{s_{\rm NN}} = 200$ GeV at RHIC.

To start with, two Lorentz contracted nuclei approach each other with almost the speed of light. During the collision, the overlapping region between the colliding nuclei is highly compressed and new particles, some of which carry large transverse momenta, are produced. It takes a short but finite time (the pre-equilibrium stage) for these particles to interact with each other and drive the system to local thermal equilibrium to form a QGP matter. The microscopic details of the dynamical evolution of the pre-equilibrium stage and its thermalization process still remain largely unknown but various models have been constructed to provide the initial condition of the subsequent QGP evolution. In this dissertation, the two most widely adopted models – the Glauber model [13, 14, 15] and the Kharzeev-Levin-Nardi (KLN) parametrization of the Color Glass Condensate (CGC) model [16, 17] – will be used and compared. In the Glauber model, the collision between two nuclei is viewed in terms of the individual interactions between mutually independent constituent nucleons; while in the KLN-CGC model, the unintegrated gluon distributions inside the two colliding nuclei are used to determine the production and distribution of the initial gluons.

For the current energy scale reached at RHIC and LHC, the QGP matter is expected to be a strongly coupled system. One may estimate the initial density of the created QGP matter as follows. The radius R of ^{197}Au nucleus is about 6.4 fm, which yields an area $S = \pi R^2$ around 128 fm^2 in the transverse plane for a head-on collision. Since it takes approximately 0.6 fm/c for the system to approach local equilibrium after the collision, the length L of the system in the longitudinal direction (along the beam axis) is around 1.2 fm when the QGP evolution commences. This leads to a volume $V = SL$ around 150 fm^3 that contains a total number (N) of 394 nucleons from the two colliding nuclei. Let us estimate that each nucleon contributes 30 to 40 partons. Then we obtain a number density around $n = 35N/V =$

90 fm^{-3}. The average distance between two partons can then be evaluated as $d = 1/\sqrt[3]{n} = 0.22$ fm, which corresponds to a momentum scale around $Q = \hbar c/d = 0.88$ GeV. According to Fig.1.1, α_s is greater than 0.5 for such a dense system. This strongly interacting QGP matter displays properties similar to that of an ideal fluid and therefore its bulk evolution has been successfully described by relativistic hydrodynamics [18, 19, 20, 21, 22, 23, 24, 25] with a value of the shear-viscosity-over-entropy-density ratio (η/s) [26] close to the lower boundary for universal quantum systems ($1/4\pi$) proposed in Ref. [27] based on the strong coupling limit. For central Au-Au collisions, the duration of the hydrodynamical expansion of the QGP is around 10-15 fm/c.

When the local temperature of a fluid cell drops below T_c during the hydrodynamical expansion, it hadronizes. Generally, one applies the Cooper-Frye formula [28] to calculate the spectra produced by the hadronizing QGP for hadrons with transverse momenta below 2 GeV. In the intermediate p_T regime (2-5 GeV), the recombination mechanism [29, 30, 31, 32] has been shown necessary for hadron production. Above 5 GeV, on the other hand, hadrons are being produced mostly via fragmentation [33, 34, 35] of high energy jets created in initial hard scatterings other than from the QGP matter itself.

After the hadronization, the hadrons continue to scatter off each other until the hadron gas is so dilute that all interactions cease. This is known as the hadronic phase and its dynamics can be studied with transport models of hadrons such as the UrQMD [36]. Finally, the hadrons are captured by detectors and their various spectra provide us hints of the properties of the hot and dense nuclear matter present in the earlier stages. In the following sections, we will briefly review how the spectra of both soft hadrons and hard probe particles are utilized to investigate the QGP matter.

1.2 QGP Bulk Evolution and Hydrodynamics

1.2.1 Hydrodynamic Equations

As mentioned earlier, as a strongly coupled system, the QGP displays properties similar to a perfect fluid and hence has been successfully described by hydrodynamics. In this subsection, we follow Ref. [37] to provide an overview on hydrodynamic equations that provide a model of the QGP background for our study of heavy flavor transport in this dissertation.

Hydrodynamics is an effective theory that describes the evolution of a fluid system. Instead of tracking the motions of all microscopic particles in the system, it divides the system into small fluid cells and treats each of them as a thermal subsystem close to local equilibrium. The size of each cell should be chosen such that the cell can be viewed as a good macroscopic representation of particles within it and meanwhile also a microscopic constituent of the whole system. In other words, the size of each cell should be simultaneously much larger than the mean free path $\lambda_{\rm mfp}$ of the particles that make up the fluid and much smaller than the length scale L of the fluid system. Therefore, the validity of hydrodynamics can be determined by a Knudsen number defined as $K \equiv \lambda_{\rm mfp}/L$. Hydrodynamics is valid for small K but breaks down for large K. In contrast, the validity of a microscopic transport model based on the Boltzmann equation requires a sufficiently large $\lambda_{\rm mfp}$. Nevertheless, there exists an overlap between the validity regions of hydrodynamics and microscopic transport – large $\lambda_{\rm mfp}$ and even larger L – in which we are allowed to derive the hydrodynamic equations from the microscopic transport model and then apply them to a wider regime as long as K remains small.

With the relaxation time approximation for the collision kernel, the Boltzmann

equation can be written as:

$$p^\mu \partial_\mu f(x,p) = C(x,p) = \frac{p\cdot u(x)}{\tau_{\rm rel}}\left[f_{\rm eq}\left(\frac{p\cdot u(x)}{T(x)}\right) - f(x,p)\right], \tag{1.6}$$

in which $u^\mu \equiv (\gamma, \gamma\vec{v})$ is the four velocity, $f(x,p)$ represents the phase space distribution of a particular type of constituent particle of the fluid system, and $f_{\rm eq}$ denotes the distribution of local thermal equilibrium

$$f_{\rm eq}\left(\frac{p\cdot u(x)}{T(x)}\right) = \frac{g_{\rm DOF}}{e^{p\cdot u(x)/T(x)} \pm 1} \tag{1.7}$$

with $T(x)$ as the local temperature and $\pm$ sign for Fermi-Dirac/Bose-Einstein statistics. Here the chemical potential $\mu(x)$ has been ignored which will not affect our discussions below. Meanwhile, one may define the local current density $j^\mu(x)$ and the energy-momentum tensor $T^{\mu\nu}(x)$ as

$$j^\mu(x) = \int d\mathcal{P} p^\mu f(x,p), \tag{1.8}$$

$$T^{\mu\nu}(x) = \int d\mathcal{P} p^\mu p^\nu f(x,p), \tag{1.9}$$

in which we have denoted

$$d\mathcal{P} \equiv \frac{d^3p}{(2\pi)^3 E} \tag{1.10}$$

for short.

For the simplest case, we start with an ideal fluid in which the interaction strength is infinite and therefore $f(x,p)$ keeps the same as $f_{\rm eq}$. Consequently, the right hand side of Eq.(1.6) gives 0. Furthermore, by using Eqs.(1.6), (1.8) and (1.9), we obtain the conservation equations for the current density and the energy-momentum tensor:

$$\partial_\mu j^\mu(x) = 0, \qquad \partial_\mu T^{\mu\nu}(x) = 0. \tag{1.11}$$

Meanwhile, since the only vector we have for constructing j^μ is p^μ (or u^μ), we may decompose it as

$$j^\mu(x) = n(x)u^\mu(x), \tag{1.12}$$

in which $n(x)$ is the scalar part. Similarly, we may decompose $T^{\mu\nu}$ with $u^\mu u^\nu$ and $g^{\mu\nu}$ as

$$T^{\mu\nu}(x) = e(x)u^\mu u^\nu - P(x)\triangle^{\mu\nu}, \tag{1.13}$$

where we have defined $\triangle^{\mu\nu} \equiv g^{\mu\nu} - u^\mu u^\nu$. The physical meaning of such a decomposition becomes apparent in the local rest frame of the fluid cell where $u^\mu = (1, \vec{0})$. In this case, $u^\mu u^\nu$ acts as a temporal projector – the (00) part of $g^{\mu\nu}$ – and $\triangle^{\mu\nu}$ acts as the spatial projector. With these projectors, one may further extract the scalar parts of Eqs.(1.12) and (1.13) as follows:

$$n(x) = u_\mu j^\mu, \quad e(x) = u_\mu T^{\mu\nu} u_\nu, \quad \text{and} \quad P(x) = -\frac{1}{3}\triangle_{\mu\nu} T^{\mu\nu}, \tag{1.14}$$

in which we have applied $u_\mu u^\mu = 1$, $u_\mu \triangle^{\mu\nu} = 0$ and $\triangle_{\mu\nu}\triangle^{\mu\nu} = 3$. One may substitute Eqs.(1.8) and (1.9) into Eq.(1.14) to calculate these scalars explicitly. And since these scalars are Lorentz invariant, we may evaluate them in the local rest frame so that their physical meanings are easy to observe:

$$n(x) = \frac{1}{(2\pi)^3}\int d^3\bar{p}\, f_{\rm eq}(\bar{E}/T) \quad = \quad \text{particle density in the l.r.f,} \tag{1.15}$$

$$e(x) = \frac{1}{(2\pi)^3}\int d^3\bar{p}\, \bar{E} f_{\rm eq}(\bar{E}/T) \quad = \quad \text{energy density in the l.r.f,} \tag{1.16}$$

$$P(x) = \frac{1}{(2\pi)^3}\int d^3\bar{p}\, \frac{\bar{\vec{p}}^2}{3\bar{E}} f_{\rm eq}(\bar{E}/T) \quad = \quad \text{pressure in the l.r.f.} \tag{1.17}$$

Here, the symbol "bar" denotes the variable to be in the local rest frame and we have applied $\bar{p}\cdot\bar{u} = \bar{E}$.

Before writing out the final "equations of motion" for ideal hydrodynamics, we define three more notations. (1) Expansion rate $\theta \equiv \partial_\mu u^\mu$ of the fluid cell; (2) full

derivative with respect to the proper time τ:

$$D \equiv u_\mu \partial^\mu = \gamma \frac{\partial}{\partial t} + \gamma \frac{\partial \vec{r}}{\partial t} \frac{\partial}{\partial \vec{r}} = \gamma \frac{d}{dt} = \frac{d}{d\tau}, \tag{1.18}$$

and we denote $Df \equiv \dot{f}$; and (3) the spatial gradient in the local rest frame $\bigtriangledown_\mu \equiv \bigtriangleup_{\mu\nu} \partial^\nu$ as will appear in

$$\partial_\mu = g_{\mu\nu} \partial^\nu = u_\mu u_\nu \partial^\nu + \bigtriangleup_{\mu\nu} \partial^\nu \equiv u_\mu D + \bigtriangledown_\mu. \tag{1.19}$$

With the above setups, we may obtain the equations of motion as follows.

$$0 = \partial_\mu j^\mu = u^\mu \partial_\mu n + n \partial_\mu u^\mu = \dot{n} + n\theta; \tag{1.20}$$

$$\begin{aligned} 0 &= \partial_\mu T^{\mu\nu} = \partial_\mu \left[(e+P) u^\mu u^\nu - P g^{\mu\nu} \right] \\ &= u^\mu u^\nu \partial_\mu (e+P) + (e+P) u^\nu \partial_\mu u^\mu + (e+P) u^\mu \partial_\mu u^\nu - g^{\mu\nu} \partial_\mu P \\ &= u^\nu D(e+P) + (e+P) u^\nu \theta + (e+P) \dot{u}^\nu - (u^\nu D + \bigtriangledown^\nu) P \\ &= u^\nu \dot{e} + (e+P) u^\nu \theta + (e+P) \dot{u}^\nu - \bigtriangledown^\nu P. \end{aligned} \tag{1.21}$$

From Eq.(1.20), we have

$$\dot{n} = -n\theta, \tag{1.22}$$

indicating the dilution of the fluid system while it expands. And by multiplying Eq.(1.21) with u_ν, we would obtain

$$\dot{e} = -(e+P)\theta, \tag{1.23}$$

which describes the change of the energy density due to the expansion of the system. Here we have applied $u_\nu D u^\nu = D(u_\nu u^\nu)/2 = 0$ and $u_\nu \bigtriangledown^\nu = 0$. Note that the relative change of e is faster than that of n as given by Eq.(1.22) because of the work done by the pressure. In the end we may substitute Eq.(1.23) back into Eq.(1.21) and obtain

$$\dot{u}^\nu = \frac{\bigtriangledown^\nu P}{e+P}. \tag{1.24}$$

This is nothing but the Newton's second law for the fluid cell where $\dot{u}^\nu$ is its acceleration, $\bigtriangledown^\nu P$ is the pressure gradient that acts as the driving force for the hydrodynamical expansion and $e + P$ is the inertial of the fluid.

Equations (1.22), (1.23) and (1.24) are the equations of motion (EOM) of ideal hydrodynamics. All together they provide 5 independent equations. Meanwhile, we have 6 unknowns: n, e, P and 3 independent components of u^μ. To close the algebraic system, we need an additional equation – the equation of state (EOS) that relates thermodynamic quantities e and P. This EOS can be either calculated using a thermodynamic model or be more rigorously obtained from lattice QCD as discussed in Sec.1.1. As an illustrative example, we take $P = c_s^2 e$, where c_s is the speed of sound inside the fluid system as defined in $c_s^2 \equiv \partial P/\partial e$. Then Eq.(1.24) can be reduced to

$$\dot{u}^\nu = \frac{c_s^2}{1 + c_s^2} \frac{\bigtriangledown^\nu e}{e}. \tag{1.25}$$

The physical interpretation of c_s becomes apparent with Eq.(1.25). It characterizes the "stiffness" of the EOS of the fluid system. With a fixed gradient of energy density, a larger c_s – a stiffer system – yields a faster acceleration of the hydrodynamical expansion and a softer c_s leads to a slower acceleration. Note that around T_c, c_s is expected to approach a minimum in both the thermodynamic model and in the lattice QCD calculation because in the mixed phase, density perturbations cause the conversion from the QGP matter to the hadron gas instead of propagating themselves.

We may repeat the above derivations for the equations of motion of a viscous fluid. In a viscous fluid, the coupling strength is finite and therefore the distribution function of constituent particles $f(x, p)$ is not able to instantaneously return to the

equilibrium limit while the system is expanding. Thus we should decompose it as

$$f(x,p) = f_{\rm eq}\left(\frac{p\cdot u(x)-\mu(x)}{T(x)}\right) + \delta f(x,p). \tag{1.26}$$

The decomposition is non-trivial. To make it unique, one needs to find optimal parameters for the local equilibrium quantities $T(x)$, $\mu(x)$,$u^\mu(x)$ so that $f_{\rm eq}$ reproduces certain key macroscopic observables associated with the non-equilibrated distribution function f. This can be achieved by the "Landau matching procedure". By requiring

$$\delta n = u_\mu \delta j^\mu = 0, \tag{1.27}$$

we may fix μ/T, and by requiring

$$\delta e = u_\mu \delta T^{\mu\nu} u_\nu = 0, \tag{1.28}$$

we may further fix T. In the end we may use the "Landau frame" to determine the local rest frame of the fluid cell:

$$T^{\mu\nu}u_\nu = e u^\mu, \tag{1.29}$$

which is equivalent to $u_\nu \delta T^{\mu\nu} = 0$ with $\delta e = 0$, indicating that there is no momentum flow in the local rest frame. Note that u^μ is the time-like eigenvector of $T^{\mu\nu}$.

With $\delta f \neq 0$, j^μ and $T^{\mu\nu}$ can now be decomposed as

$$\begin{aligned} j^\mu(x) &= n(x)u^\mu(x) + V^\mu(x) \\ T^{\mu\nu}(x) &= e(x)u^\mu u^\nu - [P(x)+\Pi(x)]\triangle^{\mu\nu} + \pi^{\mu\nu}, \end{aligned} \tag{1.30}$$

with $n(x)$, $e(x)$ and $P(x)$ the same as those calculated with $f_{\rm eq}$ for ideal hydrodynamics due to the above Landau matching conditions, and $V^\mu = \triangle^{\mu\nu} j_\nu$ being the net charge flow in the local rest frame, $\Pi = -1/3 \triangle_{\mu\nu} T^{\mu\nu} - P$ being the bulk viscous pressure, and $\pi^{\mu\nu} = \triangle^{\mu\nu}_{\alpha\beta} T^{\alpha\beta}$ being the shear stress tensor. Here we define

$$\triangle^{\mu\nu}_{\alpha\beta} \equiv \frac{1}{2}\left(\triangle^\mu_\alpha \triangle^\nu_\beta + \triangle^\mu_\beta \triangle^\nu_\alpha\right) - \frac{1}{3}\triangle^{\mu\nu}\triangle_{\alpha\beta}, \tag{1.31}$$

so that $\pi^{\mu\nu}$ is a traceless tensor without time component in the local rest frame ($\pi^{\mu}_{\mu} = 0$ and $u_\mu \pi^{\mu\nu} u_\nu = 0$). In the case of zero chemical potential $\mu = 0$, there exists no net charge (baryon free and strangeness free system), and we have $V^\mu = 0$. And although $\delta f \neq 0$ leads to non-zero collision kernel C in Eq.(1.6), its integrals $\int d\mathcal{P} C$ and $\int d\mathcal{P} p^\mu C$ are still zero so that the conservation of particle number and energy-momentum Eq.(1.11) still holds. However, at this moment, we have the same number of independent equations as for ideal hydrodynamics, but 6 more unknowns – Π and 5 independent components of $\pi^{\mu\nu}$. There are various approaches in the literature for finding the missing equations. One may refer to Ref. [37, 11] for a summary about this and a detailed derivation of the closed set of EOM for viscous hydrodynamics. Here we only cite two more useful definitions:

$$\Pi \equiv -\zeta\theta, \qquad \pi^{\mu\nu} \equiv 2\eta\sigma^{\mu\nu} \quad (\ \sigma^{\mu\nu} \equiv \triangle^{\mu\nu}_{\alpha\beta} \bigtriangledown^{\alpha} u^{\beta}\ ), \tag{1.32}$$

in which ζ is known as the bulk viscosity and η shear viscosity.

In the literature, there exist various numerical realizations of hydrodynamic equations. For instance, since the QGP medium expands with almost speed of light in the longitudinal direction ($\hat{z}$ – direction in which the colliding beams travel), it is difficult to accurately describe both the small system at early time and the much larger system at later times with (t, x, y, z) coordinates if the grid size is fixed. However, this problem can be solved with (τ, x, y, η_s) coordinates where $\tau \equiv \sqrt{t^2 - z^2}$ is the proper time and $\eta_s = \frac{1}{2}\ln[(t+z)/(t-z)]$ is the space-time rapidity. This coordinate frame has been adopted by many hydrodynamic codes. In order to simplify the calculation, one may assume longitudinal boost invariance for the solutions, i.e., the fluid profile only depends on (τ, x, y) but not η_s – for example $T(\tau, x, y, \eta_{s1}) = T(\tau, x, y, \eta_{s2})$. This is known as a (2+1)-dimensional hydrodynamic model. Other calculations assume that the distributions of particle number, energy density, etc., are homogeneous in the transverse plane and only concentrates on the expansion in the longitudinal

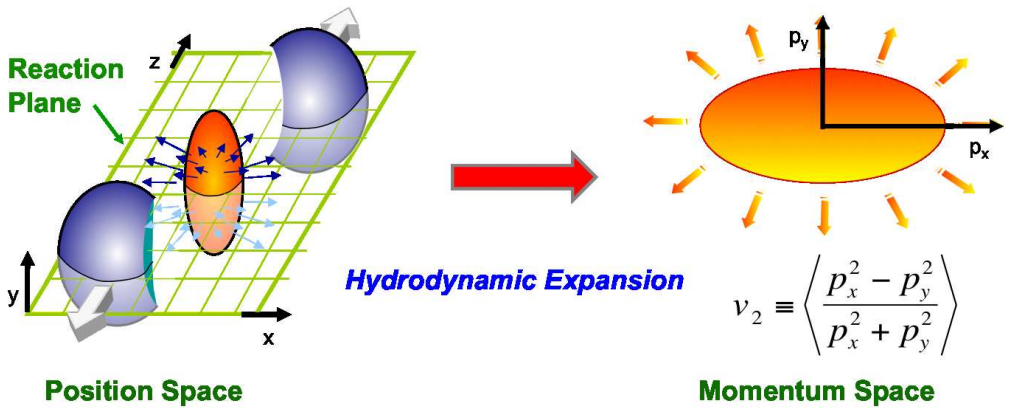

FIGURE 1.5: Development of the momentum space elliptic flow from the position space anisotropy.

direction. This is known as a (1+1)-dimensional model. Of course, there is also (0+1)-dimensional model where both the transverse homogeneity and longitudinal boost invariance are assumed. In fact, an analytical solution (the Bjorken solution) exists for this special case and one may also refer to Ref. [37] for related details.

1.2.2 Anisotropic Flows of Soft Hadrons

Hydrodynamics has successfully described and predicted the anisotropic flows of low momentum – so called "soft" – hadrons produced in relativistic heavy-ion collisions, which is considered an important evidence of the existence of strongly coupled QGP matter.[1]

As demonstrated in Fig.1.5, the rapid collision between the two nuclei forms an almond shaped zone of highly compressed QCD matter in their overlap. Here we define the concept of "reaction plane" as the plane spanned by the beam axis (z) and the impact parameter (x). Because of the geometric anisotropy of the compressed QCD matter, its pressure gradient in the x axis is greater than that in the y axis, and therefore it accelerates and expands faster in x than in y [see Eq.(1.24)]. In the

[1] The discussions about how to convert the hydrodynamic medium into observed hadrons will be postponed to Sec.6.1.1.

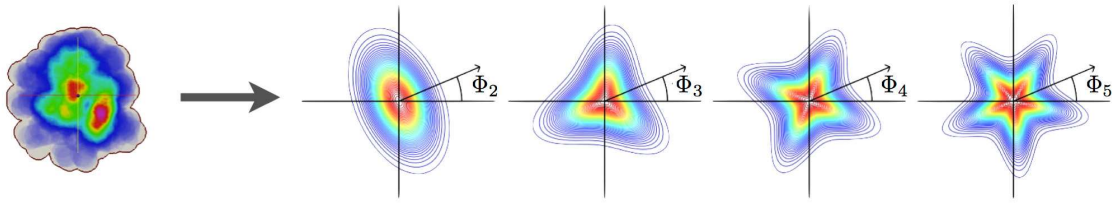

FIGURE 1.6: Decomposition of a fluctuating initial condition of hydrodynamical evolution into its first 4 harmonic deformations. This figure is taken from Ref. [38].

end, the geometric asymmetry is transformed into an anisotropy in momentum space, which can be measured via the momentum distribution of observed hadrons. We may define the elliptic flow coefficient as the average of the ratio between the difference and sum of hadron momentum squares in x and y directions: $v_2 \equiv \left\langle (p_x^2 - p_y^2)/(p_x^2 + p_y^2) \right\rangle$.

In Fig.1.5, we assume that the two colliding nuclei are smoothly distributed round disks. However, in reality, both the nucleon positions and color charges inside nuclei fluctuate from event to event [39]. This leads to many interesting consequences, such as (1) the existence of finite elliptic flow even in the ultra-central collisions (at almost zero impact parameter); (2) the minor axis of the elliptic initial profile of the created nuclear matter no longer residing in the reaction plane as defined above; and (3) the existence of odd-order harmonics in the collision geometry and flow [40, 41, 42, 43, 44, 45, 46, 47, 48, 49, 50, 51, 52]. In Fig.1.6, we illustrate the decomposition of a fluctuating initial profile of QGP into its first 4 harmonic components. One observes that with fluctuating nuclear structures, the colliding region between the two nuclei is no longer an ellipse symmetric about the y axis. Instead, it contains triangular, quadrangular, pentagonal, etc., geometric components as well. And each harmonic component has its own optimal coordinate as denoted by Φ_n in Fig.1.6. In the literature, one defines these planes – rotated from the reaction plane by Φ_n about the z axis – as the "participant planes" of the respective harmonic components. Similar as the development of the elliptic flow v_2, these higher order deformations

of the geometric profile will also be transformed into their corresponding collective flows in the momentum space through hydrodynamical evolution. The v_2 coefficient can be generalized to the following n^{th} order harmonic coefficient according to the Fourier decomposition of the hadron spectra:

$$\frac{dN^i}{dyp_{\mathrm{T}}dp_{\mathrm{T}}d\phi_p} = \frac{1}{2\pi}\frac{dN^i}{dyp_{\mathrm{T}}dp_{\mathrm{T}}}\left[1 + 2\sum_{n=1}^{\infty} v_n^i(y, p_{\mathrm{T}})\cos\left(n\left[\phi_p - \Psi_n^{(i)}(y, p_{\mathrm{T}})\right]\right)\right], \quad (1.33)$$

in which i represents the selected species of observed hadrons, p_{T} and ϕ_p denote the magnitude and angle of momentum in the transverse plane, and y is the rapidity defined as $y \equiv \frac{1}{2}\ln\left[(E + p_z)/(E - p_z)\right]$. Here, $v_n^i(y, p_{\mathrm{T}})$ is the differential coefficient of the n^{th} order flow with respect to y and p_{T}, and one may integrate Eq.(1.33) over a particular momentum regime to obtain the corresponding integrated flow coefficients. Note that just as Φ_n for the geometric anisotropy above, different orders of momentum space asymmetry also have their own optimal axes denoted by Ψ_n. A proper choice of Ψ_n maximizes the v_n for a given collisional event and this Ψ_n helps define the n^{th} order "event plane" in the same way as the previous "participant plane". Due to the non-linear behavior of hydrodynamics, the participant plane of the initial geometric space and the event plane of the final momentum space do not necessarily coincide with each other, although they will be the same after we average over a sufficiently large number of collision events. With the above definitions, it is easy to prove that one convenient scheme to simultaneously obtain v_n and Ψ_n is as follows: we start with any transverse coordinate – using the reaction plane for example – and calculate ϕ_p with respect to it, then extract the real and imaginary parts of the average $\exp(in\phi_p)$ of the selected hadrons as

$$A^i(y, p_{\mathrm{T}}) + iB^i(y, p_{\mathrm{T}}) \equiv \frac{\int d\phi_p e^{in\phi_p}\frac{dN^i}{dyp_{\mathrm{T}}dp_{\mathrm{T}}d\phi_p}}{\int d\phi_p \frac{dN^i}{dyp_{\mathrm{T}}dp_{\mathrm{T}}d\phi_p}}, \quad (1.34)$$

and in the end the flow coefficient v_n and the event plane angle Ψ_n with respect

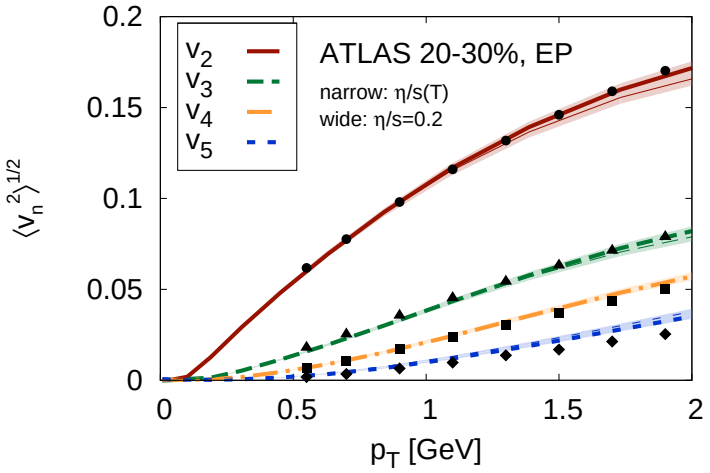

FIGURE 1.7: Comparison of hadron v_n between hydrodynamic calculation and experimental data. This figure is taken from Ref. [53].

to the chosen coordinate are directly given by the module and the direction of this complex number:

$$v_n = \sqrt{A^2 + B^2}, \qquad \tan(n\Psi_n) = B/A. \tag{1.35}$$

In Fig.1.7, we show one example of a comparison of hadron v_n between a hydrodynamic calculation [53] and experimental data [52]. In Ref. [53], a classical Yang-Mills description is applied for the early time evolution of the gluon field before the start of a (3+1)-dimensional hydrodynamic expansion of the QGP fireball. In Fig.1.7, both a constant and a temperature dependent η/s parametrization [54] are utilized for the hydrodynamic model, and they both provide a good description of the observed hadron collective flows up to the 5^{th} order harmonic component.

Because of the success of hydrodynamics in describing the dynamical evolution of the strongly interacting system, it has been widely applied to investigate the initial state fluctuations in heavy-ion collisions which still remain largely unknown. We will come back to this topic in Sec.4.3.

1.3 Exploring QGP Properties with Jet Quenching

In the previous section, we have made the case that the study of soft hadrons produced in heavy-ion collisions reveals valuable information on the QGP such as its η/s coefficient and the quantum fluctuations in its initial state. However, since these low energy hadrons cannot exist inside a deconfined medium and are only produced on the freeze-out hypersurface of the QGP, it is hard to probe the microscopic QCD structure inside the QGP with them alone. Apart from looking at the thermal radiation emitted from a hot and dense QCD medium, an alternative approach to test its properties is to shoot probe particles through it and study their interactions within the medium. In the following sections, we will briefly review the dynamics of high momentum "hard probe" particles inside the QGP. Note that other probes such as direct photons and di-leptons can also be used but are beyond the discussions of this dissertation. One may find a broader overview of different probe particles in Ref. [11].

"Hard probes" [55] refer to high energy particles created directly from partonic scatterings with large momentum transfer Q^2. Thus their cross sections can be theoretically predicted with pQCD calculations. Their formation times $\tau_f \approx 1/p_{\mathrm{T}} < 0.1$ fm are shorter than the duration of the pre-equilibrium stage before the QGP formation, which allows them to propagate through and observe the whole evolution history of the QGP matter.

One good example of a hard probe is a "jet". As illustrated in Fig.1.8, hard scattering between two partons can create two or more partons with large virtualities. These outgoing partons may reduce their virtualities by either radiating gluons or splitting into quark-antiquark pairs until the remaining virtualities are down to much smaller values than 1 GeV. Such a parton branching evolution is base on the QCD radiation probabilities and can be described by the Dokshitzer-Gribov-Lipatov-

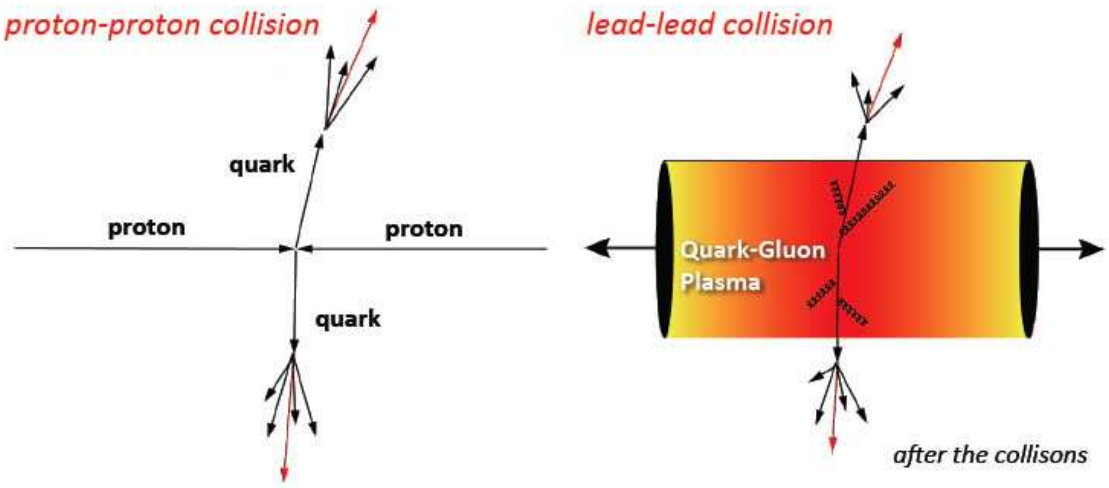

FIGURE 1.8: Cartoon of jet productions in proton-proton and nucleus-nucleus collisions. This figure is taken from the website of Prof. Andre Mischke at Utrecht University.

Altarelli-Parisi (DGLAP) equations [56, 57, 58, 59]. In the end, the produced partons fragment non-perturbatively into a bunch of almost collinear final-state hadrons which are called a "jet". What particles are included in the jet depends on how the jet is defined, e.g. via the selected size of the jet cone around the leading (most energetic) hadron.

The calculation of the jet spectra is based on the following factorization:

$$d\sigma^{\rm hard}_{AB\to h} = f_{a/A}(x_1, Q^2) \otimes f_{b/B}(x_2, Q^2) \otimes d\sigma^{\rm hard}_{ab\to c}(x_1, x_2, Q^2) \otimes D_{c\to h}(z, Q^2), \quad (1.36)$$

in which $f_{a/A}(x_1, Q^2)$ is the parton distribution function of nucleon/nucleus A – the probability of finding parton a with fractional momentum x_1 in A ($x_1 \equiv p_a/p_A$) – and $f_{b/B}(x_2, Q^2)$ of nucleon/nucleus B; $d\sigma^{\rm hard}_{ab\to c}(x_1, x_2, Q^2)$ is the inclusive differential cross section for producing parton c via the hard process $ab \to c$ at the partonic level; and $D_{c\to h}(z, Q^2)$ is the fragmentation function that describes the probability for parton c to fragment into the observed hadron h with fractional momentum z. Among these three parts, $d\sigma^{\rm hard}_{ab\to c}$ can be calculated with pQCD method while the other two –

parton distribution function and fragmentation function – are non-perturbative and should be determined by experimental observations.

As shown in Fig.1.8, jets can be produced in both proton-proton and nucleus-nucleus collisions. However, in the latter process, a hot and dense QCD medium can be created in which a parton may lose significant amount of energy before fragmenting into the observed hadrons. Consequently, the spectra of produced jets will shift towards lower p_{T} regime in nucleus-nucleus collision with respect to proton-proton collision and hence appear suppressed at large p_{T}. This is known as the medium modification to jets or jet quenching and is one of the first proposed "smoking guns" for the existence of the QGP [60]. To quantify the medium effect on jet production, we may define the nuclear modification factor as

$$R_{\mathrm{AA}}(p_{\mathrm{T}}, y; b) \equiv \frac{d^2N^i_{\mathrm{AA}}/dydp_{\mathrm{T}}}{N_{\mathrm{coll}}(b) \times d^2N^i_{\mathrm{pp}}/dydp_{\mathrm{T}}}, \tag{1.37}$$

in which the numerator represents the observed hadron spectra for species i in nucleus-nucleus collision, and the denominator the corresponding spectra produced in proton-proton collision scaled with the number of binary collisions. This number N_{coll} denotes how many hard collisions between nucleon pairs happen in each nucleus-nucleus collision and depends on its impact parameter b. If there is no medium modification, i.e., the nucleus-nucleus collision is merely a superposition of N_{coll} proton-proton collisions, R_{AA} should be exactly 1. In contrast, parton energy loss in a dense medium would lead to $R_{\mathrm{AA}} < 1$ at high p_{T}.

In Fig.1.9, we show the nuclear modification factors of different particle species observed at $\sqrt{s_{\mathrm{NN}}} = 2.76$ TeV Pb-Pb collisions together with several theoretical predictions based on pQCD models of parton energy loss [62, 63, 64, 65, 66]. We note that color-neutral particles such as the photon and the Z^0 boson hardly interact with the color deconfined hot and dense medium and therefore their R_{AA}'s are consistent

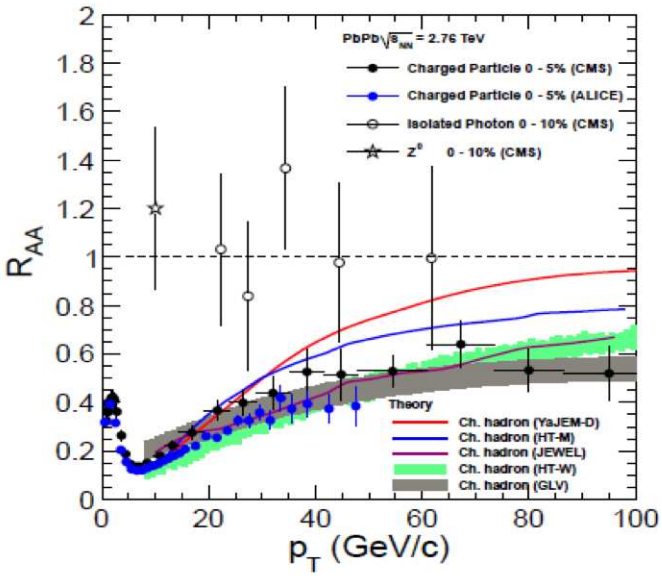

FIGURE 1.9: Nuclear modification factor R_{AA} as a function of p_{T} for various particle species, compared between theoretical predictions and experimental data. This figure is taken from Ref. [61].

with 1. On the other hand, charged hadrons that are fragmented from partons are significantly suppressed in Pb-Pb collisions in the high p_{T} regime.

Parton energy loss inside the QGP is thought to originate from a combination of collisional [67, 68] and radiative [69, 70] processes that jets experience when they travel through the medium. The former mechanism comes from the quasi-elastic scatterings between the probe parton and the medium constituents, and the latter comes from gluon radiation induced by the inelastic scatterings of the probe parton within the medium. The competition between these two energy loss mechanisms will be one of the major topics studied in the dissertation later. Various phenomenological approaches have been established to relate the QCD energy loss calculation of parton with the hadron spectra observed in experiments. In the literature, there are four major formalisms of parton energy loss inside the QGP [11]: the path-integral approach to the opacity expansion (BDMPS-LCPI/ASW) [71, 72, 73, 74, 75, 76, 77, 78, 79],

the reaction operator approach to the opacity expansion (DGLV) [80, 81, 82, 83], the higher twist (HT) approach [84, 85, 86, 87, 88, 89], and the finite temperature field theory approach (AMY) [90, 91, 92, 93]. All these formalisms are based on QCD factorization (Eq.1.36) and introduce the effect of in-medium parton energy loss by modifying the parton fragmentation function: $D_{c\to h}^{\mathrm{vac}}(z) \to D_{c\to h}^{\mathrm{med}}(z', \hat{q})$ where $\hat{q}$ is called the gluon transport coefficient characterizing the interaction strength between the parton and the QGP and $z' < z$ encodes the information on the parton energy loss. The final hadronization process from hard partons to observed hadrons is always assumed to take place in the vacuum after the partons traverse the QGP medium. The differences between these approaches lie in their respective assumptions regarding the properties of the probe particles and the medium, such as the relation between different scales: parton energy E and virtuality Q^2, the Debye mass m_D of the medium characterizing the minimum momentum exchange between the hard parton and the medium, and the length scale of the medium L. Systematic comparisons between these different energy loss formalisms can be found in Ref. [11, 94, 95].

Apart from the single inclusive hadron suppression (R_{AA}), sophisticated calculations have also been implemented for di-hadron [96, 97, 87] and photon-hadron correlations [98, 99, 100]. One of the goals of these studies is the qualitative extraction of jet transport coefficients in the strongly interacting QGP medium by comparing the calculations with the measured jet modification data. The most commonly used transport coefficient for jet energy loss is the above mentioned gluon transport coefficient $\hat{q}$ defined as

$$\hat{q} \equiv \rho \int d^2k_\perp k_\perp^2 \frac{d\sigma}{d^2k_\perp}, \tag{1.38}$$

in which ρ is the density of scattering centers (mainly gluons) in the medium, $k_\perp$ is the transverse momentum of the radiated gluon and $d\sigma$ is the differential cross

section for the parton-medium interaction. From Eq.(1.38), one may understand $\hat{q}$ as the average momentum broadening in the transverse plane of a hard parton while it propagates through the medium, and therefore reveals crucial information of the QGP fireball such as its local density and temperature.

1.4 Overview of Heavy Flavor Dynamics in Heavy-ion Collisions

1.4.1 Dynamics of Open Heavy Flavor in Heavy-ion Collisions

Apart from jet, another hard probe of the QGP matter is heavy quark. Heavy quarks (Q), including charm (c) and bottom (b) quarks, may exist either as bare quarks inside the QGP, or as bound states of $Q\bar{Q}$ when the medium temperature is still above $T_{\rm c}$ but not too high. We call the former state as "open" heavy quark and the latter as heavy quarkonium – charmonium for $c\bar{c}$ and bottomonium for $b\bar{b}$. Note that the mesonic bound states of heavy and light quark pairs ($Q\bar{q}$ or $\bar{Q}q$) that form below $T_{\rm c}$ such as D and B mesons are also named as open heavy mesons. In this dissertation, we mainly concentrate on the dynamics of open heavy flavor in heavy-ion collisions. Nevertheless, study of heavy quarkonium is also important and will be briefly discussed in the next subsection.

The most important property of heavy quarks is their large masses – $M_c \approx 1.5$ GeV for the charm quark and $M_b \approx 4.7$ GeV for the bottom quark which are much larger than $\Lambda_{\rm QCD} \approx 200$ MeV and the medium temperature $T \approx 300 \sim 400$ MeV. Because they are so heavy, their thermal production from the QGP medium is significantly suppressed and heavy quarks are instead primarily produced at the very early stage of heavy-ion collisions via hard scatterings and then propagate through and interact with the QGP matter with their flavor conserved. They thus provide a valuable tool to probe the space-time profile and transport properties of the QGP fireball. Since they are so heavy, the thermal correction to their masses can be considered small and therefore they serve as stable probe particles. Previous studies have shown

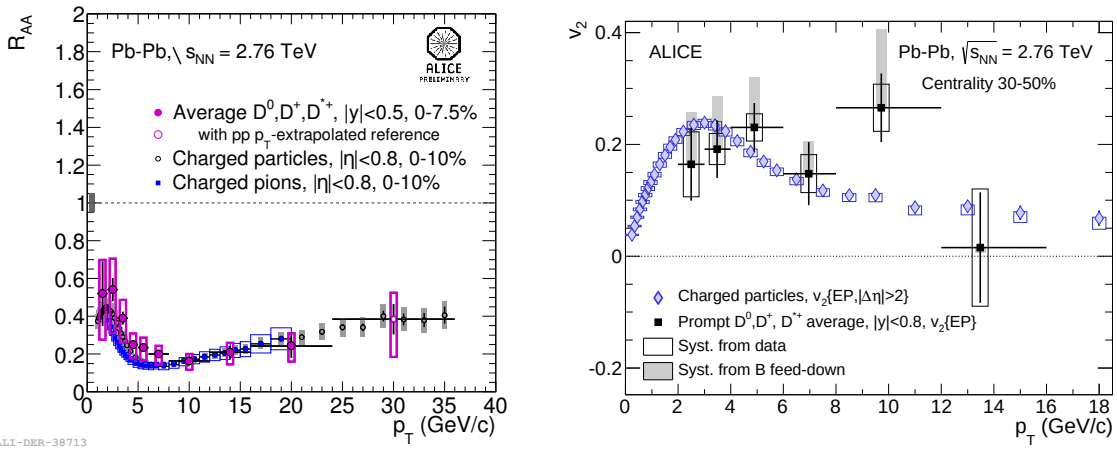

FIGURE 1.10: D meson $R_{\rm AA}$ and v_2 measured by the ALICE collaboration, compared with those of light hadrons. These two figures are taken from Ref. [108] and Ref. [109] .

that low-$p_{\rm T}$ heavy quarks provide a direct measure of the thermal properties of the medium, while at large $p_{\rm T}$ heavy quarks may provide a reference to investigate the medium modification of high-energy jets [101, 102]. At intermediate $p_{\rm T}$, heavy quarks and mesons may provide rich information for our understanding of fragmentation-versus-coalescence mechanisms for hadron formation [103, 104, 105, 106, 107].

Over the past decade, experimental observations at both RHIC and LHC have revealed a lot of interesting data on heavy flavor hadrons and their decay electrons [110, 111, 112, 113, 108, 114, 109], among which the most surprising results are the small value of their nuclear modification factor $R_{\rm AA}$ and the large value of their elliptic flow coefficient v_2, which are almost comparable to those of light hadrons as shown in Fig.1.10. This is contradictory to earlier expectations of the mass hierarchy of parton energy loss – $\Delta E_g > \Delta E_{u,d} > \Delta E_c > \Delta E_b$ – and is called the "heavy flavor puzzle". This puzzle requires a more detailed understanding of heavy flavor dynamics in heavy-ion collisions, including not only the in-medium energy loss of bare heavy quarks but also their evolution before and after the QGP phase.

Since energy loss grows with increases of medium temperature and density, heavy

quarks are expected to lose energy mostly in the QGP phase. And as discussed earlier, there exist two energy loss mechanisms for probe particles inside the QGP: medium-induced gluon radiation and quasi-elastic scattering with background medium partons [69, 67]. For light flavor partons, medium-induced gluon radiation has been shown to be more important than collisional energy loss, e.g., in the suppression of single or triggered hadron production at high transverse momenta [68, 115, 116, 117, 100]. For heavy quarks, on the other hand, collisional energy loss is usually considered to be the dominant mechanism especially at low energies [118, 119], due to the so called "dead cone effect" [120, 121]. The dead cone effect suggests that gluon bremsstrahlung off a heavy quark differs from that off a massless parton because of the kinematics constraints introduced by the mass. The distribution of soft gluons radiated by a heavy quark can be written as [120]

$$dP_{\rm HQ} = \frac{\alpha_s C_F}{\pi}\frac{d\omega}{\omega}\frac{k_\perp^2 dk_\perp^2}{(k_\perp^2+\omega^2\theta_0^2)^2} \approx dP_0 \cdot \left(1+\frac{\theta_0^2}{\theta^2}\right)^{-2}, \qquad \theta_0 \equiv \frac{M}{E} = \frac{1}{\gamma}, \tag{1.39}$$

in which $dP_{\rm HQ}$ and dP_0 denote the gluon distribution radiated from massive and massless quarks respectively, $C_F = 4/3$ is the color factor, ω is the gluon energy, $k_\perp$ is its transverse momentum, $\theta = k_\perp/\omega$ corresponds to the radiation angle, and M and E are the mass and energy of the heavy quark. Equation (1.39) implies that compared with gluon bremsstrahlung off a light parton, the radiation power of heavy quark is greatly suppressed in the forward cone θ_0 whose size increases with the mass-energy ratio. In other words, unless in an ultrarelativistic scenario, the phase space open for gluon radiation is restricted by the mass of the heavy quark. Note that the power of -2 in Eq.(1.39) is obtained under the idealized assumption of an infinitely energetic heavy quark and a static and uniform QGP medium [11]. This power may change with a more realistic treatment of the QGP matter – for instance, it becomes -4 in the higher-twist formalism [122] which will be adopted in

this dissertation. Because of the dead cone effect, the other energy loss mechanism – quasi-elastic scattering – is considered dominant especially for describing heavy flavor phenomenology observed at RHIC.

In the limit of multiple scatterings where the momentum transfer in each interaction is small, the motion of heavy quarks inside a thermalized medium can be treated as Brownian motion which is typically described by the Langevin equation [123, 118, 124, 125, 106, 126, 127, 128]. Such a framework has provided a reasonable description of the suppression and the elliptic flow of heavy flavor decay products such as the non-photonic electrons measured by RHIC experiments at relatively low p_{T}. However, when extending to higher p_{T} regions such as those reached by the LHC experiments, even heavy quarks become ultra-relativistic and thus they are expected to behave similar to light partons. In this relativistic limit, collisional energy loss alone may no longer be sufficient for simulating the in-medium evolution of heavy quarks, and radiative energy loss corrections may become significant [129, 107, 130]. The incorporation of radiative energy loss into the calculation of heavy quark evolution has been implemented in other transport frameworks such as linearized Boltzmann approach [131, 132] and the Boltzmann-based parton cascade model BAMPS [133], but had not been explored in the Langevin approach prior to our studies [134, 107].

In this dissertation, we study heavy quark evolution and energy loss in a hot and dense QGP medium within the framework of a Langevin equation. In addition to the drag and thermal forces for quasi-elastic scattering in the classical Langevin equation, a recoil term is introduced to describe the force exerted on heavy quarks due to gluon radiation. This recoil force is then related to the medium-induced gluon radiation spectrum, which is taken from a higher-twist energy loss calculation [84, 135, 122, 136]. Within this improved approach, the evolution of heavy quarks inside QGP fireballs is studied, and the significance of the medium-induced gluon radiation is observed, especially for heavy quarks with large transverse momenta.

To compare with experimental data, one needs to convert bare quarks into hadronic bound states. This conversion process may result in a qualitative difference between the spectra of bare quarks and their mesonic bound states especially at lower to intermediate p_{T} and therefore is also crucial for understanding heavy flavor phenomenology. The hadronization of heavy quark is governed by two mechanisms: high momentum heavy quarks tend to fragment directly into heavy hadrons, whereas low momentum ones coalesce with thermal light quarks from the medium to form new hadrons. In this dissertation, we construct a hybrid fragmentation plus recombination model to describe the hadronization process of heavy quarks when they reach the freeze-out hypersurface of the QGP medium. The fragmentation process is simulated with the Monte-Carlo event generator PYTHIA 6.4 [137], and the heavy-light quark recombination process is calculated with an "instantaneous coalescence" approach based on Ref. [105]. This approach was first developed for light hadron production from the QGP [138, 31, 139, 140], and then applied to heavy quark hadronization [103, 104, 105] and recently to partonic jet hadronization [141] as well. This coalescence model does not require the thermalization of the recombining partons and it is straightforward to include mesons and baryons simultaneously, thus it is convenient for the normalization over all possible hadronization channels. Note that other approaches, such as the resonance recombination model [101, 142, 106], have also been applied to the study of heavy flavor dynamics. With our hybrid hadronization model, we will show that while the fragmentation mechanism dominates D meson spectra at high p_{T}, the coalescence mechanism brings low p_{T} heavy quarks to medium p_{T} hadrons and significantly enhances D meson production in the latter regime for nucleus-nucleus collisions. This will impact the patterns of the D meson R_{AA} and v_2 that we observe.

After the decay of the QGP, interactions still exist between heavy mesons and the hadron gas although they are expected to be weaker than those inside the QGP

matter. We incorporate these hadronic interactions into our framework by using the Ultra-relativistic Quantum Molecular Dynamics (UrQMD) model developed in Ref. [36] which simulates many body interactions between hadrons. The scattering cross sections between D meson and π and ρ mesons are introduced based on the calculations in Ref. [143]. We will show that these hadronic interactions further suppress the D meson $R_{\rm AA}$ at high $p_{\rm T}$ and enhance its v_2 due to the additional energy loss of D mesons inside the hadron gas.

Within our newly developed framework, we are able to simulate the full evolution history of heavy flavor in heavy-ion collisions: initial production of heavy quarks, energy loss in the QGP, hadronization to heavy mesons and in the end rescattering inside the hadron gas. Our calculations provide good descriptions of the D meson suppression and flow that are observed at both RHIC and LHC experiments. Meanwhile, we also provide various predictions for future measurements, such as the B meson suppression and flow coefficients, dependence of the D meson $R_{\rm AA}$ on the participant number, and the non-photonic electron $R_{\rm AA}$ and v_2 observed at relatively low energy (62.4 GeV) Au-Au collisions. Furthermore, we extend our study from the single inclusive spectra of heavy flavor hadrons and non-photonic electrons to correlation functions of heavy flavor pairs and find that the investigation of the heavy-flavor-tagged angular correlation may help us better distinguish between different energy loss mechanisms of heavy quark inside the QGP. Our study provides an important step forward in the quantitative understanding of the heavy flavor dynamics in heavy-ion collisions and helps make it a more controllable tool to probe QGP properties.

1.4.2 Heavy Quarkonium in the QGP

In addition to open heavy quarks and mesons, heavy quarkonium is the other important branch of heavy flavor probes of QGP properties. Quarkonia are a special

species of hadrons. Among the vector (spin-one) charmonium states, the lightest (ground state) is the famous J/ψ; the excited states are the χ_c and the ψ'. For the bottom quark, the lightest quarkonium is the Υ, while the excited states include the χ_b, Υ', χ_b' and the Υ''. The stability of the $c\bar{c}/b\bar{b}$ quarkonium states implies that their masses satisfy $M_{c\bar{c}} < 2M_D$ and $M_{b\bar{b}} < 2M_B$. One of the most important features of quarkonia is their small size or large binding energy. Compared with the typical hadron radius 1 fm (or the typical hadronic scale $\Lambda_{\rm QCD} \sim 0.2$ GeV), the radii of J/ψ and Υ ground states are around 0.1 and 0.2 fm respectively (with binding energies around 0.6 and 1.2 GeV) [11]. This indicates that they can still survive in a QGP within a certain range of temperatures above $T_{\rm c}$. However, the higher excited states of quarkonia are less tightly bounded and have larger sizes although being still more stable than usual light hadrons. As a result, with an increase of the QGP temperature, the different quarkonium states will dissociate sequentially – loosely bounded states melt first. Therefore, by observing the surviving quarkonium states, we are able to extract temperature information of the QGP. In this way, the sequential melting of different heavy quarkonia states serves as a QGP thermometer [144, 145].

In Fig.1.11, we show an example of sequential Υ melting measured by the CMS collaboration, comparing between spectra obtained from proton-proton collisions and Pb-Pb collisions [147, 146]. The existence of the Υ ground and excited states can be seen in the resonant peaks of the invariant mass spectra of their $\mu^+\mu^-$ decay products. We see that there are three distinct peaks in the left figure for the proton-proton collision, representing $\Upsilon(1S)$, $\Upsilon(2S)$ and $\Upsilon(3S)$ states. However, in the right figure for the Pb-Pb collision, while the $\Upsilon(1S)$ state still apparently exists, the peak for the $\Upsilon(2S)$ state is significantly suppressed and the $\Upsilon(3S)$ state entirely disappears. This can be viewed as a "smoking gun" that a hot and dense nuclear matter is created in the ultrarelativistic Pb-Pb collision whose maximum temperature

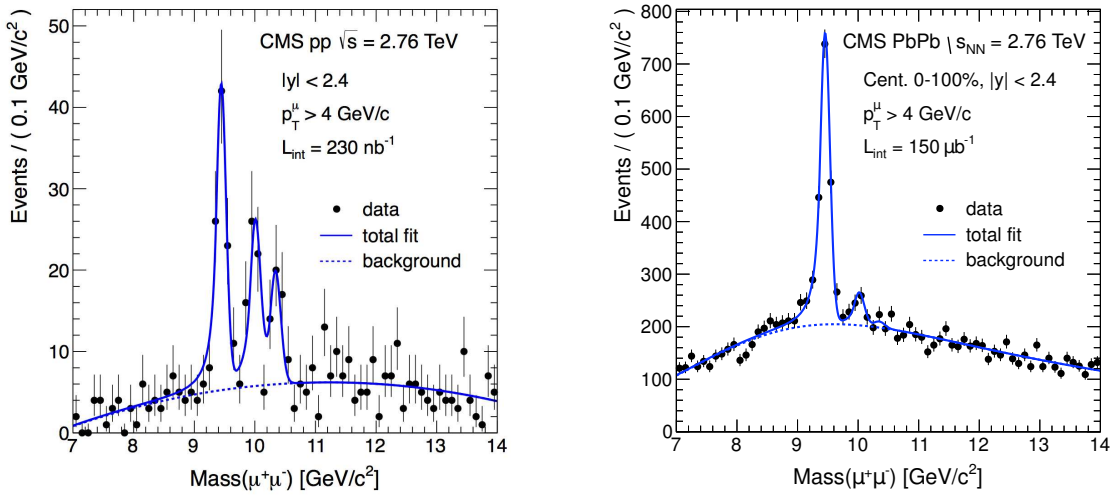

FIGURE 1.11: Sequential melting of Υ states: left for spectra obtained in proton-proton collision as a baseline reference, and right for spectra obtained in $\sqrt{s_{\rm NN}}$ = 2.76 TeV Pb-Pb collision. These two figures are taken from Ref. [146].

is between the dissociation temperatures of $\Upsilon(2S)$ and $\Upsilon(1S)$. From theory, one may obtain the binding energy $\epsilon(T)$, the average size $\langle r\rangle(T)$ and the dissociation temperature $T_{\rm d}$ of each quarkonium state by either solving the Schrödinger equation with proper assumptions for the $Q\bar{Q}$ potential [11, 148, 149] or by directly calculating the quarkonium spectra on the lattice [150, 151, 152, 153, 154, 155, 156].

Similar to open heavy flavor, one can calculate the nuclear modification factor $R_{\rm AA}$ and the elliptic flow coefficient v_2 of heavy quarkonium. However, a quantitative description of these suppression and flow patterns [157, 158, 159, 160] involves a number of extra ingredients: apart from the aforementioned quarkonium dissociation which is microscopically caused by either scattering or gluon absorption, the reverse process – regeneration of quarkonium from open heavy quarks – should be taken into account as well, and furthermore one also needs to consider the feed down contribution to lower mass resonant states from their higher excited states. In particular, the regeneration process of quarkonium bound states from the uncorrelated open heavy quarks produced in the initial hard scatterings has been recently found

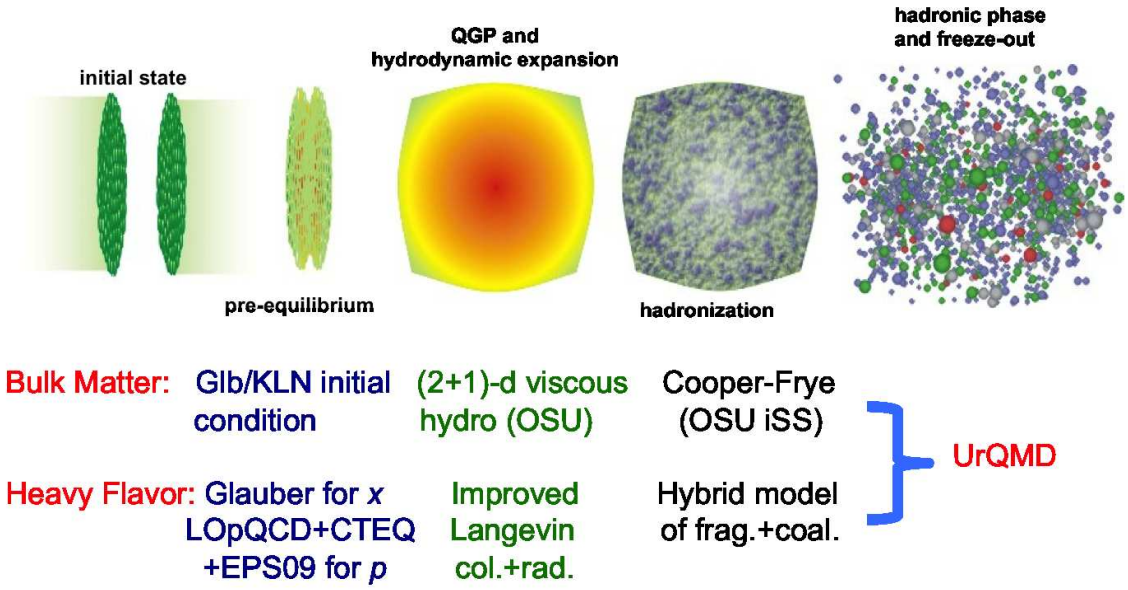

FIGURE 1.12: An overview of our theoretical framework of heavy flavor dynamics in heavy-ion collisions.

to be extremely important for the quarkonium phenomenology, especially for the LHC experiments in which abundant open heavy quarks can be produced in each collision event and therefore the regeneration probability is significantly increased [161, 162, 163, 164, 165, 166].

1.5 Outline of the Dissertation

In this dissertation, we will establish a comprehensive framework that describes the full time evolution of heavy flavor, which can be utilized to probe the transport properties of the QGP created in relativistic heavy-ion collisions. The structure of our numerical framework, and the outline of this dissertation as well, can be summarized by Fig.1.12. We use either the Glauber or the KLN model to prepare the initial conditions for the hydrodynamical expansion of the QGP. At the same time, the initial heavy quark production is calculated using the Glauber model in

position space and a pQCD method in momentum space. During the QGP evolution, the bulk matter evolves according to hydrodynamics and the heavy quark dynamics is described by our modified Langevin equation that incorporates both collisional and radiative energy loss of heavy quarks in a QGP. At the critical temperature T_c, both the bulk matter and heavy quark hadronize: while light hadrons are sampled from the QGP medium according to the Cooper-Frye formula, heavy quarks are converted into their mesonic bound states with our hybrid fragmentation plus recombination model. In the end, all the produced hadrons are placed into the UrQMD model for the simulation of their subsequent hadronic interactions until the kinetic freeze-out. Note that this framework is designed such that any of the above mentioned pieces can be easily substituted by other models – e.g. a different hydrodynamic background, a different heavy quark transport model, or a different hadronization approach – so that a systematic comparison between different studies of heavy flavor dynamics can be implemented conveniently in the future.

In Chapter 2, we will discuss how the MC-Glauber model is utilized in our study to initialize the position space distribution of the heavy quark production and how a leading-order pQCD calculation is implemented for its initial p_T spectra. The pQCD calculation is at the partonic level. We use the parton distribution function CTEQ5 for nucleon-nucleon collision. For nucleus-nucleus collision we modify the parton distribution function with the EPS parametrizations to take into account the nuclear shadowing effect in the initial state. We will show that this nuclear shadowing effect significantly suppresses the production rate of charm quarks at low p_T but slightly enhances it at larger p_T at both RHIC and LHC energies in nucleus-nucleus collisions with respect to proton-proton collisions. The impact is weaker for bottom quarks but is still non-negligible.

In the following two chapters we will study the heavy quark evolution inside a QGP medium within the framework of the Langevin equation coupled to a hydro-

dynamic background. In Chapter 3, we will concentrate on the collisional energy loss and in Chapter 4 the radiative energy loss will be introduced. We will start with a detailed review of different transport equations for heavy quarks in Chapter 3 and show that in the limit of small momentum change in each interaction the Boltzmann equation for heavy quark can be reduced to the Fokker-Plank equation and furthermore be stochastically realized with the Langevin equation. After that we will discuss how the Langevin equation is applied to heavy quark transport in a dynamic QGP medium and use it to investigate (1) the thermalization process of charm quarks inside the QGP, and (2) how the collisional energy loss of heavy quark depends on different transport coefficients and various properties of the QGP fireball such as its geometric anisotropy and collective flow behavior. In Chapter 4 we will modify the classical Langevin equation so that gluon radiation can be incorporated as well. With this improved equation, we will show that while the collisional energy loss dominates the observed heavy flavor spectra at low p_{T}, gluon radiation dominates the high p_{T} regime – the crossing points are around 6 GeV for charm quarks and 16 GeV for bottom quarks. As a result, even though the collisional energy loss mechanism alone may work well to describe the early RHIC data at low p_{T}, it becomes insufficient to describe the LHC observations. As an application of this improved Langevin equation, we will explore the impact of initial state fluctuations in heavy-ion collisions on heavy quark energy loss. Our calculation will demonstrate that although the total energy loss of heavy quarks is not very sensitive to the size of local fluctuations in a 2-dimensional system, it increases significantly with the number of hot spots. Our simulation in a realistic QGP medium will show that fluctuating initial conditions may bring about 10% more suppression for inclusive charm quark production at high p_{T} in central Pb-Pb collisions, implying that jet modification might be utilized to probe the initial fluctuations in heavy-ion collisions such as the degree of inhomogeneity or the number of hot spots.

In Chapter 5, we will develop a hybrid fragmentation plus recombination model to describe the hadronization process of heavy quarks to their hadronic bound states. After briefly reviewing the fragmentation functions selected for heavy quarks in PYTHIA, we will discuss in detail how the instantaneous coalescence model is constructed and how the hybrid model of the two hadronization mechanisms is established. Within our hybrid model, we will show that while the fragmentation mechanism dominates the heavy meson formation at large p_{T}, the coalescence mechanism significantly enhances its production at intermediate p_{T}. By attaching this hadronization process to our model of heavy quark transport, our calculations will be able to provide a good description of the D meson suppression and flow observed at both RHIC and LHC. In addition, we will also provide our predictions for B mesons and several other upcoming measurements of heavy flavor.

To complete the description of the full evolution history of heavy flavor, in Chapter 6, we will study the scatterings between heavy mesons and the hadron gas in the hadronic phase and investigate how these interactions further affect the observed heavy meson spectra. We will first review how soft hadrons are emitted from the QGP medium on the transition hypersurface according to the Cooper-Frye formula. After that, we will discuss how the many body interactions between hadrons are simulated in the UrQMD model and how the scattering cross sections for charm mesons are introduced. Our calculations will show that these hadronic interactions further suppress the D meson R_{AA} at large p_{T} and enhance its v_2. As a final example, we will apply this complete framework to an exploration of new heavy flavor observables. We will introduce heavy-flavor-tagged angular correlation functions and show that while inclusive spectra are insufficient to help us distinguish between different energy loss mechanisms of heavy quarks inside the QGP, the correlation functions may provide us with better insights.

In Chapter 7, we will summarize this dissertation and provide an outlook for

our future work including several directions for further improvement of the current framework of heavy flavor dynamics and possible additional fields of study that can be explored with our numerical framework.

2

Initial Production of Heavy Quarks

Because of their large mass threshold, the majority of heavy quarks are produced via hard scatterings at the early stage of relativistic heavy-ion collisions. Contributions from other processes such as the "intrinsic heavy quark process" (liberation of $Q\bar{Q}$ fluctuations from the projectile wavefuntion due to its scatterings inside the target) [167, 168], pre-thermal and thermal production [169, 170, 171], and in-medium jet conversion [172, 171] have been studied and shown to be small. In this work, we use a Monte-Carlo (MC) Glauber model [15] to sample the spatial distribution of the production vertices of heavy quarks in nucleus-nucleus collisions. For the momentum space, we calculate the initial heavy quark distributions using a leading-order perturbative QCD approach [173] with the incorporation of $gg \to Q\bar{Q}$ and $q\bar{q} \to Q\bar{Q}$ processes. For the calculation of partonic cross sections, we utilize the CTEQ parametrization for the parton distribution functions [174] and include the nuclear shadowing effect in nucleus-nucleus collisions using the EPS parametrization [175, 176].

In this chapter, we will first review the Glauber model in high energy nucleus-nuclues collisions. After that, we will discuss the pQCD method we adopt for the

initialization of heavy quark momentum space. Finally, we will show the p_{T} spectra we obtain for both charm and bottom quarks.

2.1 The Glauber Model

The Glauber model is base on the assumption that the collision of two nuclei can be viewed as superposition of independent interactions of nucleon pairs. At sufficiently high energies, these nucleons will move in straight lines instead of being deflected when interacting with each other. These simplifications will lead to concise analytical results for the nucleus-nucleus cross section, binary collision number, and participant number in the Optical Glauber Model (Sec.2.1.2), and a straightforward numerical simulation – the MC Glauber Model (Sec.2.1.3). This section is mostly based on Ref. [15].

2.1.1 Input into the Glauber Model

Before discussing the two realizations of the Glauber model, we first briefly review the two most important inputs of the model – the nucleon density of the nucleus and the inelastic nucleon-nucleon cross section – which should both be fixed by experiments.

The nuclear density distribution of the nucleus is usually parametrized using the Woods-Saxon distribution

$$\rho(r) = \rho_0 \frac{1 + w(r/R)^2}{1 + \exp(\frac{r-R}{a})}, \tag{2.1}$$

in which ρ_0 represents the nucleon density at the center of the nucleus, R is the nuclear radius, a is called the "skin depth" and w encodes information of the deviation of the nucleus from the spherical shape. For ^{197}Au and ^{207}Pb nuclei we discuss in this dissertation, w can be taken as 0. For ^{197}Au, we have $\rho_0 = 0.1693$, $R = 6.38$ fm, $a = 0.535$ fm; for ^{207}Pb, we have $\rho_0 = 0.1693$, $R = 6.62$ fm, $a = 0.546$ fm. Note that here we have normalized the spatial integral of $\rho(r)$ to 1.

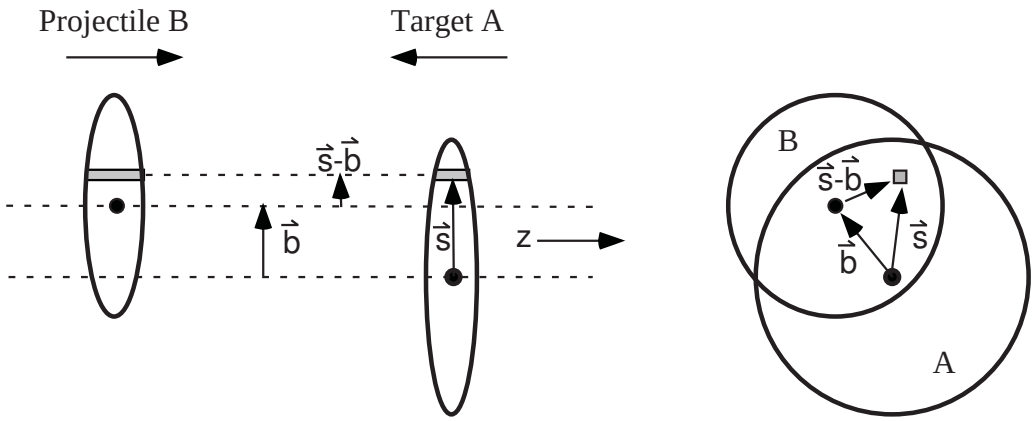

FIGURE 2.1: Demonstration of the geometry of the Optical Glauber Model: (a) for the side view and (b) for the beam-line view. This figure is taken from Ref. [15].

Apart from the nuclear density distribution, the other input of the Glauber model is the inelastic nucleon-nucleon cross section $\sigma_{\rm inel}^{\rm NN}$. Since this cross section involves processes at all momentum transfers, it cannot be directly calculated using pQCD and therefore should also be determined by measurements. For $\sqrt{s_{\rm NN}}$ =2.76 TeV (the LHC energy), we use $\sigma_{\rm inel}^{\rm NN}$ =64 mb, and for $\sqrt{s_{\rm NN}}$ =200 GeV and 62.4 GeV (the RHIC energies), we have $\sigma_{\rm inel}^{\rm NN}$ =42 mb and 36 mb respectively.

2.1.2 The Optical Glauber Model

The geometrical setup of the Optical Glauber Model is shown in Fig.(2.1), where two nuclei A and B collide with an impact parameter of $\vec{b}$. One may first focus on the two tubes located at $\vec{s}$ with respect to the center of A (or $\vec{s}-\vec{b}$ from the center of B). In these two tubes, the probability of finding a nucleon from A per unit transverse area is defined as

$$\hat{T}_{\rm A}(\vec{s}) = \int \hat{\rho}_{\rm A}(\vec{s}, z_{\rm A}) dz_{\rm A}, \tag{2.2}$$

in which $\hat{\rho}_{\rm A}(\vec{s}, z_{\rm A})$ is the nuclear density distribution discussed in Eq.(2.1). Similarly, at that colliding point, we have

$$\hat{T}_{\rm B}(\vec{s}-\vec{b}) = \int \hat{\rho}_{\rm B}(\vec{s}-\vec{b}, z_{\rm B}) dz_{\rm B}, \tag{2.3}$$

for nucleus B. And the product $\hat{T}_{\rm A}(\vec{s})\hat{T}_{\rm B}(\vec{s}-\vec{b})$ then provides the joint probability per unit area of finding a nucleon from both A and B in the selected tubes. One may further integrate this product over the area element and obtain a "thickness function" as

$$\hat{T}_{\rm AB}(\vec{b}) = \int \hat{T}_{\rm A}(\vec{s})\hat{T}_{\rm B}(\vec{s}-\vec{b}) d^2s. \tag{2.4}$$

This thickness function has the dimension of an inverse area and thus might be understood as the effective overlap area for which a nucleon from A can interact with a nucleon from B. A product with the inelastic cross section $\hat{T}_{\rm AB}(\vec{b})\sigma_{\rm inel}^{\rm NN}$ then provides the probability of this hard scattering.

With this probability for a nucleon-nucleon interaction, it is straightforward to obtain the probability for an inelastic nucleus-nucleus interaction with an impact parameter of $\vec{b}$ as

$$\frac{d^2\sigma_{\rm inel}^{\rm AB}}{d^2b} = 1 - \left[1 - \hat{T}_{\rm AB}(\vec{b})\sigma_{\rm inel}^{\rm NN}\right]^{AB}, \tag{2.5}$$

in which we use A and B to denote the number of nucleons in A and B respectively. After integrating over the transverse plane spanned by the impact parameter, one obtains the total cross section of nucleus-nucleus inelastic interaction:

$$\sigma_{\rm inel}^{\rm AB} = \int_0^\infty 2\pi b db \left\{1 - \left[1 - \hat{T}_{\rm AB}(\vec{b})\sigma_{\rm inel}^{\rm NN}\right]^{AB}\right\}. \tag{2.6}$$

Meanwhile, we have the total number of nucleon-nucleon collisions (or the binary collision number) as

$$N_{\rm coll}(\vec{b}) = AB\hat{T}_{\rm AB}(\vec{b})\sigma_{\rm inel}^{\rm NN}, \tag{2.7}$$

considering that there exist AB possible nucleon pairs with the probability of binary collision between each of them as $\hat{T}_{\rm AB}(\vec{b})\sigma_{\rm inel}^{\rm NN}$. This binary collision number is directly related to the production rate of heavy quarks – the number of heavy quarks produced in the initial hard scatterings of each nucleus-nucleus collision can be evaluated as

$$N_{\rm HQ} = N_{\rm coll}\frac{\sigma^{\rm NN\to HQ}}{\sigma_{\rm inel}^{\rm NN}}. \tag{2.8}$$

While the production of hard particles is dominated by this binary collision number, there exists another important quantity – the participant number – which is responsible for the production of the QGP medium and therefore the soft particles. The "participant number" is defined as the number of nucleons which participate in the binary collisions. Analogous to the above discussion, the probability for a nucleon in A to interact with nucleus B (i.e., at least one nucleon in B) can be written as

$$\int \hat{T}_{\rm A}(\vec{s})\left\{1-\left[1-\hat{T}_{\rm B}(\vec{s}-\vec{b})\sigma_{\rm inel}^{\rm NN}\right]^{B}\right\}d^2s. \tag{2.9}$$

And therefore, the participant number reads

$$\begin{aligned} N_{\rm part}(\vec{b}) &= A\int \hat{T}_{\rm A}(\vec{s})\left\{1-\left[1-\hat{T}_{\rm B}(\vec{s}-\vec{b})\sigma_{\rm inel}^{\rm NN}\right]^{B}\right\}d^2s \\ &\quad + B\int \hat{T}_{\rm B}(\vec{s}-\vec{b})\left\{1-\left[1-\hat{T}_{\rm A}(\vec{s})\sigma_{\rm inel}^{\rm NN}\right]^{A}\right\}d^2s, \end{aligned} \tag{2.10}$$

More discussions can be found in Refs. [14, 177].

2.1.3 The Monte-Carlo Glauber Model

Apart from the above analytical evaluation of the binary collision number and participant number in nucleus-nucleus collision, one may also numerically simulate the scattering process with a Monte-Carlo method.

To begin with, with a chosen impact parameter b, we sample the initial positions of A nucleons for nucleus A and B nucleons for B according to their density distribution functions Eq.(2.1). Then nuclei A and B are assumed to move towards each other along a straight line. At the time of overlap, one loops each nucleon in A over each one in B. If the distance between a nucleon-nucleon pair satisfies the criterion

$$d \leq \sqrt{\sigma_{\rm inel}^{\rm NN}/\pi}, \tag{2.11}$$

a hard scattering is considered to take place. The positions where binary collisions take place are recorded and utilized as the production vertices for heavy quarks. Meanwhile, one may count the number of binary collisions and participant nucleons for each nucleus-nucleus collision event directly with this MC Glauber method. The MC model provides initial conditions for the hydrodynamical evolution of the QGP medium as well. However, unlike heavy quarks, not only the binary collision number density, but also the participant number density should be taken into account for the initial energy/entropy density of the bulk matter, as will be shown in the next subsection.

Unlike the optical form of the Glauber model that is based on continuous nucleon density functions, the MC Glauber model locates nucleons at specific positions for each event which vary from event to event. This captures the feature of quantum fluctuation in the initial state of nucleus-nucleus collision. As discussed in Ref. [15], the two realizations of the Glauber model provide similar nucleus-nucleus cross sections when $\sqrt{\sigma_{\rm inel}^{\rm NN}}$ is small, but will slightly deviate as $\sqrt{\sigma_{\rm inel}^{\rm NN}}$ increases – the MC simulation may introduce a "shadowing" correction that reduces the cross section compared to the optical model.

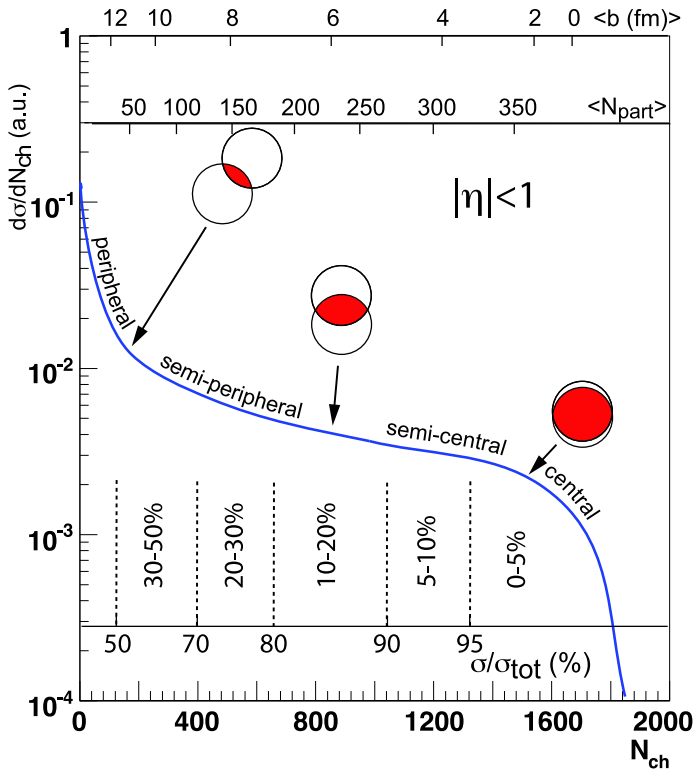

FIGURE 2.2: A cartoon demonstration of how to relate the final state observables ($N_{\rm ch}$) to quantities provided by the Glauber Model (b, $N_{\rm part}$). This figure is taken from Ref. [15].

2.1.4 Relating the Glauber Model to Experimental Data

In the experiment, we are not able to determine the impact parameter, participant number or binary collision number of the collision event. One way to construct a bridge between the Glauber model and experimental observations is through the concept of "centrality" as illustrated in Fig.2.2.

In experiments, one may measure the charged particle multiplicity distribution ($dN_{\rm vet}/dN_{\rm ch}$) as a function of the number of charged particles observed in the final state ($N_{\rm ch}$). This leads to the horse-back-shaped curve in Fig.2.2. The limit with 0 multiplicity of charged particles corresponds to the most peripheral collision (i.e., large impact parameter or small participant number). This leads to large $dN_{\rm vet}/dN_{\rm ch}$

(or $d\sigma/dN_{\rm ch}$) value since the probability for such event to take place is large. On the other hand, the events with the largest final $N_{\rm ch}$ corresponds to the head-on collision ($b = 0$), which has zero probability due to geometry. With this curve, one may then divide $N_{\rm ch}$ into "centrality regions" from right to left according to the fractional integrated area under the curve. For instance, 0-5% centrality corresponds to the region starting from the right that takes 5% of the integrated area under the $dN_{\rm vet}/dN_{\rm ch}$ curve, and is also referred to as the "central collision region". On the other hand, a centrality over 50% corresponds to the "peripheral collision region".

On the theory side, one may start with an ansatz that the number of charged particles in the final state is proportional to the following linear combination of binary collision number and participant number (i.e., hard processes and soft processes) [178, 43]:

$$N_{\rm ch}^{\rm AA}(b,\Delta\eta) = \left[\alpha N_{\rm coll}(b) + \frac{1-\alpha}{2} N_{\rm part}(b)\right] N_{\rm ch}^{\rm NN}(b,\Delta\eta), \tag{2.12}$$

In which $N_{\rm ch}^{\rm AA}(b,\Delta\eta)$ and $N_{\rm ch}^{\rm NN}(b,\Delta\eta)$ are the number of charged particles produced in a nucleus-nucleus collision and a nucleon-nucleon collision respectively. With this ansatz, we may calculate $dN_{\rm vet}^{\rm AA}/dN_{\rm ch}$ vs. $N_{\rm ch}^{\rm AA}$ (Fig.2.2) with $N_{\rm coll}$ and $N_{\rm part}$ obtained from the MC Glauber model. By comparison to the experimental data, we can fix the parameter α in Eq.(2.12) and then relate different centrality bins to regions of either impact parameter or participant number.

2.2 Initialization of the Momentum Space

2.2.1 A Leading-order pQCD Calculation

A variety of different approaches can be applied to the initialization of heavy quarks in momentum space. In our earlier work, we used either a parton cascade model (see Sec.3.2) or a simple parametrization (see Sec.3.3) to initialize heavy quarks. For most of our later calculations in this thesis, the initial momentum space distribution

is described by a leading-order pQCD calculation. Of course, while this method is sufficient for the description of heavy flavor single particle spectra (e.g., suppression and flow observables), it may not be a good choice for the study of correlation functions, since it does not include the process of gluon splitting. For this specific purpose, we will utilize a Monte-Carlo next-to-leading-order (MCNLO) calculation for the momentum space initialization in Sec.6.3.

For most of our calculations, we utilize the leading-order processes $q\bar{q} \to Q\bar{Q}$ and $gg \to Q\bar{Q}$ for the heavy quark production. The related matrix elements for these are adopted from Ref. [173]:

$$\Sigma \left|\mathcal{M}_{q\bar{q}\to Q\bar{Q}}\right|^2 = \frac{64}{9}\pi^2\alpha_s^2(M_{\rm T})\frac{(M^2-t)^2+(M^2-u)^2+2M^2s}{s^2}, \tag{2.13}$$

$$\begin{aligned}\Sigma \left|\mathcal{M}_{gg\to Q\bar{Q}}\right|^2 = \pi^2\alpha_s^2(M_{\rm T})\Bigg[&\frac{12}{s^2}(M^2-t)(M^2-u)\\ &+\frac{8}{3}\frac{(M^2-t)(M^2-u)-2M^2(M^2+t)}{(M^2-t)^2}\\ &+\frac{8}{3}\frac{(M^2-t)(M^2-u)-2M^2(M^2+u)}{(M^2-u)^2}\\ &-\frac{2}{3}\frac{M^2(s-4M^2)}{(M^2-t)(M^2-u)}\\ &-6\frac{(M^2-t)(M^2-u)+M^2(u-t)}{s(M^2-t)}\\ &-6\frac{(M^2-t)(M^2-u)+M^2(t-u))}{s(M^2-u)}\Bigg],\end{aligned} \tag{2.14}$$

where the squares of the matrix elements have been summed over color and spin degrees of freedom of the final states and averaged over the initial states. In Eqs.(2.13) and (2.14), α_s is the strong coupling constant, M is the mass of heavy quark, $M_{\rm T}$ is the transverse mass defined as $\sqrt{M^2+p_{\rm T}^2}$ and s, t, u are the Mandelstam variables. The above two matrix elements are utilized to calculate the initial momenta of heavy

quarks.

Apart from these two processes, which are termed as the "flavor creation" processes, one may also include "flavor excitation" processes – $qQ \to qQ$ and $gQ \to gQ$ – in which a heavy quark from the sea is excited by a hard scattering with a parton. The corresponding matrix elements can also be found in Ref.[173]:

$$\Sigma \left|\mathcal{M}_{qQ\to qQ}\right|^2 = \frac{64}{9}\pi^2\alpha_s^2(M_{\rm T})\frac{(M^2-u)^2+(s-M^2)^2+2M^2t}{t^2}, \tag{2.15}$$

$$\begin{aligned}\Sigma \left|\mathcal{M}_{gQ\to gQ}\right|^2 = \pi^2\alpha_s^2(M_{\rm T})\Bigg[&\frac{32}{t^2}(s-M^2)(M^2-u)\\ &+\frac{64}{9}\frac{(s-M^2)(M^2-u)+2M^2(s+M^2)}{(s-M^2)^2}\\ &+\frac{64}{9}\frac{(s-M^2)(M^2-u)+2M^2(M^2+u)}{(M^2-u)^2}\\ &+\frac{16}{9}\frac{M^2(4M^2-t)}{(s-M^2)(M^2-u)}\\ &+16\frac{(s-M^2)(M^2-u)+M^2(s-u)}{t(s-M^2)}\\ &-16\frac{(s-M^2)(M^2-u)-M^2(s-u))}{t(M^2-u)}\Bigg],\end{aligned} \tag{2.16}$$

These flavor excitation processes will be incorporated in a future project and are beyond the discussion in this dissertation.

2.2.2 Parton Distribution Function and Nuclear Shadowing Effect

In the previous subsection, we have summarized the heavy quark production via hard scatterings between partons in leading-order pQCD. To obtain the spectra of heavy quark produced in nucleon-nucleon collision or nucleus-nucleus collision, one requires in addition the information on the momentum distribution of partons in a nucleon, i.e, the parton distribution function (PDF).

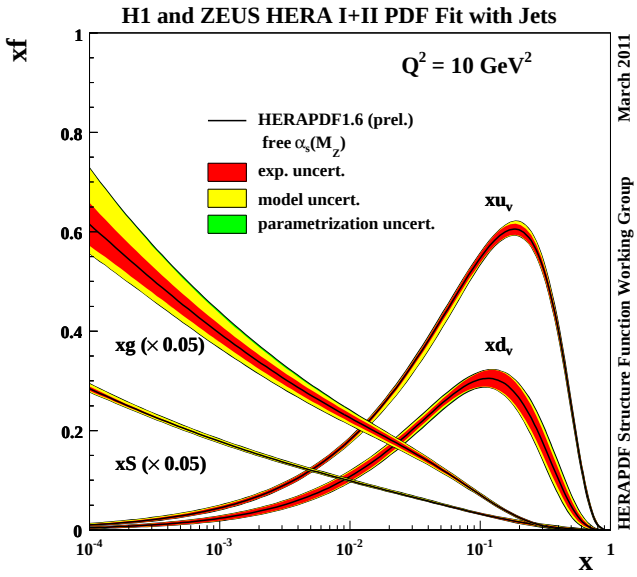

FIGURE 2.3: Demonstration of the parton distribution functions of gluon, valence quarks and sea quarks. This figure is taken from Ref. [179].

As illustrated by Fig.2.3, the PDFs $f_i(x, Q^2)$ provides the probability of finding a parton (valence/sea quark or gluon) in a nucleon with a fractional momentum x (the ratio between the momentum of the parton and that of the nucleon). Here, Q is the energy scale of the hard interaction. Then the cross sections of all processes in a nucleon-nucleon collision can be calculated by convoluting the cross sections at parton level with these PDFs. Note that QCD itself does not predict these PDFs and they needs to be determined by a fit to data from experimental observations [mainly the deep inelastic scattering (DIS)] [179]. In this work, we shall adopt the CTEQ parton distributions [174] in our calculation.

While the above mentioned CTEC PDFs can be directly applied to nucleon-nucleon collisions, for nuclear interactions, one also needs to consider the modification to these nucleon PDFs due to the nucleons being bound in a nucleus. Such modifications are usually termed as "nuclear shadowing effect" or "cold nuclear matter

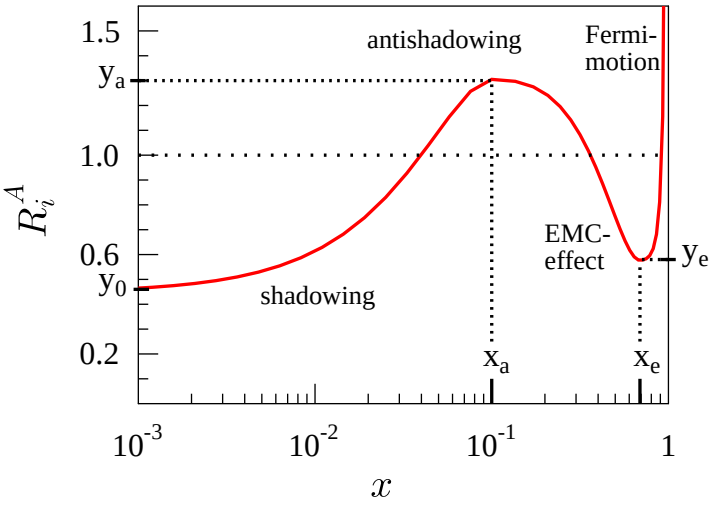

FIGURE 2.4: Demonstration of the nuclear shadowing effect. This figure is taken from Ref. [176].

effect" in the literature.

In Fig.2.4, we show a graph that helps illustrating the nuclear shadowing effect [176]. The function $R_i^{\rm A}(x,Q^2)$ is defined in

$$f_i^{\rm A}(x,Q^2) \equiv R_i^{\rm A}(x,Q^2) f_i^{\rm CTEQ}(x,Q^2), \tag{2.17}$$

and signifies the modification to the free proton PDF $f_i^{\rm CTEQ}$ in a nucleus (A). This functions may be parametrized as follows:

$$R_i^{\rm A}(x) = \begin{cases} a_0 + (a_1 + a_2 x)[\exp(-x) - \exp(-x_a)], & x \leq x_a, \\ b_0 + b_1 x + b_2 x^2 + b_3 x^3, & x_a \leq x \leq x_e, \\ c_0 + (c_1 - c_2 x)(1-x)^{-\beta}, & x_e \leq x \leq 1, \end{cases} \tag{2.18}$$

in which the parameters a_i, b_i, c_i, β, x_a and x_e depend on different nuclei species (A). By requiring that $R_i^{\rm A}(x,Q^2)$ is continuous and its first order derivative vanishes at the matching points x_a and x_e, 6 parameters out of the original 13 can be eliminated. The remaining 7 will be expressed in terms of the following 6 parameters together

with their intuitive interpretations:

y_0,	Height to which shadowing levels as $x \to 0$,
x_a, y_a,	Position and height of the antishadowing maximum,
x_e, y_e,	Position and height of the EMC minimum,
β,	Slope factor in the Fermi-motion part.

Note that c_0 is fixed as $c_0 = 2y_e$.

In the small x region, the probability for a probe particle to "see" the partons in the second nucleon in a nucleus might be reduced after its interaction with the previous one. In other words, the probing of the structure of a nucleon can be shielded by its neighbors in the nucleus. This is known as the "shadowing" region of $R_i^{\mathrm{A}}(x, Q^2)$. On the other hand, because of the conservation of energy and momentum of the target nucleon, if the probe particle "sees" less partons in the small x region, there must exist an enhancement of the parton distribution in the larger x region, which is called the "anti-shadowing effect". In the regime around $0.2 < x < 0.7$, a scaling violation of the nuclear structure function has been observed by the European Muon Collaboration – $F_2^{\mathrm{A}}(x, Q^2) < AF_2^{\mathrm{N}}(x, Q^2)$ [180, 181], which is termed as the "EMC effect". There is no universally accepted theoretical interpretation of this EMC effect at this moment and this topic is beyond the discussion of this dissertation. In the end, in the large x regime, due to the two-nucleon interaction in a nucleus which can be viewed as a fermi gas [182, 183], another rise of $R_i^{\mathrm{A}}(x, Q^2)$ is expected. Such effect can be even extended to the regime of $x > 1$ where three or more nucleon interactions are taken into account. This does not exist for partons in a free nucleon.

The parameters in Eq.(2.18) are fixed according to proton/deuteron-nucleus and lepton-nucleus deep inelastic scatterings. We use the EPS parametrization for the nuclear shadowing effect in this dissertation. Some of our earlier results were calculated with the EPS08 version [175] of the parametrization, and later we switched to an updated EPS09 version [176].

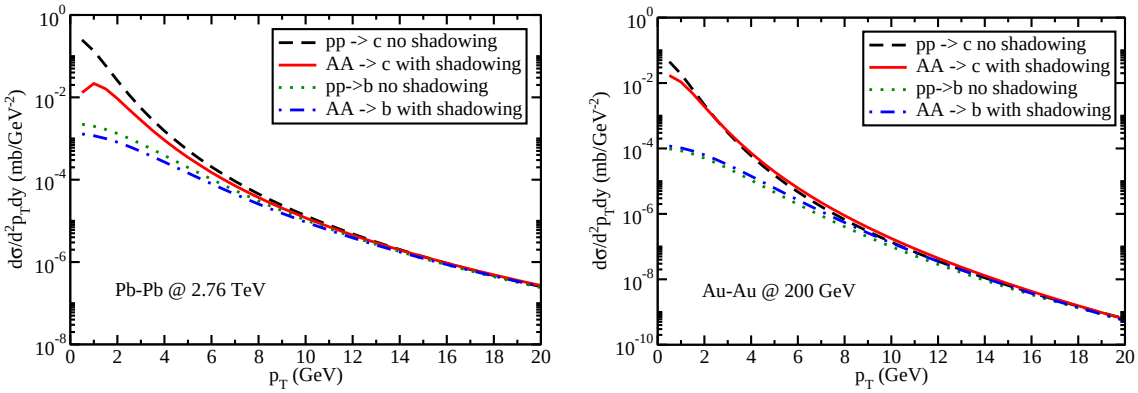

(a) (b)

FIGURE 2.5: Initial heavy flavor spectra from the leading-order pQCD calculation with and without the nuclear shadowing effect, (a) for LHC and (b) for RHIC.

2.2.3 Initial Spectra of Heavy Quarks

In Fig. 2.5 (taken from our published work [107]), we convolute the parton cross section (Sec.2.2.1) and the parton distribution function modified with the nuclear shadowing effect in nucleus-nucleus collisions (Sec.2.2.2), and show the transverse momentum distributions of initial heavy quarks in both proton-proton and binary collision number scaled nucleus-nucleus collisions at LHC and RHIC energies. One can observe from the figure the influence of the nuclear shadowing on the initial heavy quark spectra: it greatly reduces the production rate of charm quark in the low p_{T} region; the effect is stronger at the LHC than at RHIC. For the production of low p_{T} bottom quarks, this shadowing effect reduces the yield at the LHC energy but slightly enhances it at RHIC. This behavior will result in significant effects on the nuclear modification factor R_{AA} of heavy flavor hadrons as we will show in Sec.5.4. Note that the distributions in Fig.(2.5) are calculated with the EPS08 parametrization. In EPS09, the strength of the shadowing effect is reduced due to a tuning to more recent experimental data, but is still significant.

The above differential cross sections are evaluated at zero rapidity ($y = 0$). One may assume that the initial heavy quarks are uniformly distributed with respect to

the central rapidity region ($-1 < y < 1$) and we thus sample the initial transverse momentum p_{T} of heavy quarks in this region with a Monte-Carlo method according to the spectra provided in Fig.2.5 for either the proton-proton baseline or the nucleus-nucleus collision.

3

Heavy Quark Diffusion inside the QGP

In the limit of multiple scatterings where the momentum transfer in each interaction is small, the dynamical evolution of heavy quarks inside a thermalized QGP medium can be treated as Brownian motion which is typically described by the Langevin equation. We shall couple this Langevin equation to a hydrodynamic medium to study the quasi-elastic scattering of heavy quarks with light partons inside the QGP.

In this section, we will first summarize the transport theory of heavy quarks in a thermal medium and then develop a numerical framework where the Langevin evolution of heavy quarks is coupled to an expanding hydrodynamic medium. Within this Langevin framework, we present two of our studies: (1) the thermalization process of heavy quarks in a QGP medium (published in Ref. [184]), and (2) how the initial configuration of the QGP as well as its properties affect the suppression and the collective flow of the observed heavy mesons and their decay electrons (published in Ref. [185]).

3.1 Transport Equations of Heavy Quarks

In this subsection, we follow Ref. [123] and [102] to summarize the three frequently utilized transport equations for heavy quarks – the Boltzmann equation, the Fokker-Planck equation and the Langevin equation – and demonstrate the equivalence between them under certain conditions. We will show that the Fokker-Planck equation is the small-momentum-transfer limit of the Boltzmann equation, while the Langevin equation is a stochastic realization of the Fokker-Planck equation. After that, we will develop a numerical framework of the Langevin equation, in which it can be coupled to a hydrodynamic medium to describe the heavy quark evolution in a QGP.

3.1.1 The Boltzmann Equation

The evolution of the phase space distribution of heavy quarks $f_Q(t, \vec{x}, \vec{p})$ can be described by the Boltzmann equation as follows:

$$\frac{d}{dt} f_Q(t, \vec{x}, \vec{p}) = \left[\frac{\partial}{\partial t} + \frac{p_i}{E_{\vec{p}}} \frac{\partial}{\partial x_i} + F_i \frac{\partial}{\partial p_i} \right] f_Q(t, \vec{x}, \vec{p}) = C\left[f_Q\right], \tag{3.1}$$

where $E_{\vec{p}} = \sqrt{m_Q^2 + \vec{p}^2}$ is the energy of heavy quark with three momentum $\vec{p}$, $\vec{F}$ is the mean field force, and $C[f_Q]$ denotes the collision integral. Usually, two simplifications are applied – (a) the drift term, i.e., the mean field force $\vec{F}$ is neglected, and (b) the position space is integrated over first – and one obtains the following equation for the momentum distribution:

$$\frac{\partial}{\partial t} f_Q(t, \vec{p}) = C\left[f_Q\right], \tag{3.2}$$

where

$$f_Q(t, \vec{p}) \equiv \int d^3x f_Q(t, \vec{x}, \vec{p}). \tag{3.3}$$

The collision integral is defined as

$$C\left[f_Q\right] \equiv \int d^3k \left[w(\vec{p}+\vec{k},\vec{k})f_Q(\vec{p}+\vec{k}) - w(\vec{p},\vec{k})f_Q(\vec{p})\right], \tag{3.4}$$

where $w(\vec{p},\vec{k})$ denotes the transition rate for heavy quarks from momentum state $\vec{p}$ to $\vec{p}-\vec{k}$ due to their scatterings with the medium background. The first term on the right hand side of Eq.(3.4) represents the gain term of heavy quark from $\vec{p}+\vec{k}$ state to $\vec{p}$ state, while the second represents the loss term of heavy quark out of the $\vec{p}$ state.

The transition rate w can be further expressed in terms of the cross section of elastic scatterings between heavy quark and thermal partons (light quark or gluon) with momentum $\vec{q}$ inside QGP:

$$w(\vec{p},\vec{k}) = \gamma_{q,g}\int \frac{d^3q}{(2\pi)^3} f_{q,g}(\vec{q}) v_{\rm rel} d\sigma(\vec{p},\vec{q}\to\vec{p}-\vec{k},\vec{q}+\vec{k}), \tag{3.5}$$

where $f_{q,g}$ are the momentum distribution of thermal partons, $\gamma_q = 6$ and $\gamma_g = 16$ are the spin-color degeneracy of quark and gluon, and $v_{\rm rel}$ is the relative velocity defined as:

$$v_{\rm rel} \equiv \left|\frac{\vec{p}}{E_{\vec{p}}} - \frac{\vec{q}}{E_{\vec{q}}}\right| = \frac{\sqrt{(p\cdot q)^2 - (m_Q m_q)^2}}{E_{\vec{p}}E_{\vec{q}}}. \tag{3.6}$$

After summing the matrix element over the spin-color degeneracy of the final states and averaging over the initial states, the scattering cross section can be expressed as:

$$v_{\rm rel} d\sigma(\vec{p},\vec{q}\to\vec{p}',\vec{q}') =$$

$$\frac{1}{2E_{\vec{p}}2E_{\vec{q}}}\frac{d^3p'}{(2\pi)^3 2E_{\vec{p}'}}\frac{d^3q'}{(2\pi)^3 2E_{\vec{q}'}}\frac{1}{\gamma_Q\gamma_{q,g}}\sum|\mathcal{M}|^2(2\pi)^4\delta^{(4)}(p+q-p'-q'). \tag{3.7}$$

By substituting Eq.(3.5) and (3.7) into Eq.(3.4), we have

$$C\left[f_Q\right] = \frac{1}{2E_{\vec{p}}}\int\frac{d^3q}{(2\pi)^3 2E_{\vec{q}}}\int\frac{d^3p'}{(2\pi)^3 2E_{\vec{p}'}}\int\frac{d^3q'}{(2\pi)^3 2E_{\vec{p}'}}\frac{1}{\gamma_Q}\sum|\mathcal{M}|^2$$
$$\times(2\pi)^4\delta^{(4)}(p+q-p'-q')\left[f_Q(\vec{p}')f_{q,g}(\vec{q}')-f_Q(\vec{p})f_{q,g}(\vec{q})\right], \tag{3.8}$$

where we have let $\vec{p}' = \vec{p}-\vec{k}$ and $\vec{q}' = \vec{q}+\vec{k}$. Therefore, in principle, with the knowledge of the matrix element $\mathcal{M}$, the time evolution of the heavy quark distribution $f_Q(t,\vec{p})$ is determined by Eq.(3.2).

3.1.2 From the Boltzmann Equation to the Fokker-Planck Equation

In this subsection, we demonstrate that in the limit of small momentum transfers, the Boltzmann equation is reduced to the Fokker-Planck equation.

With the assumption that the momentum change of heavy quarks during each of their interactions with light partons is small, i.e., $|\vec{k}| \ll |\vec{p}|$, one may expand the right hand side of Eq.(3.4) with respect to $\vec{k}$ up to the second order:

$$w(\vec{p}+\vec{k},\vec{k})f_Q(\vec{p}+\vec{k}) \approx w(\vec{p},\vec{k})f_Q(\vec{p})$$
$$+k_i\frac{\partial}{\partial p_i}\left[w(\vec{p},\vec{k})f_Q(\vec{p})\right]+\frac{1}{2}k_ik_j\frac{\partial^2}{\partial p_i\partial p_j}\left[w(\vec{p},\vec{k})f_Q(\vec{p})\right]. \tag{3.9}$$

The collision integral is then simplified to

$$C\left[f_Q\right] \approx \int d^3k\left(k_i\frac{\partial}{\partial p_i}+\frac{1}{2}k_ik_j\frac{\partial^2}{\partial p_i\partial p_j}\right)w(\vec{p},\vec{k})f_Q(\vec{p}), \tag{3.10}$$

and thus the Boltzmann equation is reduced to the Fokker-Planck equation

$$\frac{\partial}{\partial t}f_Q(t,\vec{p}) = \frac{\partial}{\partial p_i}\left\{A_i(\vec{p})f_Q(t,\vec{p})+\frac{\partial}{\partial p_j}\left[B_{ij}(\vec{p})f_Q(t,\vec{p})\right]\right\}, \tag{3.11}$$

with the following definition of the drag and diffusion coefficients:

$$A_i(\vec{p}) = \int d^3k w(\vec{p},\vec{k})k_i,$$
$$B_{ij}(\vec{p}) = \frac{1}{2}\int d^3k w(\vec{p},\vec{k})k_ik_j. \tag{3.12}$$

If one defines

$$\langle X(\vec{p}')\rangle \equiv \frac{1}{2E_{\vec{p}}}\int\frac{d^3q}{(2\pi)^3 2E_{\vec{q}}}\int\frac{d^3p'}{(2\pi)^3 2E_{\vec{p}'}}\int\frac{d^3q'}{(2\pi)^3 2E_{\vec{q}'}}\frac{1}{\gamma_Q}\sum|\mathcal{M}|^2$$
$$\times(2\pi)^4\delta^{(4)}(p+q-p'-q')f_{q,g}X(\vec{p}'), \tag{3.13}$$

then Eq.(3.12) leads to

$$\begin{aligned} A_i(\vec{p}) &= \langle (p-p')_i \rangle\,, \\ B_{ij}(\vec{p}) &= \frac{1}{2}\langle (p-p')_i(p-p')_j \rangle\,, \end{aligned} \tag{3.14}$$

where k_i is substituted by $(p-p')_i$.

With the assumption that the medium background is in local equilibrium, rotational symmetry exists in the local rest frame of the heat bath, and therefore the directions of A_i and B_{ij} only depends on $\vec{p}$. This enables the following decomposition:

$$\begin{aligned} A_i(\vec{p}) &= A(\vec{p})p_i, \\ B_{ij}(\vec{p}) &= B_0(\vec{p})P^{\parallel}_{ij}(\vec{p}) + B_1(\vec{p})P^{\perp}_{ij}(\vec{p}), \end{aligned} \tag{3.15}$$

with the projection operators on the longitudinal and transverse directions of $\vec{p}$ defined as

$$P^{\parallel}_{ij}(\vec{p}) \equiv \frac{p_i p_j}{\vec{p}^2}, \qquad P^{\perp}_{ij}(\vec{p}) \equiv \delta_{ij} - \frac{p_i p_j}{\vec{p}^2}. \tag{3.16}$$

Consequently, the transport coefficients can be solved as follows:

$$\begin{aligned} A(\vec{p}) &= p_i A(\vec{p})^i/\vec{p}^2 = \left\langle 1 - \frac{\vec{p}\cdot\vec{p}'}{\vec{p}^2}\right\rangle, \\ B_0(\vec{p}) &= P^{\parallel}_{ij}B^{ij} = \frac{1}{2}\left\langle \frac{(\vec{p}\cdot\vec{p}')^2}{\vec{p}^2} - 2\vec{p}\cdot\vec{p}' + \vec{p}^2\right\rangle, \\ B_1(\vec{p}) &= \frac{1}{2}P^{\perp}_{ij}B^{ij} = \frac{1}{4}\left\langle \vec{p}'^2 - \frac{(\vec{p}\cdot\vec{p}')^2}{\vec{p}^2}\right\rangle, \end{aligned} \tag{3.17}$$

where the following identities have been applied:

$$P_{ij}^{\parallel}P_{\parallel}^{ij}=1,\qquad P_{ij}^{\perp}P_{\perp}^{ij}=2,\qquad P_{ij}^{\parallel}P_{\perp}^{ij}=0. \tag{3.18}$$

For a "minimal model", one may assume the transport coefficient of heavy quark in the longitudinal direction equals to that in the transverse direction, i.e., $B(\vec{p})\equiv B_0(\vec{p})=B_1(\vec{p})$, although they may not be exactly the same from the microscopic calculation. This results in $B_{ij}(\vec{p})=B(\vec{p})\delta_{ij}$. In addition, the transport coefficients $A(\vec{p})$ and $B(\vec{p})$ should only depend on the magnitude of the momentum (or energy), and therefore can be written as $A(E)$ and $B(E)$. (We denote $E_{\vec{p}}$ as E for short if unambiguous.) The Fokker-Planck equation (3.11) then simplifies to

$$\frac{\partial}{\partial t}f_Q(t,\vec{p})=\frac{\partial}{\partial p_i}\left[A(E)p_i f_Q(t,\vec{p})\right]+\frac{\partial^2}{\partial p_i\partial p^i}\left[B(E)f_Q(t,\vec{p})\right]. \tag{3.19}$$

With the physical requirement that the heavy quarks should approach thermal equilibrium with the medium background in the infinite time limit, we may plug in the stable solution $f_Q(\vec{p},t\to\infty)\sim e^{-E/T}$ into Eq.(3.19), where T is the temperature of the medium. With a zero on the left hand side, Eq.(3.19) leads to the following constraints between the drag and the diffusion coefficients:

$$A(E)ET-B(E)+TB'(E)=0, \tag{3.20}$$

where the derivative on $B(E)$ is with respect to E. This is known as the "fluctuation-dissipation relation", or the "Einstein relation". Note that this relation originates from the requirement of the thermal limit, and may not be guaranteed for Eq.(3.12) when the transport coefficients are directly calculated from the matrix elements.

3.1.3 The Langevin Equation: a Stochastic Realization of the Fokker-Planck Equation

In this subsection, we will show the equivalence between the Langevin equation and the Fokker-Planck equation. We will start from the Langevin equation that describes

the Brownian motion of a single particle and demonstrate that it is nothing but a stochastic realization of the Fokker-Planck equation that describes the phase space evolution of a particle ensemble. An alternative method to show the equivalence between these two equations can be found in Ref. [186] where the Fokker-Planck equation is recognized as an Euclidean Schrödinger equation whose Hamiltonian can be constructed using the transition probability from the Langevin equation.

The classical Langevin equation for a single particle reads:

$$\begin{aligned} dx_i &= \frac{p_i}{E_{\vec{p}}} dt, \\ dp_i &= -\Gamma p_i + \sqrt{dt} C_{ik} \rho^k, \end{aligned} \tag{3.21}$$

where in general, the drag coefficient Γ and the strength of the thermal noise C_{ik} are functions of $(t, \vec{x}, \vec{p})$, and $\vec{\rho}$ is the Gaussian-normal distributed random variable signifying the stochastic process:

$$P(\vec{\rho}) = \left(\frac{1}{2\pi}\right)^3 \exp\left(-\frac{\vec{\rho}^2}{2}\right). \tag{3.22}$$

This leads to:

$$\langle \rho_i \rangle_\rho = 0, \qquad \langle \rho_i \rho_j \rangle_\rho = \delta_{ij}, \tag{3.23}$$

where $\langle \cdots \rangle_\rho$ here denotes the stochastic average. One may refer to Appendix B for the related properties of the Gaussian integrals. Thus the thermal random force, which is defined as

$$F_i^{\text{thermal}} = \frac{1}{\sqrt{dt}} C_{ik} \rho^k, \tag{3.24}$$

satisfies the correlation function

$$\begin{aligned} \left\langle F_i^{\text{thermal}}(t) F_j^{\text{thermal}}(t') \right\rangle &= \frac{1}{dt} \left\langle C_{ik} \rho^k C_{jl} \rho^l \right\rangle_\rho = \frac{1}{dt} C_{ik} C_{jl} \delta^{kl} \delta_{tt'} \\ &= C_{ik} C_j^k \delta(t - t') \equiv \kappa_{ij} \delta(t - t'), \end{aligned} \tag{3.25}$$

where $\kappa_{ij} \equiv C_{ik}C_j^k$ is called the momentum space diffusion coefficient of heavy quarks. Note that here we assume a Gaussian white noise for the thermal force, i.e., there exists no correlation between forces at different times.

Up till now, the stochastic process has not been uniquely defined, but depends on how the momentum argument is chosen for C_{ik} [187]. To be more specific, one may define

$$C_{ik} \to C_{ik}(t, \vec{x}, \vec{p} + \xi d\vec{p}), \tag{3.26}$$

and $\xi = 0, 1/2, 1$ correspond to the three different discretization schemes that are usually adopted – pre-point Ito, mid-point Stratonovic-Fisk, and post-point Ito schemes. These different means may lead to different processes, though equivalence can be shown after proper transformation from one to another [118]. This is an essential difference between stochastic differential equations and ordinary differential equations – solutions of the latter do not depend on the discretization scheme when the continuum limit ($dt \to 0$) is taken. To be general, we shall keep the form of Eq.(3.26) for the rest discussion of this subsection.

To derive the Fokker-Planck equation from the Langevin equation, we first discretize Eq.(3.21) with the definition of C_{ik} in Eq.(3.26):

$$x_i(t+\epsilon) = x_i(t) + \epsilon \frac{p_i(t)}{E_{\vec{p}}(t)}, \tag{3.27}$$

$$p_i(t+\epsilon) = p_i(t) - \epsilon\Gamma\left[\vec{p}(t) + \xi d\vec{p}\right] p_i(t) + \sqrt{\epsilon} C_{ik}\left[\vec{p}(t) + \xi d\vec{p}\right] \rho^k. \tag{3.28}$$

We may further substitute $dp_i = -\epsilon\Gamma\left[\vec{p}(t)\right] p_i(t) + \sqrt{\epsilon} C_{ik}\left[\vec{p}(t)\right] \rho^k$ into Eq.(3.28), and keep to the order of ϵ. This yields:

$$\begin{aligned} p_i(t+\epsilon) &= p_i(t) - \epsilon\Gamma\left[\vec{p}(t)\right] p_i(t) + \sqrt{\epsilon} C_{ik}\left[\vec{p}(t)\right] \rho^k + \sqrt{\epsilon}\rho^k \frac{\partial C_{ik}\left[\vec{p}(t)\right]}{\partial p_j} \sqrt{\epsilon}\xi C_{jl}\left[\vec{p}(t)\right] \rho^l \\ &= p_i(t) - \epsilon\Gamma\left[\vec{p}(t)\right] p_i(t) + \sqrt{\epsilon} C_{ik}\left[\vec{p}(t)\right] \rho^k + \epsilon \frac{\partial C_{ik}\left[\vec{p}(t)\right]}{\partial p_j} \xi C_{jl}\left[\vec{p}(t)\right] \rho^k \rho^l. \end{aligned} \tag{3.29}$$

The phase space distribution function of heavy quarks at $(t+\epsilon, \vec{x}, \vec{p})$ can be expressed as an integral over the distribution function at $(t, \vec{x}', \vec{p}')$, with the constraint that the heavy quarks at $(\vec{x}', \vec{p}')$ should propagate to $(\vec{x}, \vec{p})$ within the time interval ϵ. Mathematically, we have

$$f_Q(\vec{x},\vec{p},t+\epsilon) = \int d^3x' d^3p' f_Q(\vec{x}', \vec{p}', t)\delta^{(3)}\left(x_i - x_i' - \epsilon\frac{p_i'}{E_{\vec{p}'}}\right) \times \left\langle \delta^{(3)}\left[p_i - p_i' + \epsilon\Gamma(\vec{p}')p_i' - \sqrt{\epsilon}C_{ik}(\vec{p}')\rho^k - \epsilon\xi C_{jl}(\vec{p}')\frac{\partial C_{ik}(\vec{p}')}{\partial p_j'}\rho^k\rho^l\right]\right\rangle_\rho . \quad (3.30)$$

One may expand the two δ-functions with respect to $\vec{x}$ and $\vec{p}$ respectively and keep to the order of ϵ:

$$\delta^{(3)}\left(x_i - x_i' - \epsilon\frac{p_i'}{E_{\vec{p}'}}\right) = \delta^{(3)}(x_i - x_i') - \epsilon\frac{p_m'}{E_{\vec{p}'}}\frac{\partial}{\partial x_m}\delta^{(3)}(x_i - x_i'), \quad (3.31)$$

$$\begin{aligned}
&\left\langle \delta^{(3)}\left[p_i - p_i' + \epsilon\Gamma(\vec{p}')p_i' - \sqrt{\epsilon}C_{ik}(\vec{p}')\rho^k - \epsilon\xi C_{jl}(\vec{p}')\frac{\partial C_{ik}(\vec{p}')}{\partial p_j'}\rho^k\rho^l\right]\right\rangle_\rho \\
&= \delta^{(3)}(p_i - p_i') + \left\langle \epsilon\Gamma(\vec{p}')p_m'\frac{\partial}{\partial p_m}\delta^{(3)}(p_i - p_i')\right\rangle_\rho - \left\langle \sqrt{\epsilon}C_{mk}(\vec{p}')\rho^k\frac{\partial}{\partial p_m}\delta^{(3)}(p_i - p_i')\right\rangle_\rho \\
&\quad - \left\langle \epsilon\xi C_{jl}(\vec{p}')\frac{\partial C_{mk}(\vec{p}')}{\partial p_j'}\rho^k\rho^l\frac{\partial}{\partial p_m}\delta^{(3)}(p_i - p_i')\right\rangle_\rho \\
&\quad + \frac{1}{2}\left\langle (\sqrt{\epsilon})^2 C_{mk}(\vec{p}')\rho^k C_{nl}(\vec{p}')\rho^l\frac{\partial^2}{\partial p_m\partial p_n}\delta^{(3)}(p_i - p_i')\right\rangle_\rho . \quad (3.32)
\end{aligned}$$

With the identities Eq.(3.23), Eq.(3.32) can be simplified to

$$\begin{aligned}
&\left\langle \delta^{(3)}\left[p_i - p_i' + \epsilon\Gamma(\vec{p}')p_i' - \sqrt{\epsilon}C_{ik}(\vec{p}')\rho^k - \epsilon\xi C_{jl}(\vec{p}')\frac{\partial C_{ik}(\vec{p}')}{\partial p_j'}\rho^k\rho^l\right]\right\rangle_\rho \\
&= \delta^{(3)}(p_i - p_i') + \epsilon\left[\Gamma(\vec{p}')p_m' - \xi C_j^k(\vec{p}')\frac{\partial C_{mk}(\vec{p}')}{\partial p_j'}\right]\frac{\partial}{\partial p_m}\delta^{(3)}(p_i - p_i') \\
&\quad + \frac{1}{2}\epsilon C_{mk}(\vec{p}')C_n^k(\vec{p}')\frac{\partial^2}{\partial p_m\partial p_n}\delta^{(3)}(p_i - p_i'). \quad (3.33)
\end{aligned}$$

By substituting Eq.(3.31) and (3.33) into Eq.(3.30), we obtain

$$f_Q(\vec{x},\vec{p},t+\epsilon) = \int d^3x'd^3p' f_Q(\vec{x}',\vec{p}',t)\left(1-\epsilon\frac{p'_m}{E_{\vec{p}'}}\frac{\partial}{\partial x_m}\right)\delta^{(3)}(x_i-x'_i)\Bigg\{1+\epsilon\Bigg[\Gamma(\vec{p}')p'_m$$
$$-\xi C^k_j(\vec{p}')\frac{\partial C_{mk}(\vec{p}')}{\partial p'_j}\Bigg]\frac{\partial}{\partial p_m}+\frac{1}{2}\epsilon C_{mk}(\vec{p}')C^k_n(\vec{p}')\frac{\partial^2}{\partial p_m\partial p_n}\Bigg\}\delta^{(3)}(p_i-p'_i). \tag{3.34}$$

One may take the derivatives with respect to x_i and p_i out of the integral first and perform integrations over $d^3x'd^3p'$ with the two δ-functions which merely substitute $\vec{x}'$ and $\vec{p}'$ by $\vec{x}$ and $\vec{p}$ respectively. Again, by keeping terms up to the order of ϵ, we have

$$f_Q(\vec{x},\vec{p},t+\epsilon) = f_Q(\vec{x},\vec{p},t)-\epsilon\frac{p_m}{E_{\vec{p}}}\frac{\partial}{\partial x_m}f_Q(\vec{x},\vec{p},t)+\epsilon\frac{\partial}{\partial p_m}\Bigg\{\Bigg[\Gamma(\vec{p})p_m$$
$$-\xi C^k_j(\vec{p})\frac{\partial C_{mk}(\vec{p})}{\partial p_j}\Bigg]f_Q(\vec{x},\vec{p},t)\Bigg\}+\frac{1}{2}\epsilon\frac{\partial^2}{\partial p_m\partial p_n}\left[C_{mk}(\vec{p})C^k_n(\vec{p})f_Q(\vec{x},\vec{p},t)\right], \tag{3.35}$$

which is equivalent to

$$\left(\frac{\partial}{\partial t}+\frac{p_m}{E_{\vec{p}}}\frac{\partial}{\partial x_m}\right)f_Q(\vec{x},\vec{p},t) = \frac{\partial}{\partial p_m}\Bigg\{\left[\Gamma(\vec{p})p_m-\xi C^k_j(\vec{p})\frac{\partial C_{mk}(\vec{p})}{\partial p_j}\right]f_Q(\vec{x},\vec{p},t)$$
$$+\frac{1}{2}\frac{\partial}{\partial p_n}\left[C_{mk}(\vec{p})C^k_n(\vec{p})f_Q(\vec{x},\vec{p},t)\right]\Bigg\}. \tag{3.36}$$

If one sets

$$\begin{aligned} A_m(\vec{p}) &= \Gamma(\vec{p})p_m-\xi C^k_j(\vec{p})\frac{\partial C_{mk}(\vec{p})}{\partial p_j}, \\ B_{mn}(\vec{p}) &= \frac{1}{2}C_{mk}(\vec{p})C^k_n(\vec{p}), \end{aligned} \tag{3.37}$$

we obtain the previous Fokker-Planck equation (3.11) except that the position ($\vec{x}$) space is also included here. Furthermore, by combining Eq.(3.15) and Eq.(3.37), we have

$$\Gamma(\vec{p}) = A(\vec{p})+\frac{1}{p_i}\xi C^k_j(\vec{p})\frac{\partial C_{ik}(\vec{p})}{\partial p_j}, \tag{3.38}$$

$$C_{ik}(\vec{p}) = \sqrt{2B_0}P^{\parallel}_{ik}+\sqrt{2B_1}P^{\perp}_{ik}. \tag{3.39}$$

As discussed in the previous subsection, one may assume $B_0(\vec{p}) = B_1(\vec{p}) = B(\vec{p})$, which simplifies Eq.(3.39) to

$$C_{ik}(\vec{p}) = \sqrt{2B(\vec{p})}\delta_{ik}. \tag{3.40}$$

Thus, we have the momentum space diffusion coefficient

$$\kappa_{ij}(\vec{p}) = C_{ik}(\vec{p})C^k_j(\vec{p}) = 2B(\vec{p})\delta_{ij} \equiv \kappa(\vec{p})\delta_{ij}, \tag{3.41}$$

with the definition $\kappa(\vec{p}) \equiv 2B(\vec{p})$. Moreover, by substituting Eq.(3.40) and (3.41) back into Eq.(3.38), we have

$$\begin{aligned}\Gamma(\vec{p}) &= A(\vec{p}) + \frac{1}{p_i}\xi\sqrt{\kappa(E)}\frac{\partial\sqrt{\kappa(E)}}{\partial E}\frac{\partial E}{\partial p_j}\delta^k_j\delta_{ik} \\ &= A(\vec{p}) + \frac{1}{2}\xi\frac{1}{E}\frac{\partial\kappa(E)}{\partial E}.\end{aligned} \tag{3.42}$$

In the end, we combine Eq.(3.20) and Eq.(3.42) and obtain the fluctuation-dissipation relation for the Langevin equation (3.21):

$$2\Gamma(E)ET - \kappa(E) + (1-\xi)T\kappa'(E) = 0. \tag{3.43}$$

For the case of $\xi = 1$, i.e., the post-point Ito scheme, or κ independent of E, we have a simplified form of the Einstein relation $\Gamma = \kappa/2TE$, which will be utilized in our Langevin framework for the rest of this dissertation.

3.1.4 Langevin Evolution of Heavy Quark inside a QGP Medium

Due to their large mass, the momentum change of heavy quarks during each of their scatterings with thermal partons is considered to be small. Therefore, in the limit of multiple interactions where the Gaussian distribution of the thermal noise Eq.(3.22) can be reasonably applied, the heavy quark motion inside a QGP can be treated as a Brownian motion and be described by the Langevin equation (3.21). In this work,

we start with a "minimal model" where the momentum space diffusion coefficient κ_{ij} is assumed isotropic – the same in the longitudinal and the transverse directions – and independent of the momentum of the heavy quark. Thus, according to the analysis in the previous subsection, Eq.(3.21) is reduced to

$$\begin{aligned} dx_i &= \frac{p_i}{E_{\vec{p}}}dt, \\ dp_i &= -\Gamma(\vec{p})p_i + \sqrt{dt}\sqrt{\kappa}\rho_i, \end{aligned} \tag{3.44}$$

in which the drag term and the thermal term are related by the fluctuation-dissipation theorem $\Gamma = \kappa/2TE$. In the literature, the spatial diffusion coefficient D is usually quoted for heavy quark calculations, which is related to κ via

$$D = \frac{T}{M\Gamma(0)} = \frac{2T^2}{\kappa}. \tag{3.45}$$

More discussion about this diffusion coefficient can be found in Appendix C. This will be the main parameter in our Langevin framework for the rest of our study. For the numerical calculation, we adopt the pre-point Ito discretization and re-write the Langevin equation as

$$x_i(t+\Delta t) = x_i(t) + \frac{p_i(t)}{E_{\vec{p}}(t)}\Delta t, \tag{3.46}$$

$$p_i(t+\Delta t) = p_i(t) - \Gamma\left[\vec{p}(t)\right] p_i(t)\Delta t + F_i^{\text{thermal}}(t)\Delta t, \tag{3.47}$$

where the thermal force satisfies

$$\left\langle F_i^{\text{thermal}}(t) F_j^{\text{thermal}}(t+n\Delta t)\right\rangle_\rho = \frac{\kappa}{\Delta t}\delta_{ij}\delta_{0n}, \tag{3.48}$$

and can be generated using the Monte-Carlo method with a Gaussian distribution whose width is $\sqrt{\kappa/\Delta t}$.

For the study of heavy quark motion in a static medium, the only information required for the medium is the temperature, which remains fixed throughout the time

evolution of the heavy quarks. On the other hand, to study the heavy quark transport inside the highly excited medium produced in heavy-ion collisions, we need to simulate the QGP matter with hydrodynamic models. Either a fully (3+1)-dimensional ideal relativistic hydrodynamic model developed in Ref .[21] or a (2+1)-dimensional viscous relativistic hydrodynamic model developed in Ref. [22, 188, 24] can be embedded into our Langevin framework. In our work, two different initial condition models, a Glauber [13, 15] as well as a KLN-CGC [16] model, are utilized to describe the initial entropy density distribution of the medium before its hydrodynamical evolution. Both initial conditions are tuned to provide the hadronic data in the soft sector, such as hadron yields, spectra, and rapidity-distributions as well as radial and elliptic flow. These hydrodynamic models provide us with the time evolution of the spatial distribution of the temperature and the flow velocity of the QGP medium. In such a dynamic medium, heavy quark evolution is treated as follows: for every Langevin time step we boost each heavy quark to the local rest frame of the fluid cell in which it is located; the Langevin approach Eq.(3.47) is then applied to obtain the momentum change of the heavy quark due to the surrounding QGP medium. After that we boost the heavy quark back to the global computation frame where it propagates to the space-time point for the next scattering according to Eq.(3.46).

One of the key assumptions for the hydrodynamic calculation is that the QCD medium experiences a sudden thermalization (to form a QGP) at an initial time τ_0 (chosen as 0.6 fm/c here) at which the hydrodynamical evolution commences. And up till now, little knowledge has been attained regarding the pre-equilibrium evolution and thermalization of the system. On the heavy quark side, we treat their motion prior to the QGP formation as free-streaming. Such treatment should be a good approximation as the time of the pre-equilibrium stage is short compared to the total life time of the QGP (about 10 fm/c).

3.2 Thermalization of Charm Quarks in the QGP Medium

In this section, we use our Langevin framework constructed above to conduct an investigation into heavy quark thermalization in an infinite medium at fixed temperature and then compare our findings to a dynamic scenario in which the heavy quarks propagate through an expanding and cooling QGP medium, modeled with a (3+1)-dimensional ideal relativistic hydrodynamic approach [21]. The purpose of this study is to answer the question whether general features seen in the data, such as the presence of elliptic flow and a small value of the nuclear modification factor of heavy flavor observables, can be used to conclude that heavy quarks actually have thermalized in the QGP medium created in ultra-relativistic heavy-ion collisions, or whether the heavy quarks remain off-equilibrium during their entire evolution, despite exhibiting a strong response to the surrounding QGP. The contents presented in this section has been originally published in Ref. [184].

3.2.1 Thermalization Criterion

Before exploring the thermalization process of heavy quarks, one needs to define the thermalization criterion. Our criterion is based on the heavy quark energy and momentum spectra.

In a medium at fixed temperature without any inherent collective flow, one may apply the canonical ensemble to thermalized heavy quarks:

$$f(\vec{p})dp_x dp_y dp_z = \frac{V}{\mathcal{Z}} e^{-\beta E} dp_x dp_y dp_z, \tag{3.49}$$

where V is the volume in position space and $\mathcal{Z}$ is the partition function. Alternatively, we may write

$$\frac{dN}{d^3p} \propto e^{-E/T}. \tag{3.50}$$

Note that $d^3p = p^2 dp d\Omega = pEdEd\Omega$, we have

$$\frac{dN}{pEdE} = Ce^{-E/T}. \tag{3.51}$$

This allows for a straightforward extraction of the "temperature" of the heavy quark ensemble via an exponential fit. While this particular form for the energy distribution provides a convenient representation for the extraction of the temperature parameter, later we will show that it is insufficient to actually indicate thermalization, since we still need to verify isotropy of particle momenta.

To obtain the momentum spectrum in a specific direction (take $\hat{z}$ as an example), we start from Eq.(3.49) again and integrate over p_x and p_y. This yields

$$\begin{aligned} f(p_z) &= \frac{V}{\mathcal{Z}} \int dp_x dp_y e^{-\beta\sqrt{p_x^2+p_y^2+p_z^2+m^2}} \\ &= \frac{V}{\mathcal{Z}} \int_0^{2\pi} d\theta \int_0^{\infty} p_T dp_T e^{-\beta\sqrt{p_T^2+p_z^2+m^2}} \\ &= CT(\sqrt{p_z^2+m^2}+T)e^{-\sqrt{p_z^2+m^2}/T}. \end{aligned} \tag{3.52}$$

Note that if we initialize our heavy quark ensemble with a finite momentum along a given coordinate axis, its momentum distribution along that axis will be blue-shifted – this can be taken into account by shifting the distribution along that axis using a parameter $\tilde{p}_i$; e.g. for the z axis this would give [1]:

$$f(p_z) = CT(\sqrt{(p_z-\tilde{p}_z)^2+m^2}+T)e^{-\sqrt{(p_z-\tilde{p}_z)^2+m^2}/T}. \tag{3.53}$$

For an expanding and cooling QGP medium, establishing thermalization requires the following procedure: for a given time step we select all cells in our hydrodynamic

[1] Rigorously, p_z should be boosted via $\gamma p_z + \gamma\beta E$. However, it is found that in our study, for β not too large (below 0.8), the much more convenient Eq.(3.53) already fits the spectrum well (with an error less than 5% for T).

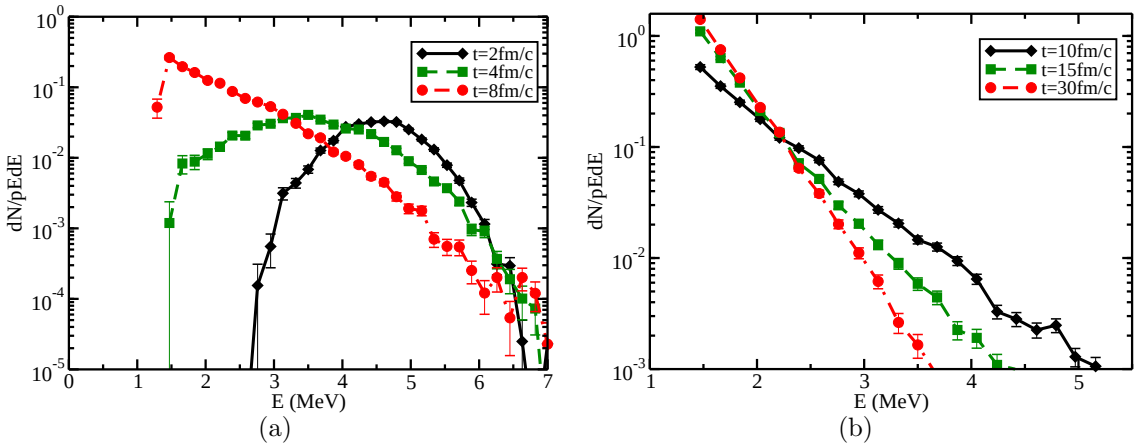

FIGURE 3.1: The time evolution of the energy spectrum. (a) shows the results between 2 fm/c and 8 fm/c, where no linear relation is observed; and (b) shows the results between 10 fm/c and 30 fm/c, where the linear relation is apparent.

medium within a temperature band of $T \pm \Delta T$. We then boost all charm quarks localized in those cells into the respective local rest frames of the cells they are residing in and calculate the resulting heavy quark energy and momentum distributions. If both the energy [Eq.(3.51)] and the momentum [Eq.(3.53)] distributions of the heavy quark ensemble yield thermal distributions with a temperature that lies within our selected temperature band, we can conclude that the selected heavy quark ensemble has thermalized in the medium at the given temperature and selected time step. This procedure can then be repeated for other temperature bands and time steps.

3.2.2 Equilibration in a Static Medium

We start our investigation by simulating the diffusion of charm quarks in an infinite medium with a static temperature of 300 MeV. The initial momentum of the charm quarks is chosen to be 5 GeV in the $\hat{z}$ direction and the diffusion coefficient is set as $D = 6/(2\pi T)$ which will be shown later to provide the best agreement to data on the elliptic flow and the nuclear modification factor of heavy mesons observed at RHIC and LHC.

Figure 3.1 shows the energy spectrum $dN/pEdE$ vs. E for different diffusion

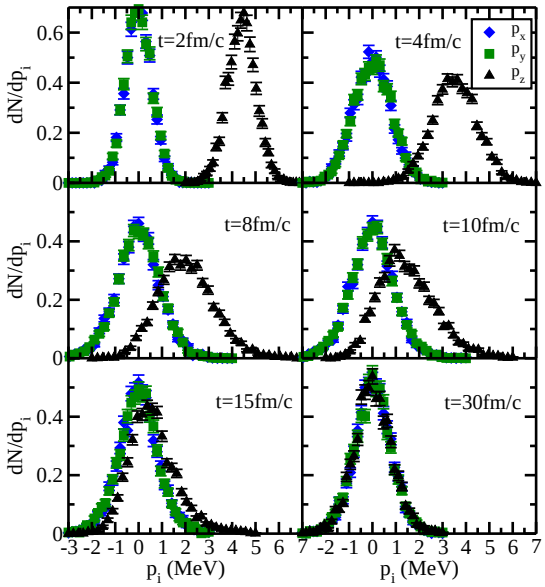

FIGURE 3.2: The time evolution of the momentum spectrum.

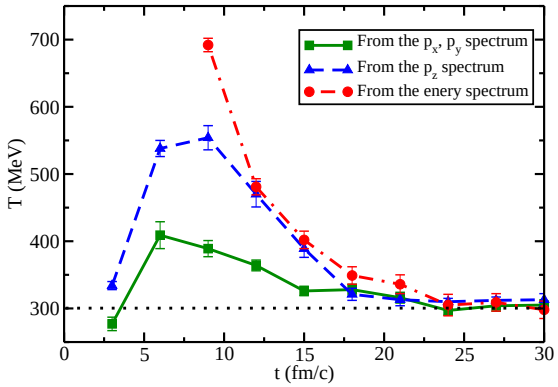

FIGURE 3.3: A comparison of "temperatures" obtained from p_x, p_y, p_z and the energy spectra. Since $\hat{x}$ and $\hat{y}$ directions are symmetric, we take the mean value of the "temperatures" fitted from p_x and p_y spectra here.

times. We see that a linear relation between $\ln(dN/pEdE)$ and E does not occur for diffusion times shorter than approx. 10 fm/c. The distribution appears thermal for longer diffusion times. However, the slope continues to increase as a function of diffusion time and does not converge to the temperature of the medium until a diffusion time of around 30 fm/c. Therefore, despite the shape of the energy distribution, our ensemble of charm quarks is not fully equilibrated for diffusion times between 10 fm/c and 30 fm/c.

Figure 3.2 shows the momentum distributions in the three directions for the same diffusion times as displayed in Fig.3.1. Since the initial momentum of the charm quarks is in the $\hat{z}$ direction, the p_x and p_y spectra are symmetric with respect to 0 and are virtually identical to each other. To the contrary, the center of the p_z spectrum, which initially is a δ-function at $p_z = 5$ GeV due to our initial condition, shifts towards 0 as a function of increasing diffusion time, signifying the influence of the drag term of the Langevin equation on the dominant direction of propagation. The widths of the momentum distributions along all three coordinate axes start to

agree with each other for diffusion times later than 25 fm/c, hinting at a common "temperature". At that time, full isotropy of the momenta is obtained.

We can obtain the "temperature" evolution of the charm quark ensemble by fitting the momentum distributions with Eq.(3.53), and compare the respective values of the temperature parameter with those obtained from the slope of the energy distribution. The results are shown in Fig.3.3 as a function of diffusion time, which helps to summarize our main observations from the previous figures as follows:

- for diffusion times less than 10 fm/c, the p_z spectrum is distinctly separated from the p_x and p_y spectra. The temperature parameters extracted from the widths of the distributions initially rise and are significantly above the actual temperature of the medium. They are of different values for the transverse momentum distributions vs. the longitudinal momentum distribution (as defined by the z axis). No temperature can be obtained from the energy distribution since no linear relation is observed at those short diffusion times.

- for diffusion times between 10 fm/c and 20 fm/c, all momentum distributions as well as the energy distribution exhibit a thermal shape, even though the extracted temperature parameters strongly differ among each other and from the temperature of the medium. Interestingly, the temperature parameter extracted from the longitudinal momentum distribution seems to track that from the energy distribution during this time interval. However, both are significantly higher than the temperature parameter extracted from the transverse momentum distributions.

- at a diffusion time of roughly 25 fm/c, all temperature parameters agree well with each other and have converged to the temperature of the medium, signaling full equilibration of our charm quark ensemble.

Based on our observations, we define a "quasi-equilibrium" stage to be a near equilibrium state where the linear relation of the $\ln(dN/pEdE)$ vs. E distribution appears and the temperature parameters extracted from energy and p_z spectra are of approximately the same value. During this stage, our ensemble of charm quarks exhibits thermal properties, even though it has not yet fully equilibrated with the surrounding medium. In contrast, a "full equilibrium" is obtained when the temperature parameters extracted from different ways agree with each other and reach the temperature of the medium.

To further understand the nature of the quasi-equilibrium state and why the "temperature" of the charm quarks is still higher than that of the medium in this stage of the evolution, despite the linear relation between $\ln(dN/pEdE)$ and E, we may have to take into account a "blue shift" caused by the center of mass motion of the charm quarks: for our analysis, all charm quarks were initialized to carry a momentum of 5 GeV in the $\hat{z}$ direction. This initial momentum can be seen as a center of mass motion – it contributes to the total energy of the particle, but is non-thermal in origin. As the charm quark diffuses through the medium, this initial kinetic energy will dissipate through the drag term of the Langevin equation. During this dissipation dominated phase of the charm quark evolution, the center of mass motion will contribute to an additional part of energy and therefore a higher "temperature". In this sense, the quasi-equilibrium state can be understood as a stage when the thermal part of heavy quark motion is already close to equilibrium but the center of mass motion has not entirely dissipated.

This blue shift can be verified by fitting Eq.(3.53) with a momentum distribution that includes a momentum shift $\tilde{p}_z$. We will see that the blue shift is suppressed if the initial momentum of the heavy quarks is small enough that it becomes comparable to its thermal motion. This in fact helps prove that the blue shift is the reason for a higher heavy quark "temperature" in the quasi-equilibrium state.

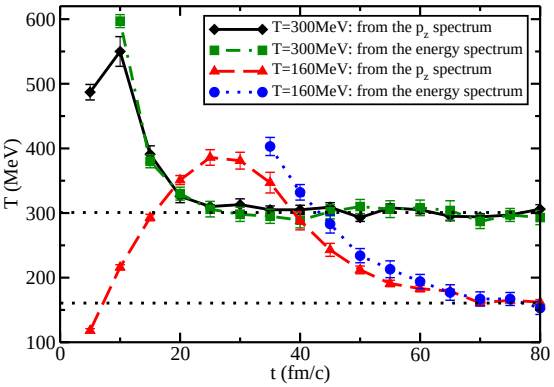

FIGURE 3.4: A comparison of the charm quark thermalization processes with different medium temperatures.

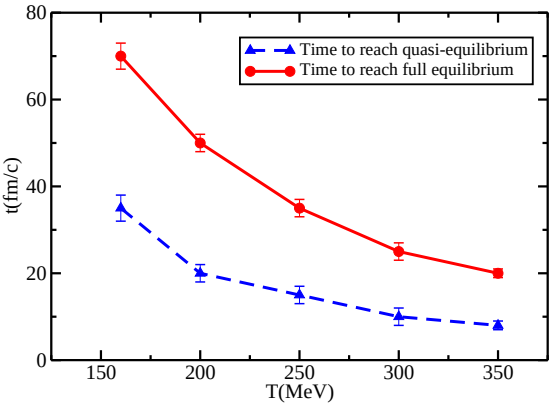

FIGURE 3.5: The variation of critical times of thermalization with respect to the medium temperature.

With the above definitions of thermalization process of heavy quarks, we may explore how such process depends on the properties of the medium as well as heavy quarks themselves. As above, we initialize charm quarks with 5 GeV momentum along the $\hat{z}$ direction. The spatial diffusion coefficient is set to be $D = 6/(2\pi T)$. Here, we vary the temperature of the static medium and examine its corresponding influence on the thermalization process. The results are shown in Fig.3.4 and Fig.3.5.

In Fig.3.4, we compare the thermalization of charm quarks in a 300 MeV temperature medium to that in a medium at 160 MeV. For charm quarks with an initial momentum of 5 GeV, their "temperature" extracted from the dN/dp_z distribution increases first, and then decreases until it approaches the medium temperature at which time the full equilibrium is reached. It is observed that the turning point between the rise and fall of the "temperature" is close to the onset of the quasi-equilibrium stage. A similar trend can be observed via the $dN/dp_{x,y}$ distribution (not shown here), but the range of variation in the extracted "temperature" is not as large as that from the dN/dp_z distribution. The above observation can also be obtained from media with other temperatures indicated in Fig.3.5 (not shown here).

We can understand the "turning point" behavior as follows. Since the charm

quarks are all sampled with 5 GeV initial momentum in the $\hat{z}$ direction here, they are initially at zero temperature with respect to their center of mass frame. During the diffusion process, the momenta of the charm quarks are randomized and thus their "temperature" increases. When the random motion approaches equilibrium, i.e., the entrance of the quasi-equilibrium state, the charm quarks' "temperature" might be higher than the medium temperature if the initial center of mass momentum of the ensemble has not entirely been dissipated. After that, this temperature parameter gradually decreases towards the medium temperature with the dissipation of the center of mass momentum. Such a rise in the temperature parameter before reaching the quasi-equilibrium results from this particular initialization of charm quarks, and will not occur for more realistic scenarios where charm quarks are initialized in more realistic ways.[2]

As the temperature of the medium decreases, both the time needed to reach quasi-equilibrium and the time to obtain full equilibrium increase. The time to enter the quasi-equilibrium stage can vary from 8 fm/c (for 350 MeV medium) to 35 fm/c (for 160 MeV medium), and the time to approach the full equilibrium can vary from 20 fm/c (for 350 MeV medium) to 70 fm/c (for 160 MeV medium). This variation is clearly shown in Fig.3.5.

In Fig.3.6 we investigate how the thermalization speed is affected by the initial momentum of charm quarks. We utilize a static medium with 160 MeV temperature and show our analysis for charm quarks with initial momenta of 1 GeV and 3 GeV in the $\hat{z}$ direction (results for an randomized initialization in the x-y plane can be found in our original work [184]).

We observe that the results of 3 GeV initial momentum are similar to those

[2] The temperature parameter before quasi-equilibrium is approached provides some insight into the dynamics of thermalization, namely the interplay of momentum broadening vs. energy dissipation through collisional energy loss. However, the values of the "temperature" obtained in this domain are not indicative of thermal behavior but just a measure of the broadening of the charm quark momentum distribution, since Eq.(3.53) is only strictly valid near equilibrium.

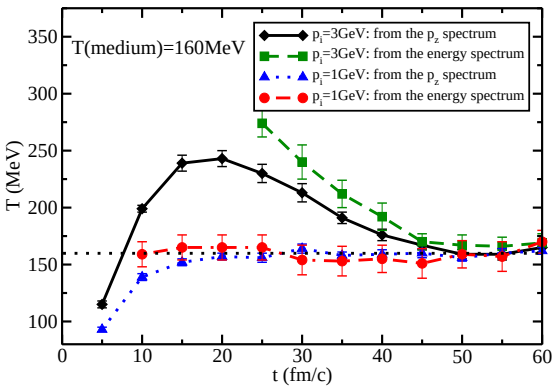

FIGURE 3.6: A comparison of the thermalization processes of charm quarks with different initial momenta.

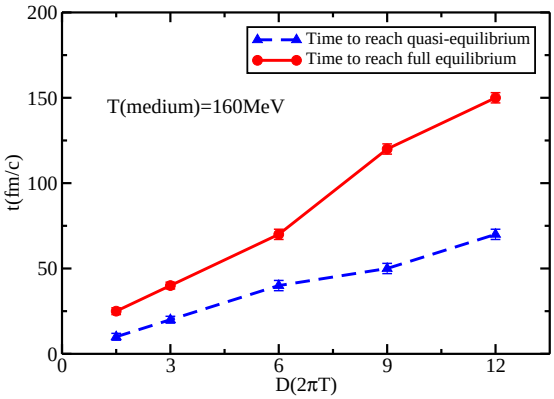

FIGURE 3.7: The variation of critical times of thermalization with respect to the diffusion coefficient of the medium.

of the 5 GeV case shown in Fig.3.4: the "temperature" obtained from the dN/dp_z distribution first increases and then decreases until the full equilibrium is approached, and the turning point corresponds to the entrance of the quasi-equilibrium stage. However, the results of the 1 GeV initial momentum case are different. There is no overshoot in the "temperature" for this case. Instead, the "temperature" obtained from the dN/dp_z distribution keeps increasing gradually towards the temperature of the medium until the full equilibrium is reached. In other words, unlike in the higher initial momentum cases, the "temperature" of the charm quarks with 1 GeV initial momentum is always below that of the medium until reaching full equilibrium. We attribute this difference to the suppression of the blue shift for the center of mass motion of the charm quarks, which is too small in this case to contribute significantly to the energy of the charm quark.

For the low initial momentum situation, the onset of the quasi-equilibrium stage can no longer be determined via the "turning" point, but only by the appearance of the linear relation in the $\ln(dN/pEdE)$ vs. E distribution. In our simulation, for heavy quarks with 1 GeV initial momentum, this linear relation does not appear until 10 fm/c for the 160 MeV medium.

Additionally, a comparison between Fig.3.4 and Fig.3.6 suggests that with a decrease of the magnitude of the initial momentum, the thermalization occurs faster. For instance, the times needed for 5 GeV charm quarks to reach quasi-equilibrium and full equilibrium are 35 fm/c and 70 fm/c respectively, while the respective times for 1 GeV charm quarks are 10 fm/c and 20 fm/c. This decrease can also be understood with the concept of the blue shift: it takes less time for a smaller initial momentum to dissipate.

In Fig.3.7, we examine the influence of the diffusion coefficient on the process of heavy quark thermalization. We set the medium temperature to 300 MeV, initialize charm quarks with a momentum of 5 GeV in the $\hat{z}$ direction, and vary the diffusion coefficient to investigate its effect on the thermalization time. The results indicate that as the diffusion coefficient decreases, i.e., the drag coefficient increases, the thermalization process speeds up. The times needed to enter the quasi-equilibrium state and the full equilibrium state can be respectively reduced from 70fm/c and 150fm/c for $D = 12/(2\pi T)$ to 10 fm/c and 25 fm/c for $D = 1.5/(2\pi T)$.

3.2.3 Charm Quark Thermalization in a QGP Medium

After a detailed investigation of the heavy quark thermalization process inside a static medium, we extend our study to a realistic expanding QGP medium. The QGP medium is generated by a (3+1)-dimensional ideal hydrodynamic calculation with MC-Glauber initial conditions that have been adjusted to reproduce bulk properties of the QCD medium created in central Au+Au collisions at RHIC [21]. The initial distribution of charm quarks here is generated by the VNI/BMS parton cascade model [189, 190]. The parameters chosen for both the hydrodynamical evolution and the heavy quark initialization here are consistent with the experimental setup of $\sqrt{s} = 200$ GeV Au-Au collisions with an impact parameter of 2.4 fm. Although at about 8 fm/c the medium temperature drops below T_c (160 MeV), we extend our

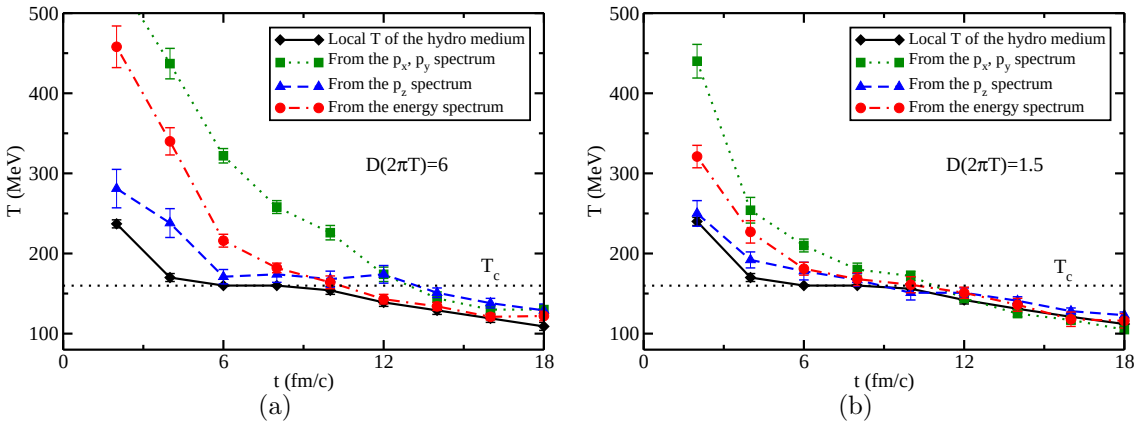

FIGURE 3.8: Thermalization of charm quarks in a realistic QGP medium. (a) shows the results with a diffusion coefficient of $D = 6/(2\pi T)$; and (b) shows the results with a diffusion coefficient of $D = 1.5/(2\pi T)$.

study of charm quarks to the time of kinetic freeze-out (around 20 fm/c), assuming that D mesons interact with the medium in a similar way as the charm quarks do with the QGP. Details about the heavy flavor hadronization and the subsequent hadronic interactions will be discussed later in this dissertation.

We show our results in Fig.3.8. As shown in Fig.3.8(a), using a diffusion coefficient of $D = 6/(2\pi T)$, the "temperature" of the charm quarks never manages to catch up with that of the medium until freeze-out. A closer observation indicates that the charm quarks remain far off equilibrium during the entire lifetime of the QGP phase, i.e., when the medium temperature is above T_c. However, Fig.3.8(b) suggests that if the diffusion coefficient is reduced to $D = 1.5/(2\pi T)$, the thermalization process accelerates significantly and the "temperature" of the charm quarks is able to catch up with that of the medium during its QGP phase, i.e., above T_c. This result does not imply a small value as $D = 1.5/(2\pi T)$ for the diffusion coefficient, but only indicates that with a currently favored value of $D = 6/(2\pi T)$, which describes experimental results well, charm quarks remain off-equilibrium during their entire evolution although they exhibit a strong response to the surrounding QGP.

To summarize for this section, we have studied the dynamics of heavy quark

thermalization in the framework of the Langevin equation. Simulations have been carried out in both static and dynamic QGP media, and our methodology allows for the extraction of the "temperature" of the heavy quarks by fitting either the heavy quark energy or its momentum spectrum. Using an idealized static medium, it is found that charm quark thermalization occurs in two distinct steps: first a quasi-equilibrium is obtained in which the charm quark energy distribution matches that of a thermal medium, but the momentum distribution remains non-isotropic; subsequently the charm quark momenta isotropize and the charm quarks are in full equilibrium with the surrounding medium. The occurrence of this two step process might be explained by a blue shift effect due to the center of mass motion of the heavy quarks. We define full equilibrium to imply that the "temperature" extracted from both methods, fitting the energy and the momentum distributions, matches that of the medium. Our simulations in the static medium indicate that as the medium temperature decreases, it takes a longer time for the charm quarks to thermalize. Additionally, the thermalization time is extremely sensitive to the diffusion coefficient of the medium: as the diffusion coefficient decreases, or the drag coefficient increases, the thermalization process can be significantly accelerated. A decrease in the magnitude of the initial momentum leads to a suppression of the blue shift effect and therefore results in a faster thermalization process, due to the initial charm quark momenta being closer to the thermal momentum scale of the system. For a realistic expanding QGP medium, we find that for a reasonable choice of the diffusion coefficient, quasi-elastic scatterings between heavy quarks and thermal partons do not infer the thermalization of heavy quarks within the QGP lifetime. Therefore, the manifestation of collective behavior, such as a significant elliptic flow, or the presence of a strongly interacting system (via the nuclear modification factor) is insufficient to conclude that charm quarks have actually thermalized in the medium even though their properties are strongly affected by the surrounding medium.

3.3 Model and Parameter Dependence of Heavy Quark Energy Loss

In this section, using the Langevin framework developed in Sec.3.1, we investigate how heavy quark spectra in relativistic heavy-ion collisions are affected by various parameters of the calculation of heavy quark energy loss, such as the initial production of heavy quarks, the geometry and the flow properties of the hydrodynamic medium, and the coupling strength between heavy quarks and medium. This will provide us with important quantitative understanding of the interaction dynamics of heavy quarks in a hot and dense medium before we move on to make a direct comparison between our calculations and experimental data. The contents presented in this section has been originally published in Ref. [185].

3.3.1 Calculation Setup and Final State Observables

As discussed in the previous subsection, we continue to utilize the fully (3+1)-dimensional ideal relativistic hydrodynamic model [21] to describe the spacetime evolution of the QGP medium. Two different initial condition models, the Glauber and the KLN-CGC model, are utilized to describe the initial energy distribution of the medium before the hydrodynamical evolution commences. These two initial state models provide energy/entropy density profiles with different spatial anisotropies in the transverse plane, a larger eccentricity for the KLN-CGC model than the Glauber model. The comparison between the two will allow for a study of the sensitivity of heavy-quark observables to the initial spatial make-up of the system. We will focus on mid-central Au-Au collisions at RHIC with a center-of-mass energy $\sqrt{s_{\rm NN}}$=200 GeV per nucleon pair and use an impact parameter of $b = 6.5$ fm throughout the calculation.

Since the production of heavy quarks is dominated by processes with large transverse momentum transfer, perturbative QCD is applied to calculate the initial mo-

mentum distribution of heavy quarks prior to their propagation through the QGP medium. We fit a leading-order perturbative QCD calculation with a power-law distribution [118], and sample the initial transverse momentum of heavy quarks according to the following parametrization:

$$\frac{dN}{d^2p_{\mathrm{T}}} \propto \frac{1}{(p_{\mathrm{T}}^2 + \Lambda^2)^{\alpha}}, \tag{3.54}$$

where $\alpha = 3.9$ and $\Lambda = 2.1$ are taken for charm quarks, and $\alpha = 4.9$ and $\Lambda = 7.5$ for bottom quarks. In this work, we focus on the energy loss of heavy quarks at mid-rapidity and therefore assign no initial longitudinal momentum to heavy quarks. We have verified that the introduction of initial longitudinal momenta that are uniform around the mid-rapidity region ($-1 < y < 1$) does not affect our final transverse momentum spectra and does not affect the systematics we are about to explore. The relative normalization (ratio) of charm and bottom quarks is not fixed, but rather serves as a free parameter in our simulation. Later we will investigate the effect of this normalization on the quenching and the elliptic flow of heavy flavor decay electrons.

The initial spatial distribution of heavy quarks in the transverse plane is sampled according to the distribution of binary collisions as calculated from a Monte-Carlo Glauber model. With a given spatial and momentum initialization of heavy quarks, we are able to simulate their time evolution inside the QGP in the framework of Langevin equation as described in Sec.3.1.4. After passing through the medium, their fragmentation into heavy flavor mesons and the subsequent decay into electrons are simulated via PYTHIA 6.4 [137]. By default, the fragmentation process is calculated with the Lund symmetric fragmentation function that is modified by the Bowler spacetime picture of string evolution [191] for heavy quarks. The hadronic and the subsequent semi-leptonic processes are combined for the decay of charm/bottom hadrons in which all possible channels are taken into account. Details regarding the

implementation can be found in the PYTHIA manual above and will be summarized in Sec.5.1. Note that apart from fragmentation, the other hadronization mechanism – heavy-light quark coalescence – is also important but has not been included in this particular analysis. A unified hadronization framework of the fragmentation plus coalescence model for heavy quarks will be developed later in Chapter 5.

After freeze-out, the final state particles in the mid-rapidity region ($-1 < y < 1$) are selected and their momentum distributions are utilized to calculate the nuclear modification factor $R_{\rm AA}$ and the elliptic flow coefficient v_2 as follows:

$$R_{\rm AA}(p_{\rm T}) \equiv \frac{1}{N_{\rm coll}} \frac{dN^{\rm AA}/dp_{\rm T}}{dN^{\rm pp}/dp_{\rm T}}, \tag{3.55}$$

$$v_2(p_{\rm T}) \equiv \langle \cos(2\phi) \rangle = \left\langle \frac{p_x^2 - p_y^2}{p_x^2 + p_y^2} \right\rangle. \tag{3.56}$$

Note that when heavy quarks are directly analyzed, the denominator and the numerator of $R_{\rm AA}$ are the initial heavy quark distribution and the final state distribution of suffering energy loss and passing through the medium. When analyzing heavy flavor mesons or electrons, the denominator represents the spectra of the corresponding particles fragmented/decayed directly from the initial heavy quarks, while the numerator represents those produced from the heavy quarks after propagating through the QGP medium. $\langle \cdots \rangle$ in Eq.(3.56) represents the average over all analyzed particles in a selected $p_{\rm T}$ bin.

3.3.2 Charm Quark Energy Loss and Flow

The energy loss of heavy quarks and the development of the elliptic flow crucially depend on the geometrical shape and the dynamical evolution of the thermalized QGP medium that the heavy quarks traverse. The total energy loss of heavy quarks is mostly controlled by the overall magnitude of the energy density of the medium, while the elliptic flow is more sensitive to the geometry of the medium as it characterizes

the anisotropy of the final transverse momentum spectra. In typical non-central nucleus-nucleus collisions, the overlap region of the two nuclei is anisotropic in the transverse plane, thus resulting in an anisotropy of the produced hot and dense medium. Due to the different pressure gradients in different directions, anisotropic flow is built up during the hydrodynamical evolution of the thermalized QGP.

In such an anisotropic dynamical medium, there exist two factors affecting the anisotropy of heavy quark energy loss: the different path lengths through the medium and the different flow profiles experienced by the heavy quarks traveling in different directions. Longer paths will be traversed by heavy quarks moving in the out-of-plane (y) direction than in the in-plane (x) direction, where the reaction plane is defined to be spanned by the impact parameter and the beam axis directions. Thus in absence of collective flow from the medium, heavy quarks, after passing through such an anisotropic medium, would have larger momentum in the x direction than in the y direction, $\langle p_x^2 \rangle > \langle p_y^2 \rangle$, resulting in a positive elliptic flow. In addition, the collective flow of the medium also contributes positively to heavy quark elliptic flow since the push of the radial flow is more prominent in the x direction. Therefore, the total elliptic flow developed during the propagation of heavy quarks in such an anisotropic hydrodynamic medium is due to a combination of these two factors.

We can separate these two effects in the simulation by switching on or off the coupling of the collective flow of the thermalized medium to the evolving heavy quarks. The decoupling from the collective flow can be accomplished by not boosting the heavy quarks into the respective rest frame of the fluid cell for the Langevin evolution. The comparison between the heavy quark evolution with and without coupling to the collective flow is shown in Fig.3.9, where the left plot shows the nuclear modification factor $R_{\rm AA}$ and the right plot shows the elliptic flow v_2 of the charm quarks as a function of the transverse momentum. We show results for two different values of diffusion coefficient $D = 1.5/(2\pi T)$ and $D = 6/(2\pi T)$.

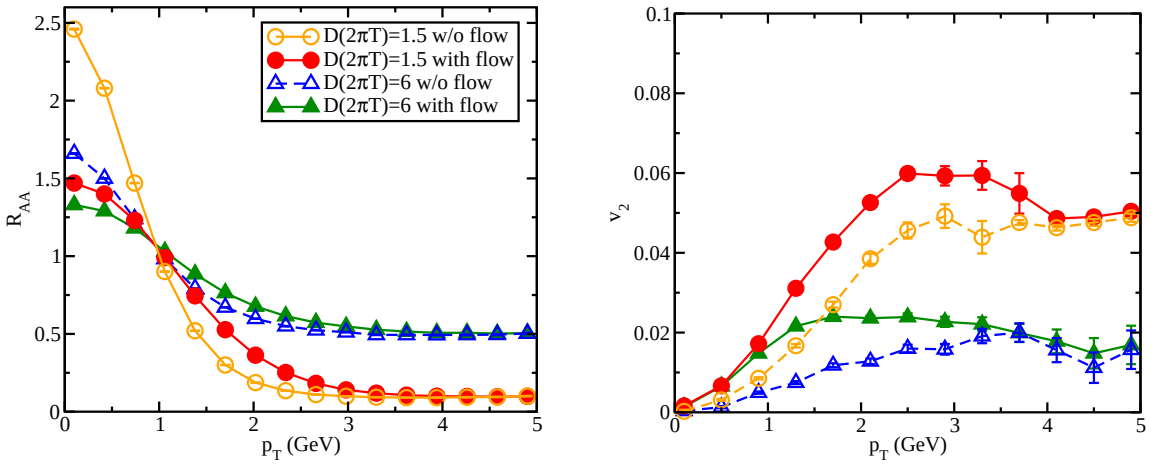

FIGURE 3.9: A comparison between the influence of QGP media with and without collective flow on $R_{\rm AA}$ (left panel) and v_2 (right panel) of charm quarks. Both media are generated with the Glauber initial condition.

The effect of the collective flow of the medium on the heavy quark energy loss can be clearly seen from the plot of the nuclear modification factor $R_{\rm AA}$ in Fig.3.9. It is negligible at high $p_{\rm T}$, and becomes observable at intermediate $p_{\rm T}$ regime. Due to the push by the radial flow, heavy quarks are less suppressed, i.e. have a larger $R_{\rm AA}$, at larger transverse momenta, since the radial flow effectively transports low momentum heavy quarks to larger transverse momenta. Similar effects stemming from the elliptic flow of the medium are observed for the heavy quark elliptic flow coefficient v_2. At low $p_{\rm T}$, the collective flow of the medium presents a significant influence on the charm quark v_2. At high $p_{\rm T}$, the collective flow effect is small, thus the development of charm v_2 is dominated by the geometric anisotropy of the medium. The dominance of the medium collective flow at low $p_{\rm T}$ for v_2 might indicate that low $p_{\rm T}$ charm quarks are more likely to lose a significant amount of their momenta and therefore thermalize in the medium, and thus flow more like the thermalized medium.

A closer observation suggests that with a decrease of the diffusion coefficient, i.e., an increase of the coupling strength, the influence of the geometric asymmetry becomes more dominant. For instance, Fig.3.9 reveals that for $D = 6/(2\pi T)$, the geo-

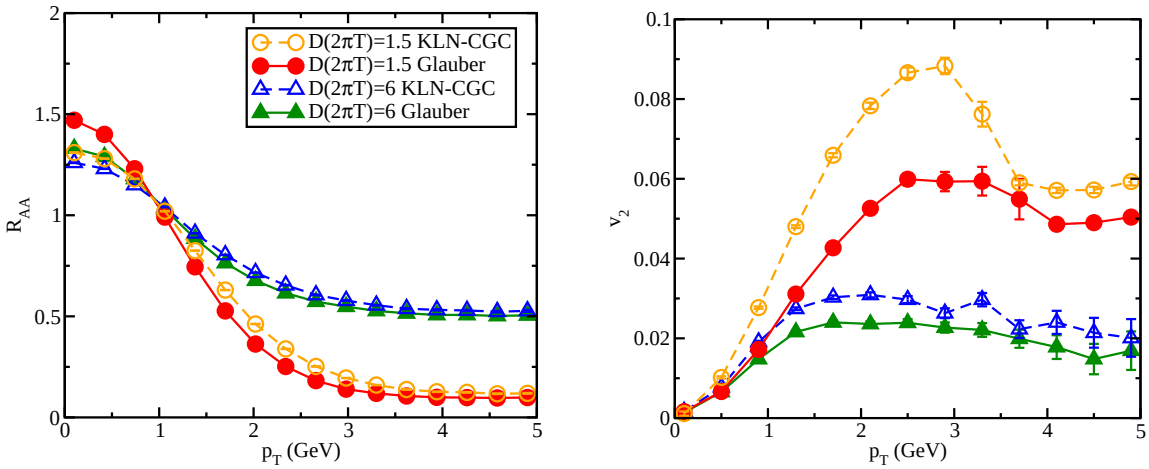

FIGURE 3.10: Effects of different QGP profiles (Glauber vs. KLN-CGC initial conditions) on the charm quark $R_{\rm AA}$ (left panel) and v_2 (right panel).

metric asymmetry of the medium contributes to only approximately half of the charm quark v_2 at the peak value (around $p_{\rm T} = 1.5$ GeV). However, for $D = 1.5/(2\pi T)$, such contribution increases to more than 80% at the corresponding peak value (around $p_{\rm T} = 3$ GeV). Note that such increase of the geometric contribution is not unlimited. With further reduction of the diffusion coefficient ($D < 1.5/(2\pi T)$), i.e., a larger coupling between heavy quarks and the medium, the energy loss of charm quarks will be so intense that all of them will be captured by the medium. In that limit, charm quarks thermalize with the medium during the QGP lifetime (see Sec.3.2), and therefore, their v_2 will entirely follow the collective flow of the medium. In our simulation, the choice of $D \sim 1.5/(2\pi T)$ provides the largest elliptic flow for the final heavy quarks.

We may further investigate the effect of the spatial medium distribution on the heavy quark energy loss and the development of heavy quark elliptic flow by utilizing different initial conditions for the hydrodynamic simulation of the QGP. Two different initial condition models are widely used for the initialization of the energy density distribution prior to the hydrodynamic evolution: the Glauber model and the KLN-CGC model. These two models provide initial energy density profiles with different

anisotropies in the transverse plane. In particular, the KLN-CGC model exhibits a larger eccentricity $\epsilon_2 = \langle y^2 - x^2 \rangle / \langle y^2 + x^2 \rangle$ than the Glauber model, which will manifest itself in larger elliptic flow coefficients for the heavy quarks.

The comparison between these two initial condition models is shown in Fig.3.10, where the left frame of the figure shows the nuclear modification factor $R_{\rm AA}$ and right shows the elliptic flow v_2. As expected, a significantly larger elliptic flow is observed for the charm quarks traveling through the hydrodynamic medium with the KLN-CGC initial condition than those with the Glauber initial condition. As indicated by Fig.3.10, the difference can be as large as 20% for $D = 6/(2\pi T)$ and 40% for $D = 1.5/(2\pi T)$. We also observe that while v_2 is sensitive to the choice of the initial condition, the nuclear modification factor $R_{\rm AA}$ is not significantly affected by the choice of these two initial conditions. This is due to $R_{\rm AA}$ being controlled by the overall normalization of the density profile in the hydrodynamical evolution which has been tuned to describe the properties of bulk matter, such as the π and K spectra.

3.3.3 D Mesons and Heavy Decay Electrons

In the above discussion, we have focused on the effects of initial conditions and medium parameters on heavy quark energy loss and the development of heavy quark elliptic flow. Now we investigate the corresponding sensitivities of heavy flavor mesons and their decay electrons. Since the KLN-CGC initial condition provides a larger eccentricity for the initial energy density profile and thus produces a larger elliptic flow of heavy quarks during their medium evolution, we use it for the remainder of our analysis. This is merely to obtain the largest possible values of the final elliptic flow, since most of the previous calculations seem to under-predict the elliptic flow data of non-photonic electrons once the model parameters have been tuned to describe the measured nuclear modification factor.

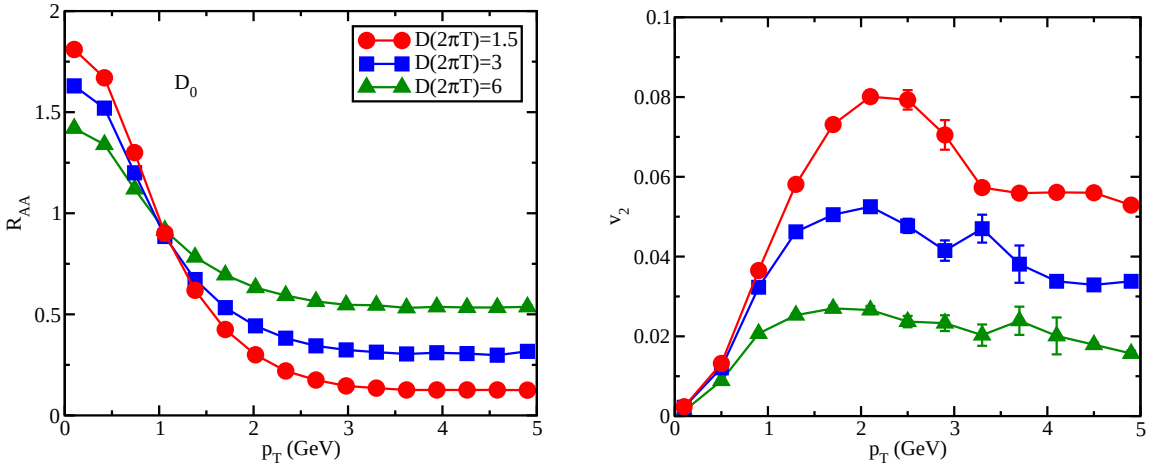

FIGURE 3.11: $R_{\rm AA}$ (left panel) and v_2 (right panel) of D_0 mesons. The QGP medium is generated with the KLN-CGC initial condition.

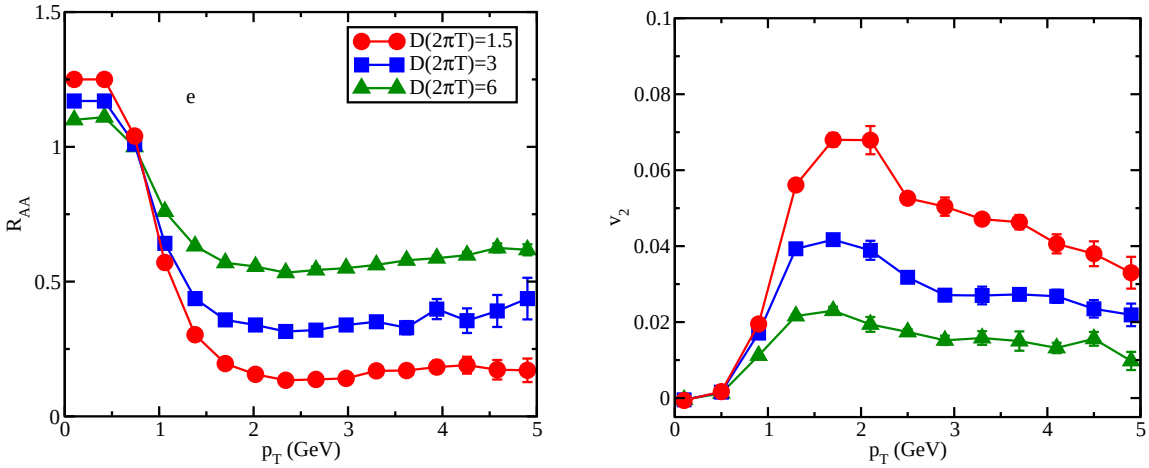

FIGURE 3.12: $R_{\rm AA}$ (left panel) and v_2 (right panel) of electrons decayed from charm quarks. The QGP medium is generated with the KLN-CGC initial condition.

Figures 3.11 and 3.12 display the numerical results of the nuclear modification factor $R_{\rm AA}$ and the elliptic flow v_2 for D mesons and D-decay electrons. Three different values of diffusion coefficients are used for comparison $D = 1.5/(2\pi T)$, $D = 3/(2\pi T)$, and $D = 6/(2\pi T)$. We observe that the transverse momentum dependence of $R_{\rm AA}$ and v_2 are similar to that for charm quarks as shown in the previous figures.

For the heavy flavor decay electron spectra, another important factor is the relative contributions from charm vs. bottom quarks. Since charm and bottom quarks

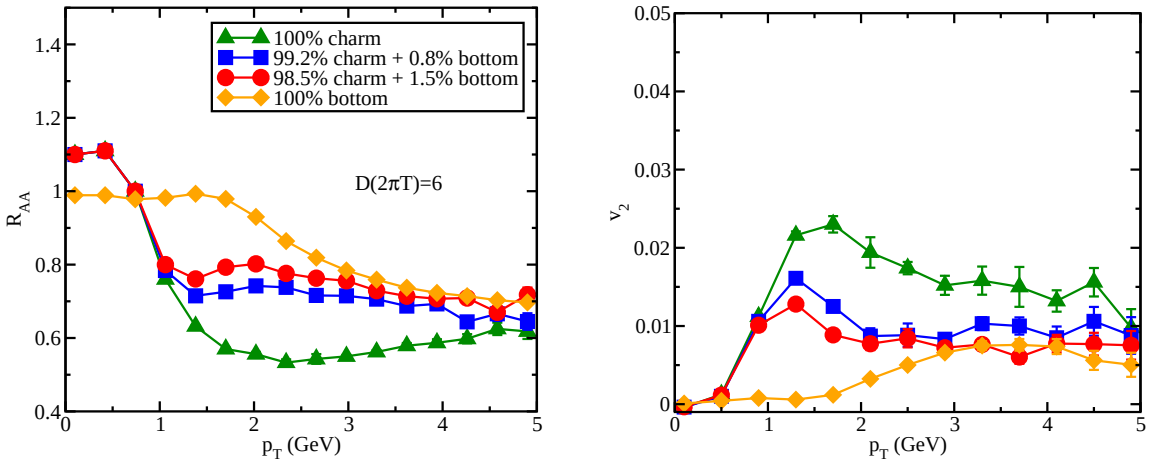

FIGURE 3.13: A comparison of $R_{\rm AA}$ (left panel) and v_2 (right panel) of non-photonic electrons between different initial charm/bottom ratios. Set $D = 6/(2\pi T)$ and the QGP medium is generated with the KLN-CGC initial condition.

have different masses, they are produced with different initial transverse momentum distributions, and experience different energy loss and coupling to the collective flow in medium. This manifests itself in different $R_{\rm AA}$ and v_2 systematics for D and B mesons respectively and subsequently translates into different behavior for their respective decay electrons. The electrons at lower $p_{\rm T}$ are dominated by the charm quark decay, while in the high $p_{\rm T}$ regime the bottom quark dominates as the source of these electrons. Since there are multiple uncertainties affecting the relative normalization of the charm and the bottom quark production, for example the scale dependence in pQCD calculation of initial heavy quark production [192], we treat the ratio of charm and bottom quarks as a free parameter for our calculation, and investigate how the variation of this ratio affects the final non-photonic electron distributions.

The results are shown in Fig.3.13 and Fig.3.14 for two different values of diffusion coefficients, $D = 1.5/(2\pi T)$ and $D = 6/(2\pi T)$, respectively. We compare four different initializations here – pure charm, pure bottom, and two mixtures of charm and bottom quarks: 99.2% charm quarks with 0.8% bottom quarks, and 98.5% charm

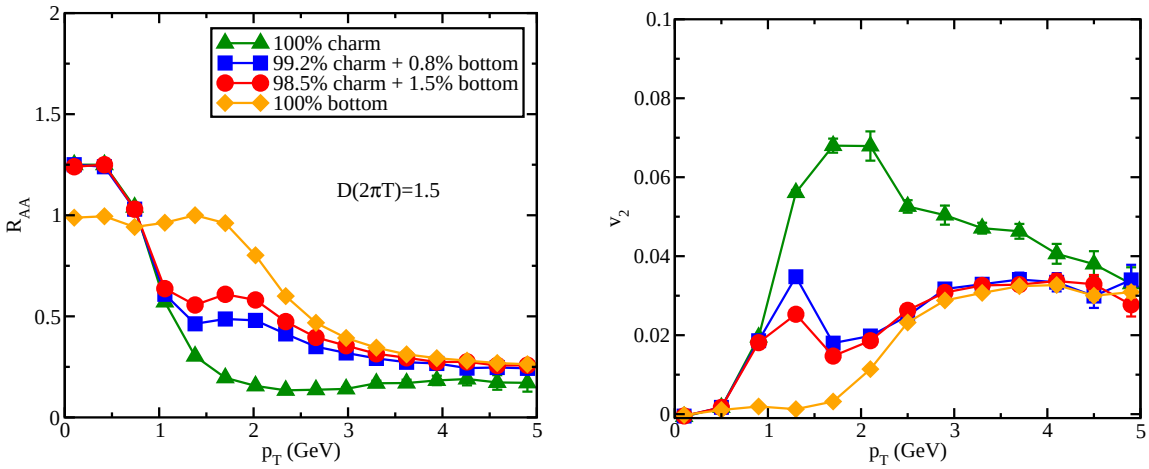

FIGURE 3.14: A comparison of $R_{\rm AA}$ (left panel) and v_2 (right panel) of non-photonic electrons between different initial charm/bottom ratios. Set $D = 1.5/(2\pi T)$ and the QGP medium is generated with the KLN-CGC initial condition.

quarks with 1.5% bottom quarks. As shown in [192], the bottom quark contribution to the electron spectra may start dominating over the charm quark contribution at transverse momentum as low as 3 GeV or as high as 9 GeV. Our two hybrid mixtures of charm and bottom quarks have about a factor of 2 difference in their ratio, representing an estimate of the uncertainties due to our limited control of the proton-proton baseline.

One observes from these two figures that the nuclear modification factor $R_{\rm AA}$ and the elliptic flow v_2 of heavy flavor decay electrons are very different for the pure charm vs. pure bottom scenario. Bottom quarks are less suppressed than charm quarks at high transverse momenta, thus less enhancement is observed at low transverse momenta in the $R_{\rm AA}$. The magnitude of the elliptic flow coefficient v_2 is much smaller for electrons from the bottom decay than from the charm decay, again due to the reduced energy loss experienced by the bottom quarks. In addition, we observe a difference in the transverse momentum dependence: while the elliptic flow coefficient v_2 of electrons from charm decays has a peak value at intermediate transverse momentum, that for bottom decays increases monotonically with increasing

transverse momentum (below 5 GeV). This results from charm quarks contributing mostly to the production of low transverse momentum electrons while bottom quarks contributing mostly to high transverse momentum electrons because of their different masses.

Due to the different behavior of charm vs. bottom decay electrons, the electrons from a mixture of charm and bottom decays exhibit a very rich structure. Both R_{AA} and v_2 trend similar to the pure charm initialization at low transverse momenta and converge to the values of the pure bottom quark scenario at high transverse momenta. In the intermediate p_{T} region where the transition from charm dominance to bottom dominance in the origin of the decay electrons takes place, a non-monotonic transverse momentum dependence of R_{AA} and v_2 is observed: a dip-peak structure for R_{AA} and a peak-dip structure for v_2. Such a non-monotonic behavior is more prominent for the smaller value of the diffusion coefficient $D = 1.5/(2\pi T)$ (Fig.3.14), since a smaller value of the diffusion coefficient increases the interaction with the medium and thus the energy loss of charm quarks and their elliptic flow, while such an enhancement is far less for bottom quarks due to their larger mass. Current experimental results seem not able to resolve whether such a peak-dip structure is present or not in the non-photonic electron elliptic flow v_2 due to large experimental error bars. Further improvement of the measurement of the detailed p_{T} dependence of non-photonic electrons would be helpful for the determination of the diffusion coefficient and therefore the coupling strength between heavy quarks and the QGP.

Another important effect seen in Fig.3.13 and Fig.3.14 is the significant sensitivity of heavy flavor decay electron v_2 to the initial charm-to-bottom quark ratio. For instance, a 0.7% difference in the mixing ratio between charm and bottom quarks in our simulation leads to a variation of approximately 25% in v_2 for a diffusion coefficient of $D = 6/(2\pi T)$ and over 30% for $D = 1.5/(2\pi T)$. As has been discussed earlier, significant uncertainties regarding the initial heavy quark spectra are still

present in our current phenomenological calculations, and thus provide a sizable uncertainty for the prediction of the quenching and the elliptic flow of non-photonic electrons.

To summarize this section, we have studied the model and parameter dependence of heavy quark energy loss within the Langevin approach developed in Sec.3.1.4. Numerical results are presented for both the nuclear modification factor and the elliptic flow of heavy quarks, heavy flavor mesons and their corresponding non-photonic decay electrons. We have investigated in detail how the $R_{\rm AA}$ and v_2 are affected by various components of the model, such as the geometry and the collective flow of the hydrodynamic medium, the initial production ratio of charm to bottom quarks and the coupling strength between the heavy quarks and the medium.

We have focused on two particular properties of the medium that affect the heavy quark energy loss – its geometric anisotropy and its collective flow. It is found that the geometric anisotropy dominates the final heavy quark distributions in the high $p_{\rm T}$ region, while the collective flow of the medium dominates the low $p_{\rm T}$ region. The impact of the initial QGP geometry on the heavy quark energy loss has been explored by comparing the Glauber and the KLN-CGC initialization of the hydrodynamic medium. We found that while a similar nuclear modification factor $R_{\rm AA}$ is observed for both initial condition models, a significantly higher heavy quark elliptic flow v_2 is found for the KLN-CGC model. We have further investigated the sensitivity of the spectra and the elliptic flow of non-photonic electrons to the relative contributions from charm and bottom quarks. It is found that a less than 1% difference in the initial charm-to-bottom ratio can lead to more than 30% variation of the non-photonic electron spectra. Therefore, narrowing down these uncertainties is essential for a better understanding of the interaction dynamics between heavy quarks and the QGP.

4

Medium-induced Gluon Radiation of Heavy Quarks inside the QGP

In the study of parton evolution and energy loss in a dense QCD matter, two important mechanisms are usually considered: quasi-elastic scattering with medium partons and medium-induced gluon radiation [69, 67]. In the previous chapter, we constructed a Langevin framework for the former mechanism. This should be sufficient for the description of heavy quark motion at low transverse momentum regime because the phase space for the latter process – gluon radiation – is restricted by their large mass. This is known as the "dead cone effect" [120]. However, as we extend our investigation to higher p_{T} regions, heavy quarks become as ultra-relativistic as light partons, and therefore it is no longer reasonable to neglect radiative energy loss. In this chapter, we will modify the classical Langevin equation so that it can also incorporate the medium-induced gluon radiation of heavy quarks by treating gluon emission as a recoil force term.

We will first demonstrate how gluon radiation is introduced into the classical Langevin framework in Sec.4.1. Subsequently, within this new framework, we will

compare the contribution from collisional and radiative energy loss to the in-medium evolution of heavy quark in Sec.4.2, and show that while quasi-elastic scattering dominates heavy quark motion at low momenta, gluon radiation dominates at high momenta. In Sec.4.3, we apply our modified Langevin approach to an investigation of how the energy loss of heavy quarks is affected by initial state fluctuations in heavy-ion collisions. The contents of Sec.4.1 and Sec.4.2 have been originally published in Ref. [134, 107] and Sec.4.3 has been published in Ref. [193].

4.1 The Modified Langevin Equation

As illustrated in the previous chapter, in the limit of small momentum transfer, the multiple scattering of heavy quarks off thermal partons inside a QGP medium can be treated as Brownian motion and thus is typically described using the Langevin equation. However, in addition to the collisional energy loss resulting from such quasi-elastic scatterings, heavy quarks may also lose energy through medium-induced gluon radiation. To incorporate both collisional and radiative energy loss experienced by heavy quarks propagating through the dense QGP, we modify the classical Langevin equation Eq.(3.44) as follows:

$$\begin{aligned} dx_i &= \frac{p_i}{E_{\vec{p}}}dt, \\ dp_i &= -\Gamma(\vec{p})p_i + \sqrt{dt}\sqrt{\kappa}\rho_i + F_i^{\text{gluon}}dt, \end{aligned} \tag{4.1}$$

The first two terms on the right-hand side of the second line are the drag force and the thermal random force from the original Langevin equation, and the third term $\vec{F}_{\text{gluon}} = -d\vec{p}_{\text{gluon}}/dt$ is introduced to describe the recoil force exerted on heavy quarks due to gluon radiation, where $\vec{p}_{\text{gluon}}$ denotes the momentum of radiated gluons.

Similar to Eq.(3.46) and Eq.(3.47), we discretize this modified Langevin equation

as follows:

$$x_i(t+\Delta t) = x_i(t) + \frac{p_i(t)}{E_{\vec{p}}(t)}\Delta t, \tag{4.2}$$

$$p_i(t+\Delta t) = p_i(t) - \Gamma\left[\vec{p}(t)\right] p_i(t)\Delta t + F_i^{\text{thermal}}(t)\Delta t - \Delta p_i^{\text{gluon}}(t), \tag{4.3}$$

in which the thermal force satisfies the following correlation function

$$\left\langle F_i^{\text{thermal}}(t) F_j^{\text{thermal}}(t+n\Delta t)\right\rangle_\rho = \frac{\kappa}{\Delta t}\delta_{ij}\delta_{0n} \tag{4.4}$$

as before and thus each spatial component of F_i^{thermal} during a Δt can still be independently sampled with a Gaussian distribution whose width is $\sqrt{\kappa/\Delta t}$ in our numerical simulations.

In Eq.(4.3), $\Delta\vec{p}_{\text{gluon}}$ is the momentum of gluons radiated during the time interval Δt. We determine the probability of this gluon radiation during each inteval Δt according to the average number of gluons in this time interval:

$$P_{\text{rad}}(t,\Delta t) = \langle N_{\text{gluon}}(t,\Delta t)\rangle = \Delta t \int dx dk_\perp^2 \frac{dN_{\text{gluon}}}{dx dk_\perp^2 dt}. \tag{4.5}$$

We choose sufficiently small time steps Δt to ensure that the average radiated gluon number is smaller than 1 in Δt. In this work, we utilize the results of the higher-twist calculation for the medium-induced gluon spectra [84, 135, 122]:

$$\frac{dN_{\text{gluon}}}{dx dk_\perp^2 dt} = \frac{2\alpha_s P(x)\hat{q}}{\pi k_\perp^4}\sin^2\left(\frac{t-t_i}{2\tau_f}\right)\left(\frac{k_\perp^2}{k_\perp^2 + x^2M^2}\right)^4, \tag{4.6}$$

where $k_\perp$ is the transverse momentum of the radiated gluon, and x is the fractional energy carried by radiated gluons from the heavy quark. In addition, α_s is the strong coupling constant, $P(x)$ is the splitting function of the gluon and $\hat{q}$ is the gluon transport coefficient. The gluon formation time τ_f is defined as $\tau_f = 2Ex(1-x)/(k_\perp^2 + x^2M^2)$, with E and M being the energy and mass of the

heavy quark. Note that the quartic term at the end of Eq.(4.6) characterizes the "dead-cone" effect, i.e., the suppression of gluon radiation due to the finite mass of heavy quarks. In this work, we shall use a leading-order running coupling constant α_s, and the related details can be found in Appendix A.

At a given time step, Eq.(4.5) is used to determine the probability of radiating a gluon. If a gluon is formed, its energy and momentum will be generated using a Monte-Carlo method according to the gluon radiation spectrum in Eq.(4.6). After a gluon is emitted from the heavy quark, the initial time t_i in the equation is reset to zero so that the probability of radiating the next gluon starts to accumulate again with time. Note that the framework we describe here does not necessarily require the higher-twist formalism – other energy loss formalisms can be used as well, as long as they provide the distributions for both energy and transverse momentum of the radiated gluons.

For the classical Langevin equation without the contribution from gluon radiation, we have the fluctuation-dissipation relation $\Gamma = \kappa/2TE$. We assume this still holds for the thermal drag term and the noise term in our modified Langevin equation. However, the detailed balance between gluon radiation and absorption has not been rigorously included into our current framework due to the lack of the latter process. To mimic this balance in the simulation of radiative energy loss, we impose a lower cutoff $\omega_0 = \pi T$ for the gluon energy. Below such a cutoff, the gluon emission is disabled and the evolution of heavy quarks with low energies is completely controlled by quasi-elastic multiple scattering for which the detailed balance is well defined. Such a treatment for medium-induced gluon radiation ensures that heavy quarks achieve thermal equilibrium after sufficiently long evolution times. Meanwhile, we use $\hat{q} = 2\kappa C_A/C_F$ to relate the gluon transport coefficient (signifying the momentum broadening of gluon in the transverse direction) and the momentum space diffusion coefficient of heavy quark, where $C_F = N_c = 3$ and $C_A = (N_c^2 - 1)/(2N_c) = 4/3$

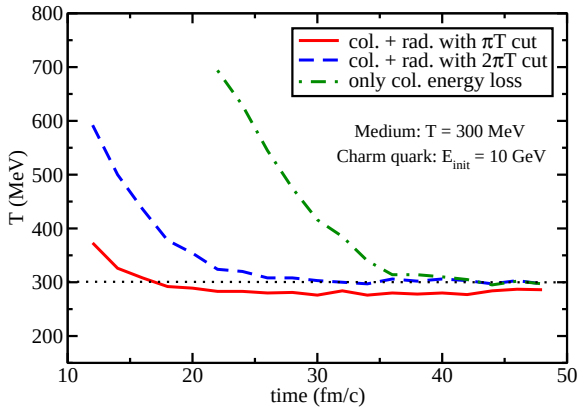

FIGURE 4.1: Thermalization process of charm quarks in a static medium, compared between different lower cutoffs of gluon energy.

are the color factors for quarks and gluons. With such a setup, we only have one free parameter in the Langevin framework as described above. To be consistent with the previous chapter and other literature as well, we convert both $\hat{q}$ and κ into the spatial diffusion coefficient of heavy quark defined in Eq.(3.45) and set $D = 6/(2\pi T)$ throughout the calculations in this chapter, which corresponds to a gluon transport coefficient $\hat{q}$ around 3 GeV^2/fm at a temperature of $T = 400$ MeV.

In Fig. 4.1 we provide a numerical check of the thermalization process of charm quarks according to the modified Langevin equation. The charm quarks are all initialized with an energy of 10 GeV and then evolve inside an infinite and static medium with a constant temperature of 300 MeV. The temperature parameter of the charm quark ensemble is extracted from their energy spectrum utilizing the method as described in Sec.3.2. As is shown, if there is only collisional energy loss, the temperature parameter of the charm quarks evolves to the medium temperature as expected. We also examine such thermalization behavior when the gluon radiation is introduced. If the energy cutoff for the gluon radiation is large enough, e.g., $2\pi T$ in the plot, the heavy quarks will eventually equilibrate with the medium temperature. For the choice of πT, an equilibrium can still be achieved, with the only difference that

the equilibrium temperature is shifted by a small amount, approximately 20 MeV below the medium temperature.

In this work, the lower cutoff for radiative gluon energy is taken to be πT, which is the typical energy of the gluons in the thermalized QGP medium. Such choice introduces 5-10% uncertainty in the equilibrium temperature, but should not substantially influence the description of heavy flavor observables presented later. Additionally, if one considers all sources of experimental and theoretical uncertainties, such as those in hydrodynamic initial conditions and the nuclear shadowing effect, it might not be necessary to artificially increase the energy cut for gluon radiation merely for the exact preservation of the detailed balance. A more rigorous treatment would incorporate the absorption process as well in the above simulation of gluon radiation. Such an effort has already been explored in the context of light parton radiative energy loss [194] and will be pursued in a future study.

With the modified Langevin framework described above, we may now couple it to a hydrodynamic medium to simulate the heavy quark evolution inside hot and dense QCD matter created in relativistic heavy-ion collisions as described in Sec.3.1.4. Starting with this chapter, the space-time evolution profiles of the QGP fireballs at LHC and RHIC will be generated with a (2+1)-dimensional viscous hydrodynamic model, which was developed by Song et al [22, 188] and has recently been modified by Qiu and Shen for increased numerical stability [24]. We employ the code version and parameter tunings that were previously used in Ref. [24]. In the following calculation, a MC-Glauber model is adopted to generate the positions of participant nucleons and binary collisions, providing both the initial conditions of hydrodynamics and the spatial distribution of initial heavy quarks if not otherwise specified. As described in Chapter 2, a leading-order perturbative QCD calculation will be adopted for the momentum space initialization of heavy quarks, in which the nuclear shadowing effect in nucleus-nucleus collision is taken into account by using the EPS08 parametrization

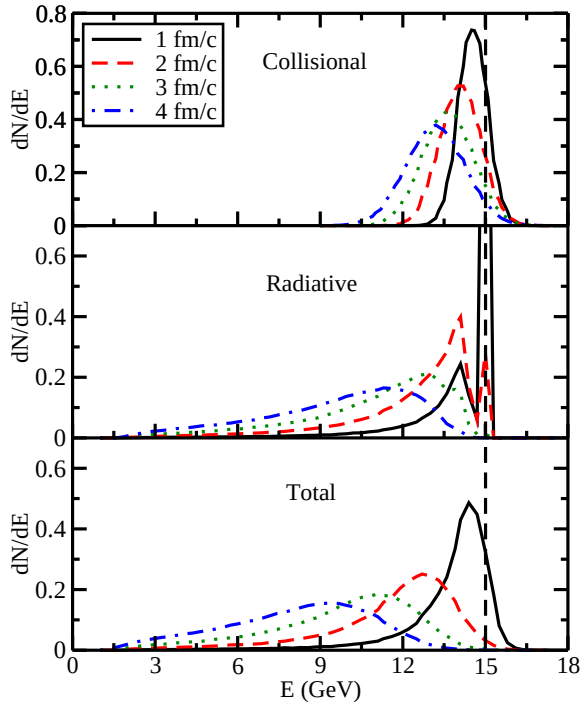

FIGURE 4.2: A comparison of the evolution of the charm quark energy distribution in a static medium between collisional, radiative and total energy loss.

[175] of the parton distribution function. As mentioned in Sec.3.1.4, the evolution of heavy quarks in the pre-equilibrium state before the onset of the hydrodynamical evolution ($\tau_0 = 0.6$ fm/c) is treated as free-streaming. Additionally, in this chapter heavy quarks are also assumed to stream freely after they leave the QGP, i.e., when the local temperature of the medium drops below T_c (165 MeV for the hydrodynamic model used here). The subsequent hadronization process and the interaction between heavy mesons and the hadron gas will be discussed in later chapters.

4.2 Collisional vs. Radiative Energy Loss

Before moving on to utilize our updated Langevin framework to explore heavy flavor observables, we first compare the contribution from each energy loss mechanism to heavy quark evolution in this section.

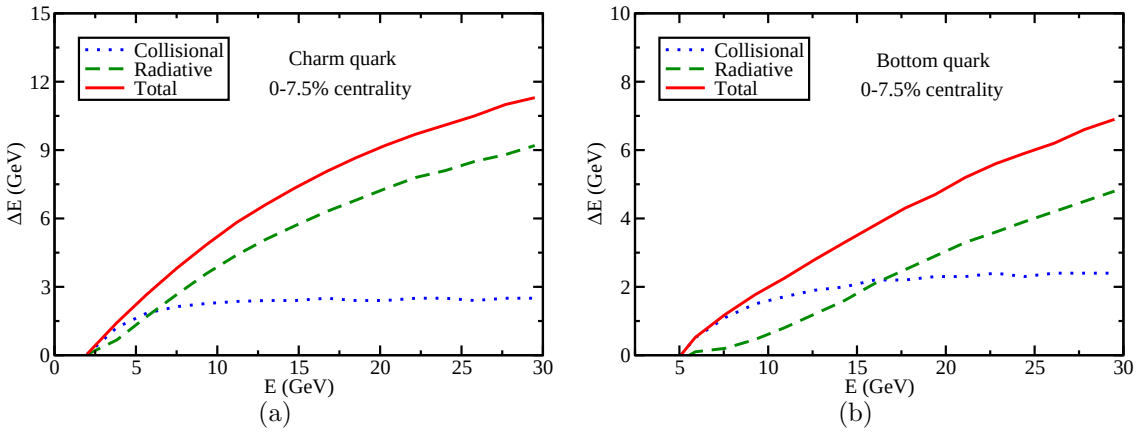

FIGURE 4.3: Comparison of radiative and collisional energy losses for charm (a) and for bottom (b) quarks.

As shown in Fig.4.2, we start with the evolution of the charm quark energy distribution due to the different energy loss mechanisms. Here, the charm quarks are all initialized with 15 GeV energy before traveling through an infinite medium with a fixed temperature of 300 MeV. From Fig.4.2, we observe that the energy distributions start from a δ-function at 15 GeV and then evolve with respect to time. Before 2 fm/c, collisional energy loss dominates the charm quark evolution. However, after 2 fm/c, gluon radiation starts to dominate. Moreover, the collisional energy loss leads to a Gaussian smearing of the energy distribution, which should be a natural result of multiple soft scatterings according to the "central limit theorem". To the contrary, gluon radiation generates a "long tail structure" of the energy distribution.

In Fig.4.3, we compare the total energy loss of heavy quarks after they traverse a realistic QGP medium produced in 0-7.5% centrality Pb-Pb collisions at 2.76 TeV. The x-axis represents the initial energy of heavy quarks and y represents the total energy loss. As is shown, quasi-elastic scatterings dominate the heavy quark energy loss in the low energy regime, while medium-induced gluon radiation dominates at high energies. The crossing points are around 6 GeV for charm quarks and 16 GeV for bottom quarks. These results indicate that collisional energy loss alone may

provide good descriptions for the heavy flavor measurements at low p_{T} but will become insufficient when we extend to a higher p_{T} regime, such as that measured by the LHC experiments. Similar competition between the collisional and the radiative energy loss will be observed in the heavy meson suppression and flow as will be shown in the next chapter when hadronization is included.

4.3 Influence of Initial State Fluctuations on Heavy Quark Energy Loss

As the first application of our modified Langevin framework, we explore the effects of initial state fluctuations in heavy-ion collisions on heavy quark energy loss.

Fluctuations help reveal essential information on physical systems. For example, the temperature inhomogeneity in the Cosmic Microwave Background that evolved from the initial fluctuations after the Big Bang provides valuable knowledge on the cosmological expansion. Similarly, there has been significant effort in studying initial state fluctuations in our "little bang" system, such as the fluctuations of nucleon positions and color charges inside the colliding nuclei [39]. Some of the most interesting consequences of initial state fluctuations include nonzero anisotropy in ultra-central collisions and the presence of odd-order harmonics in initial geometry and collective flow [40, 41, 42, 43, 44, 45, 46, 47, 48, 49]. Elliptic, triangular and other higher-order harmonic flows have been measured at RHIC and LHC [50, 51, 52]. These measurements have triggered great interest in studying the origin of initial state fluctuations, and how they affect the dynamical evolution of the fireball and manifest themselves in final state particle flow and correlations [41, 43, 46, 47, 195, 196, 197, 53]. One of the purposes of these studies is to obtain a quantitative extraction of transport properties such as the shear viscosity of the QGP matter produced in high energy nucleus-nucleus collisions.

Initial conditions, especially the geometry of the heavy-ion collisions, still remain

one of the major uncertainties in the extraction of a precise value for QGP shear viscosity [23, 198, 26]. Various types of fluctuations, such as that of initial transverse flow and longitudinal fluctuations [25, 197], as well as the medium response to jet energy loss [199] may introduce more uncertainties in our understanding of the initial states. The purpose of this section is to investigate the effect of fluctuating initial conditions on the dynamics of heavy quark in medium and whether it is possible to infer information on the initial state fluctuations in heavy-ion collisions from heavy flavor observables.

In most of the literature that studies heavy quark evolution, smooth initial conditions are utilized for hydrodynamic models to simulate the hot and dense medium through which heavy quarks propagate. The influence of initial state fluctuations on heavy quarks has not been studied prior to our work. There have been similar studies on the effect of initial state fluctuations in the context of high p_{T} light flavor jets [200, 201, 202], but no unified conclusion has been reached so far. For instance, Ref. [200] used a (1+1)-dimensional Bjorken hydrodynamic background and found that the fluctuation in the spatial distribution of the initial hard scatterings significantly reduces the suppression of jet production. In Ref. [202] it was found that with the inclusion of the transverse expansion of the medium, i.e., using a (2+1)-dimensional hydrodynamic model, jet energy loss will be enhanced when the initial state fluctuation is incorporated. However, using a (2+1)-dimensional medium for peripheral collisions, Ref. [201] showed a decrease of quenching when initial state fluctuations are included.

In the following, we investigate the influence of initial state fluctuations on heavy quark evolution inside the QGP matter. We simulate the dynamical evolution of heavy quarks using our modified Langevin equation developed in Sec.4.1 that includes both collisional and radiative energy losses. The QGP medium is simulated with a (2+1)-dimensional viscous hydrodynamic model which has been tuned to

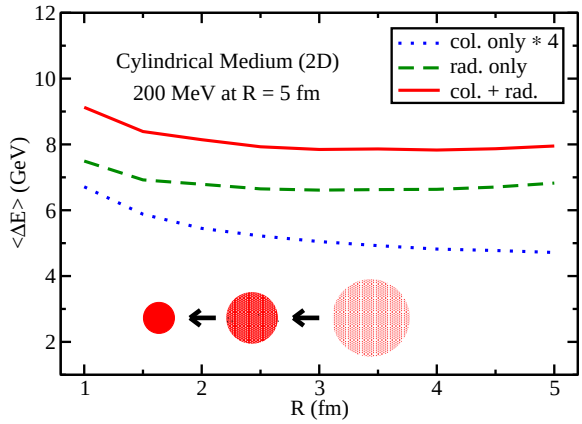

FIGURE 4.4: Energy loss of charm quark as a function of the size of the hot tube.

describe bulk matter observables. We do not aim for a direct comparison with experimental data in this analysis, but focus on exploring how heavy quark evolution and energy loss are affected by the the presence of initial state fluctuations. Finally, we will discuss the prospect of utilizing heavy quarks to probe the granularity of local fluctuations inside the QGP and to improve our knowledge of the initial state of the QGP fireball.

4.3.1 Effects of Fluctuations on Heavy Quarks in a Static Medium

Before exploring the effects of initial state fluctuations of a realistic QGP medium on heavy quark energy loss, we first investigate the influence of local temperature fluctuations (or hot spots) on heavy quark energy loss in a static medium. We will look at two different aspects of density fluctuations: the size and the number of local fluctuations. To mimic the effect of the realistic (2+1)-dimensional boost invariant hydrodynamic medium which we will use in the next subsection, the static medium is chosen to be two dimensional, i.e., the hot spots are in fact hot tubes in this case.

For the first scenario, we generate one cylindrical medium (hot tube) with a constant temperature. As demonstrated by the cartoon inside Fig.4.4, we vary its size and study how the energy loss of charm quarks is affected. When varying the

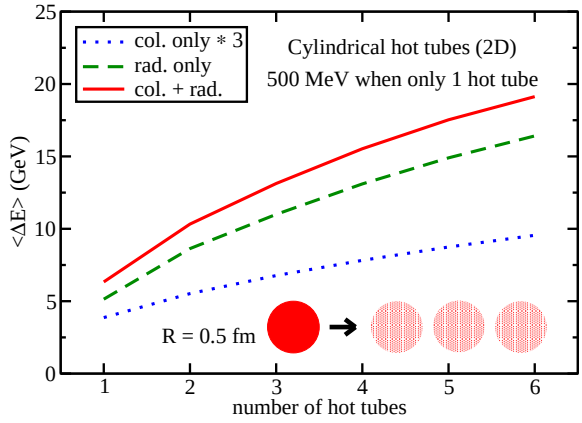

FIGURE 4.5: Energy loss of charm quark as a function of the number of hot tubes.

size, the total energy contained inside the tube is kept fixed. The temperature of the medium is set as 200 MeV when the tube radius is $R = 5$ fm and will increase as the radius decreases. Each charm quark is initialized with 50 GeV and placed at the center of the cylinder. We calculate the average energy loss of charm quarks as they exit the hot tube medium, and the results are shown in Fig.4.4. We also compare the results using different energy loss mechanisms of heavy quarks: collisional energy loss only, radiative only and the combined loss. In the figure we multiply the results from quasi-elastic scatterings by a factor of 4 for a better resolution. From the figure, we observe that the energy loss of charm quarks is not very sensitive to the size of the hot tube (with the total deposited energy unchanged).

To study the effect of the number of local density fluctuations on the heavy quark energy loss, we generate N hot tubes with the same radius $R = 0.5$ fm. As displayed by the cartoon inside Fig.4.5, they are lined up along charm quarks' initial direction of propagation. The initial charm quark energy is set as 50 GeV (placed at the edge of the first hot tube) and the temperature of the medium is set as 500 MeV when there is only one hot tube. Again, when changing the number of hot tubes, the total energy deposited in the medium (sum of the N hot tubes) is fixed. The result for

such scenario is shown in Fig.4.5. We see that the energy loss of charm quarks is quite sensitive to the number of hot tubes.

The above results can be easily understood with the following argument. One may assume the power law dependence for heavy quark energy loss on the medium length and temperature as follows:

$$\Delta E \propto (NR)^{\alpha} T^{\beta}, \quad \epsilon \propto T^4, \quad V \propto NR^d, \tag{4.7}$$

where N is the number of hot tubes, R is the radius of each hot tube probed by heavy quarks, and V is the total volume of the d-dimensional medium. T is the temperature, and ϵ is the medium energy density. The parameters α and β denote power law dependence of heavy quarks on the path length and the medium temperature. Since we fix the total amount of energy contained in the medium, i.e., $\epsilon V = \text{Const.}$, one may obtain the dependence on the size and the number of hot tubes as:

$$\Delta E \propto N^{\alpha-\beta/4} R^{\alpha-\beta d/4}. \tag{4.8}$$

In our energy loss model, $\alpha = 1$ and $\beta = 2$ are good approximations for collisional energy loss, and one may roughly use $1 < \alpha < 2$ (e.g. taking $\alpha = 3/2$ in the following analysis) and $\beta = 3$ for radiative energy loss.

When there is only one hot tube $N = 1$ (the first scenario), Eq.(4.8) is reduced to $\Delta E \propto R^{\alpha-\beta d/4}$. Thus for a 2-dimensional system, this indicates that the total energy loss of heavy quark is not very sensitive to the size R of the hot tubes. This is consistent with Fig. 4.4. We have also checked that for a 1-dimensional system, the total energy loss of heavy quarks decreases when confining the same amount energy in a smaller region, but the energy loss increases for a 3-dimensional system.

Similarly, one may fix the the size R of hot tubes in Eq.(4.8) to isolate the influence of the number of hot tubes: $\Delta E \propto N^{\alpha-\beta/4}$. One can see that the total energy loss does not depend on the dimension of the system, but increases significantly

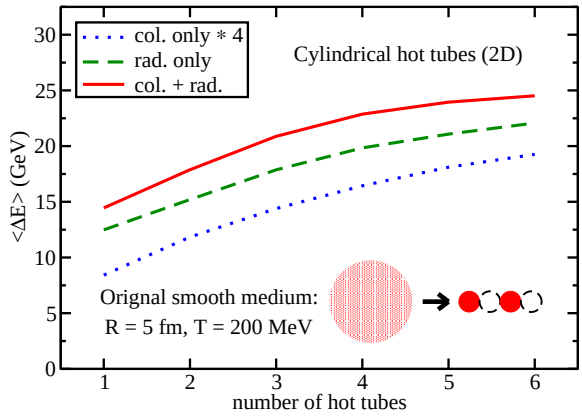

FIGURE 4.6: Effects of the strength of medium fluctuation (number of hot tubes N) on charm quark energy loss.

with the number of hot tubes for both collisional and radiative energy loss. This is consistent with the finding shown in Fig.4.5.

One may combine the above two scenarios, i.e., changing the size and the number of hot spots/tubes simultaneously. This is very similar to the change from a large and smooth medium to fluctuating medium consisting of several hot (and cold) regions as demonstrated by the cartoon inside Fig.4.6. The total energy contained in these two different media are the same. To simplify the study, we split a large smooth tube medium into N hot tubes with smaller sizes, which are lined up adjacent to each other along the direction of the initial momentum of our charm quarks ($E_{\rm init} = 50$ GeV). Another N cold tubes (vacuum here) are also placed between every two hot tubes to mimic the realistic distribution of local density fluctuations. The sizes of the smaller tubes are chosen such that the total length $4NR$ traversed by heavy quarks is fixed as the diameter of the original smooth medium with a radius of 5 fm and temperature of 200 MeV. The results for a 2-dimensional system are shown in Fig.4.6. One observes that the energy loss of charm quarks increases when the original smooth medium is splitted into more hot and cold tubes, i.e., the more fluctuations the medium has, the stronger energy loss the charm quarks experience.

To summarize this subsection, we find that the energy loss of charm quarks in a 2-dimensional system does not have much dependence on the size of the local fluctuations, but is quite sensitive to the number of local fluctuations in the medium. Heavy quarks tend to lose more energy in a fluctuating medium than in a smooth one when the total energy contained in the medium is the same. Although the above results are obtained using a static medium, it provides some guidance to explain the results for a realistic hydrodynamic medium presented in the next section. We also note that our finding is based on the path length and temperature dependence of heavy quark energy loss in our model, i.e., the values of α and β in Eq.(4.8).

4.3.2 Heavy Quarks in Event-by-Event Hydrodynamic Medium

In the previous subsection, we studied the response of heavy quark energy loss to the temperature fluctuations in a static QGP medium. In this subsection, we perform the investigation for a realistic expanding medium in which both temperature fluctuations and flow (fluctuations) are present. Here, we utilize a (2+1)-dimensional viscous hydrodynamic model to simulate the dynamical evolution of a hot QGP produced in Pb-Pb collisions at the LHC energy. The initial conditions for the hydrodynamical evolution are obtained from the Monte-Carlo Glauber model.

In Fig.4.7, we compare the initial entropy density distribution in the transverse plane from a typical event [Fig.4.7(a)] with one after averaging over 100,000 events for 0-7.5% Pb-Pb collisions at 2.76 TeV at the LHC [Fig. 4.7(b)]. We note that in Fig. 4.7(b), the initial profiles of all the events have been rotated to the same second-order participant plane before performing the event average of the entropy density. One can clearly see the presence of hot and cold regions in the QGP fireball for fluctuating initial conditions.

In Fig.4.8, we show the nuclear modification factor $R_{\rm AA}$ of charm quarks after their traversal of the QGP medium created in 2.76 TeV Pb-Pb collisions. We com-

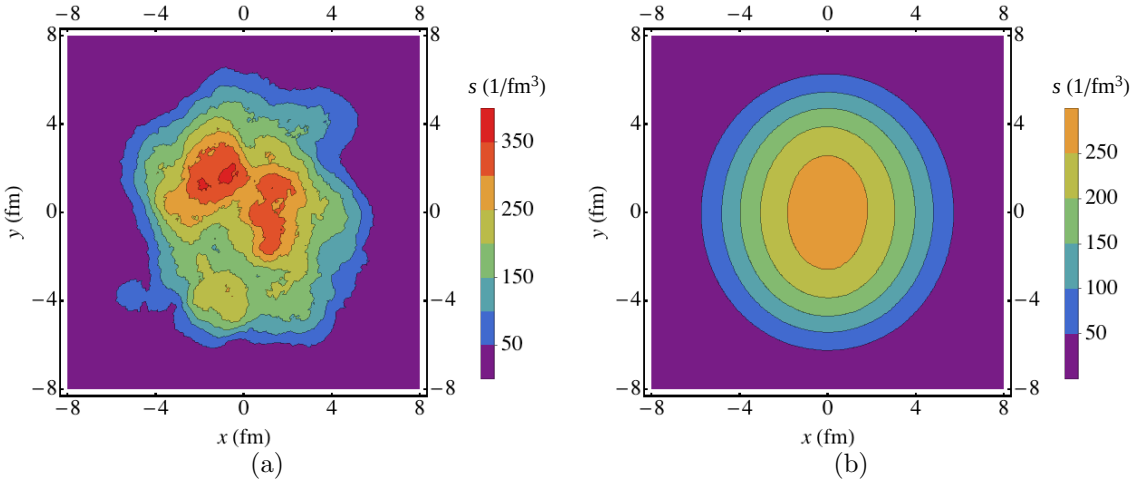

FIGURE 4.7: Comparison between (a) fluctuating and (b) smooth initial entropy density profiles of hydrodynamical evolution of 2.76 TeV central Pb-Pb collisions.

pare the results from smooth initial conditions with those from an event-by-event calculation for four different centralities. One can see from Fig.4.8(a) - 4.8(d) that the event-by-event calculations give larger suppression for heavy quarks at high p_{T}, i.e., the initial state fluctuations lead to larger energy loss for heavy quarks. This is consistent with the finding for the static medium case in the previous subsection. As a consequence, a slightly smaller suppression is observed for low p_{T} charm quarks.

As has been mentioned, there exist temperature fluctuations and flow (fluctuations) in a realistic medium. To remove and investigate the effect of the medium flow on heavy quark evolution, one may solve the Langevin equation Eq.(4.1) in the global center-of-mass frame instead of the local rest frame of the fluid cell (see Sec.3.3.2). In this way, the evolution of heavy quarks is solely affected by the temperature distribution and fluctuations of the medium. One can see that the effect of the medium flow is to boost low p_{T} charm quarks into the medium p_{T} regime and form the bump structure for the nuclear modification factor R_{AA}. This bump feature disappears when flow is switched off in the calculation.

The above observation can be seen more clearly in the subfigures inside Fig.

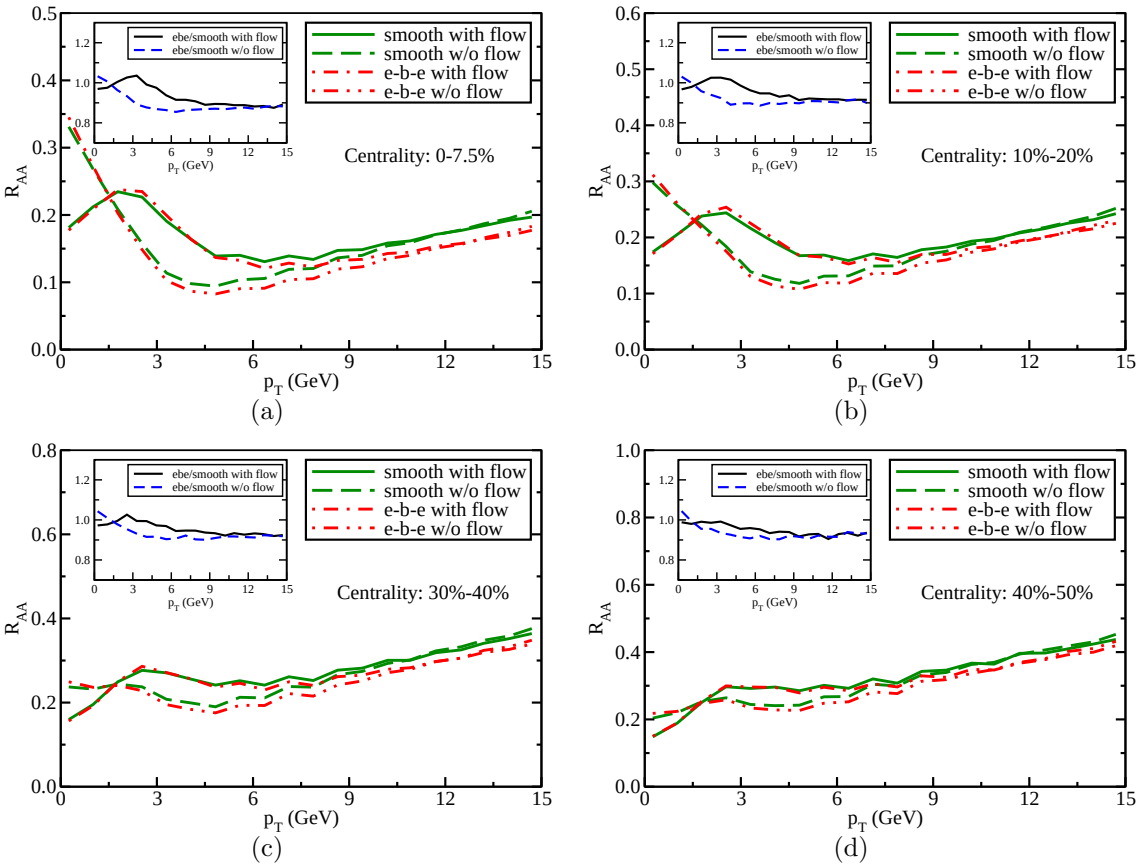

FIGURE 4.8: Comparison of charm quark $R_{\rm AA}$ between calculations with smooth and fluctuating initial conditions of hydrodynamical evolution.

4.8(a) - 4.8(d) where we show the ratios between the final state $p_{\rm T}$ spectra of charm quarks from the event-by-event calculations and those from the smooth cases. For the central collisions [Fig. 4.8(a)], we obtain about 12% more quenching at high $p_{\rm T}$ for the fluctuating initial condition as compared to the smooth initial condition. This could result in a 10%-15% difference in the extraction of the gluon transport coefficient $\hat{q}$ inside QGP. For more peripheral collisions, the effect of initial state fluctuations on heavy quark energy loss is less; the quenching increases about 7% when switching from the smooth to the fluctuating initial condition in 40%-50% Pb-Pb collisions [Fig. 4.8(d)].

To summarize this section, we have studied the impact of initial state fluctua-

tions on heavy quark evolution and energy loss in relativistic heavy-ion collisions. The in-medium evolution of heavy quarks is described using our modified Langevin equation that simultaneously incorporates collisional and radiative energy loss components. We have investigated the effect of local fluctuations for both static and realistic expanding QGP media. In static media, we have studied the effects of temperature fluctuations on heavy quark energy loss in terms of the size and the number of local fluctuations (hot spots), and found that the total energy loss of heavy quarks is not particularly sensitive to the size of local fluctuations in a 2-dimensional system, but the energy loss increases significantly with the increasing number of hot spots. Our simulation in a realistic QGP medium has demonstrated that fluctuating initial conditions may yield about 10% more suppression for inclusive charm quark production at high p_{T} in relativistic nucleus-nucleus collisions. The effect of initial state fluctuations on heavy quark energy loss tends to diminish for more peripheral collisions.

Our study constitutes an important contribution to the quantitative understanding of heavy quark dynamics in relativistic heavy-ion collisions with initial state fluctuations. Although we utilize heavy quarks in our study to probe the effects of the fluctuations, many of our results should apply to light flavor partons as well. Our results suggest that jet modification might be utilized to probe the fluctuations of the QGP medium, such as the degree of inhomogeneity or the number of hot spots. We further note that the sensitivity of heavy quark energy loss to hot spot number might be enhanced when one uses correlation measurements or triggered observables; we leave such study to a future effort. The study along this direction may potentially provide more constraints on modeling initial states, thus helping our quantitative understanding of the transport properties of the hot and dense QGP produced in high energy heavy-ion collisions.

5

Hadronization of Heavy Quarks

In Chapter 3 and Chapter 4, we have developed an improved Langevin framework to describe the heavy quark evolution in a QGP matter, simultaneously incorporating collisional and radiative energy loss. After these heavy quarks exit the color deconfined region of the medium (i.e., when the local temperature falls below the critical temperature T_c), they are forced to hadronize into their hadronic bound states. In this chapter, we will construct a model to describe this hadronization process.

High p_T heavy quarks tend to fragment into lower energy partons among which the hadronic bound state of heavy flavor can be formed. This process is termed as "fragmentation". On the other hand, it is more probable for a lower p_T heavy quark to combine with thermal partons from the QGP medium to form new hadrons. This mechanism is known as heavy-light "coalescence" or "recombination". We will develop a hybrid fragmentation plus recombination model in this chapter to simulate the hadronization process of heavy quarks at all momentum scales. In this application, we adopt a "sudden recombination" approach for heavy quark coalescence with light quarks from the QGP medium. This approach was first developed for light hadrons formed from bulk matter [138, 31, 139, 140], and then applied to heavy

flavors [103, 104, 105] and recently to partonic jet hadronization [141]. This coalescence model does not require the thermalization of the recombining partons and it is straightforward to simultaneously include mesons and baryons, which is convenient for the normalization over all possible hadronization channels. Note that an alternative approach, based on the resonance recombination [101, 142, 106], may also be applied to the study of heavy flavor dynamics. For the fragmentation mechanism, we utilize PYTHIA 6.4 [137] to simulate the conversion from heavy quark to heavy flavor hadrons.

This chapter will be organized as follows. In Sec.5.1, we will summarize how the fragmentation process is simulated in PYTHIA. In Sec.5.2, we will introduce the coalescence model we utilize for calculating the heavy-light recombination process. We will then construct our hybrid model in Sec.5.3 for heavy quark hadronization incorporating both mechanisms, and compare the contributions from each process to the spectra of the produced heavy mesons. Finally, in Sec.5.4, we will apply our hadronization model to the heavy quarks emerging from the Langevin evolution through the QGP, calculate the heavy flavor $R_{\rm AA}$ and v_2 and compare them with the existing data from both RHIC and LHC experiments; predictions of future measurements will also be provided. Major results in this chapter have been originally published in Ref. [107].

5.1 Heavy Quark Fragmentation

In this work, we utilize PYTHIA 6.4 [137] to implement the fragmentation of heavy quarks into heavy flavor hadrons. By default, the Lund symmetric fragmentation function [203] is selected:

$$f(z) \propto \frac{1}{z} z^{a_\alpha} \left(\frac{1-z}{z}\right)^{a_\beta} \exp\left(-\frac{b m_\perp^2}{z}\right), \tag{5.1}$$

where $m_\perp$ is the transverse momentum defined as $m_\perp^2 = E^2 - p_z^2$, and z is the fraction of $E + p_z$ taken by the fragmented hadron out of the parent quark. In Eq.(5.1), a_α, a_β and b are the parameters which need to be fixed according to experimental data, in which α corresponds to the "old" flavor and β corresponds to the "new" flavor in the fragmentation process. While Eq.(5.1) works well for light quark fragmentation, its predictions for heavy meson spectra deviate from experimental data. In PYTHIA, for the simulation of heavy quark fragmentation, Eq.(5.1) is modified according to the Bowler space-time picture of string evolution [191]:

$$f(z) \propto \frac{1}{z^{1+r_Q b m_Q^2}} z^{a_\alpha} \left(\frac{1-z}{z}\right)^{a_\beta} \exp\left(-\frac{b m_\perp^2}{z}\right). \tag{5.2}$$

In our work, we use the default parametrization as $a_\alpha = a_\beta = 0.5$ GeV^{-2}, $b = 0.9$ GeV^{-2} and $r_Q = 1$.

In the literature, an alternative fragmentation function – the Peterson fragmentation function [204] – is widely adopted for heavy quark fragmentation:

$$f(z) \propto \frac{1}{z\left(1 - \frac{1}{z} - \frac{\epsilon_Q}{1-z}\right)^2}, \tag{5.3}$$

with $\epsilon_Q = -0.05$ for the charm quark and -0.005 for the bottom quark. This option has also been incorporated into PYTHIA and we have verified that it provides very similar heavy meson spectra compared to those given by Eq.(5.2).

In the numerical implementation, an iterative method is used to simulate the fragmentation process. For instance, one may start with a single quark q_0. Then a new $q_1\bar{q}_1$ pair may be produced, such that $q_0\bar{q}_1$ forms a new meson whose energy and momentum is given by a proper fragmentation function as shown above, and q_1 is left for the next fragmentation process until the leftover quark is not energetic enough to further fragment. The choice of the flavor of $q\bar{q}$ is determined with the probability due to mass, by default, $u\bar{u} : d\bar{d} : s\bar{s} = 1 : 1 : \gamma_s$ where γ_s is set

to 0.3, and no heavy quark pair is produced in the current fragmentation process. Once the flavor is chosen, the spin of the valence quark S and the internal orbital angular momentum L is assigned according to parameterized relative probabilities. For baryon formation, a diquark $\bar{q}q$ might be picked instead of a single q by q_0. This is known as the "diquark picture" in PYTHIA. Meanwhile, alternative ways to form baryons also exist, such as the "simple popcorn" and the "advanced popcorn" frameworks. One may refer to the above mentioned manual [137] for more details.

5.2 Heavy-light Quark Coalescence

In this section, we introduce a Wigner function that describes the probability for two partons to combine into a meson. Although we utilize a two particle system as an example here, this Wigner formalism can be easily generalized to a three body system for baryon formation, as will be shown in the next section.

5.2.1 The Coalescence Probability: the Wigner Function

The probability for two partons to combine into a meson can be expressed in terms of the overlap between the wavefunctions of the initial two partons and the final meson – $|\langle M|\vec{k}_1,\vec{r}_1;\vec{k}_2,\vec{r}_2\rangle|^2$, where $\vec{k}_1,\vec{r}_1$ and $\vec{k}_2,\vec{r}_2$ are the momenta and positions of the two initial free partons and M represents the formed meson.

In a fixed volume V, the wavefuctions of the partons and the combined meson can be written as:

$$\begin{aligned}\langle\vec{r}_1|\vec{k}_1\rangle &= \frac{1}{\sqrt{V}}e^{-i\vec{k}_1\cdot\vec{r}_1},\\ \langle\vec{r}_2|\vec{k}_2\rangle &= \frac{1}{\sqrt{V}}e^{-i\vec{k}_2\cdot\vec{r}_2},\\ \langle\vec{r}|M\rangle &= \frac{1}{\sqrt{V}}\phi_M(\vec{r})e^{-i\vec{K}\cdot\vec{R}},\end{aligned} \tag{5.4}$$

in which $\phi_M(\vec{r})$ is the wavefunction of the mesonic bound state in its rest frame and

we have defined the total momentum, relative momentum, center-of-mass position and relative position as

$$\begin{aligned}
\vec{K} &= \vec{k}_1 + \vec{k}_2, \\
\vec{k} &= \frac{m_2\vec{k}_1 - m_1\vec{k}_2}{m_1 + m_2}, \\
\vec{R} &= \frac{m_1\vec{r}_1 + m_2\vec{r}_2}{m_1 + m_2}, \\
\vec{r} &= \vec{r}_1 - \vec{r}_2.
\end{aligned} \tag{5.5}$$

Note that with the transformations in Eq.(5.5), we have

$$\vec{K}\cdot\vec{R} + \vec{k}\cdot\vec{r} = \vec{k}_1\cdot\vec{r}_1 + \vec{k}_2\cdot\vec{r}_2, \tag{5.6}$$

$$\mathcal{J}\left[\frac{\partial(\vec{R},\vec{r})}{\partial(\vec{r}_1,\vec{r}_2)}\right] = \begin{vmatrix} \partial\vec{R}/\partial\vec{r}_1 & \partial\vec{R}/\partial\vec{r}_2 \\ \partial\vec{r}/\partial\vec{r}_1 & \partial\vec{r}/\partial\vec{r}_2 \end{vmatrix} = -1. \tag{5.7}$$

With these relations, we may calculate the overlap between the wavefunctions as follows

$$\begin{aligned}
\langle M|\vec{k}_1,\vec{r}_1;\vec{k}_2,\vec{r}_2\rangle &= \int d^3r_1 \int d^3r_2 \frac{1}{\sqrt{V}} e^{-i\vec{k}_1\cdot\vec{r}_1} \frac{1}{\sqrt{V}} e^{-i\vec{k}_2\cdot\vec{r}_2} \frac{1}{\sqrt{V}} \phi_M^*(\vec{r}) e^{i\vec{K}\cdot\vec{R}} \\
&= \int d^3R \int d^3r \left|\mathcal{J}\left[\frac{\partial(\vec{r}_1,\vec{r}_2)}{\partial(\vec{R},\vec{r})}\right]\right| \frac{1}{V^{3/2}} e^{-i(\vec{K}\cdot\vec{R}+\vec{k}\cdot\vec{r})} \phi_M^*(\vec{r}) e^{i\vec{K}\cdot\vec{R}} \\
&= \int d^3r \frac{1}{\sqrt{V}} e^{-i\vec{k}\cdot\vec{r}} \phi_M^*(\vec{r}).
\end{aligned} \tag{5.8}$$

And thus we have the coalescence probability as below:

$$\left|\langle M|\vec{k}_1,\vec{r}_1;\vec{k}_2,\vec{r}_2\rangle\right|^2 = \int d^3r \int d^3r' \frac{1}{V} \phi_M^*(\vec{r})\phi_M(\vec{r}') e^{-i\vec{k}\cdot\vec{r}} e^{i\vec{k}\cdot\vec{r}'}. \tag{5.9}$$

One may further simplify this probability with the following Wigner transformation:

$$\vec{Q} = \frac{1}{2}(\vec{r} + \vec{r}'), \qquad \vec{s} = \vec{r} - \vec{r}', \tag{5.10}$$

whose Jacobian is also -1 as above. Thus, Eq.(5.9) can be re-written as

$$\left|\langle M|\vec{k}_1,\vec{r}_1;\vec{k}_2,\vec{r}_2\rangle\right|^2 = \int d^3Q \int d^3s \frac{1}{V}\phi_M^*(\vec{Q}+\vec{s}/2)\phi_M(\vec{Q}-\vec{s}/2)e^{-i\vec{k}\cdot\vec{s}}$$
$$= \int \frac{d^3r}{V} f_M^W(\vec{r},\vec{k}), \tag{5.11}$$

where we have substituted $\vec{Q}$ by $\vec{r}$ in the second line considering that the above probability decreases exponentially when $\vec{r}$ is away from $\vec{r}'$, and defined the Wigner function as

$$f_M^W(\vec{r},\vec{k}) \equiv \int d^3s \phi_M^*(\vec{r}+\vec{s}/2)\phi_M(\vec{r}-\vec{s}/2)e^{-i\vec{k}\cdot\vec{s}}. \tag{5.12}$$

This Wigner function represents the probability for two partons with relative position $\vec{r}$ and relative momentum $\vec{k}$ to combine into a meson. One may verify that the integral of the Wigner function over the whole phase space gives the total volume:

$$\int d^3r \int d^3k f_M^W(\vec{r},\vec{k}) = \int d^3k \int d^3r \int d^3s \phi_M^*(\vec{r}+\vec{s}/2)\phi_M(\vec{r}-\vec{s}/2)e^{-i\vec{k}\cdot\vec{s}}$$
$$= \int d^3r \int d^3s \phi_M^*(\vec{r}+\vec{s}/2)\phi_M(\vec{r}-\vec{s}/2)V\delta^{(3)}(\vec{s})$$
$$= V\int d^3r \phi_M^*(\vec{r})\phi_M(\vec{r})$$
$$= V. \tag{5.13}$$

In an infinite medium, this normalizes to $(2\pi)^3$ instead with the identity $\int d^3k e^{-i\vec{k}\cdot\vec{s}} = (2\pi)^3\delta^{(3)}(\vec{s})$.

With the knowledge of the meson wavefunction $\phi_M(\vec{r})$, the Wigner function Eq.(5.12) is determined. We will use the model of a simple quantum mechanic harmonic oscillator to approximate this wavefunction:

$$\phi_M(\vec{r}) = \left(\frac{\mu\omega}{\pi}\right)^{3/4} e^{-\frac{1}{2}\mu\omega r^2}, \tag{5.14}$$

where $\mu = m_1 m_2/(m_1+m_2)$ is the reduced mass and ω is the angular frequency of the harmonic oscillator which will be discussed later. By substituting Eq.(5.14) into Eq.(5.12), we have

$$\begin{aligned} f_M^W(\vec{r},\vec{k}) &= \int d^3s e^{-i\vec{k}\cdot\vec{s}} \left(\frac{\mu\omega}{\pi}\right)^{3/2} e^{-\frac{1}{2}\mu\omega(\vec{r}+\vec{s}/2)^2-\frac{1}{2}\mu\omega(\vec{r}-\vec{s}/2)^2} \\ &= 2\pi \int_{-1}^{1} d(\cos\theta) \int_0^\infty s^2 ds \left(\frac{\mu\omega}{\pi}\right)^{3/2} e^{-\mu\omega r^2} e^{-\mu\omega s^2/4} e^{-iks\cos\theta} \\ &= 2\pi \left(\frac{\mu\omega}{\pi}\right)^{3/2} e^{-\mu\omega r^2} \int_0^\infty s^2 ds e^{-\mu\omega s^2/4} \frac{1}{-iks}\left(e^{-iks}-e^{iks}\right) \\ &= 2\pi \left(\frac{\mu\omega}{\pi}\right)^{3/2} e^{-\mu\omega r^2} \frac{1}{ik} e^{-\frac{1}{\mu\omega}k^2} \int_0^\infty ds s \left[e^{-\frac{1}{4}\mu\omega\left(s-\frac{2i}{\mu\omega}k\right)^2} - e^{-\frac{1}{4}\mu\omega\left(s+\frac{2i}{\mu\omega}k\right)^2}\right] \end{aligned} \tag{5.15}$$

One may change the variables of the two parts of integral in the last line with $\xi = s - \frac{2i}{\mu\omega}k$ and $\xi = s + \frac{2i}{\mu\omega}k$ respectively. The integral is then re-written as

$$\begin{aligned} &\int_{-\frac{2i}{\mu\omega}k}^\infty d\xi \left(\xi + \frac{2i}{\mu\omega}k\right) e^{-\frac{1}{4}\mu\omega\xi^2} - \int_{\frac{2i}{\mu\omega}k}^\infty d\xi \left(\xi - \frac{2i}{\mu\omega}k\right) e^{-\frac{1}{4}\mu\omega\xi^2} \\ &= \int_{-\frac{2i}{\mu\omega}k}^{\frac{2i}{\mu\omega}k} d\xi \xi e^{-\frac{1}{4}\mu\omega\xi^2} + \frac{2i}{\mu\omega}k \int_{-\infty}^\infty d\xi e^{-\frac{1}{4}\mu\omega\xi^2} \\ &= 0 + \frac{2i}{\mu\omega}k\sqrt{\frac{4\pi}{\mu\omega}}, \end{aligned} \tag{5.16}$$

where the symmetry of $\exp(-\mu\omega\xi^2/4)$ about $\xi = 0$ is applied. By inserting Eq.(5.16) into Eq.(5.15), we obtain

$$f_M^W(\vec{r},\vec{k}) = 8e^{-\mu\omega r^2} e^{-\frac{1}{\mu\omega}k^2} = 8e^{-r^2/\sigma^2} e^{-\sigma^2 k^2}, \tag{5.17}$$

in which we define $\sigma \equiv \sqrt{1/(\mu\omega)}$. In the end, we may add a degeneracy factor g_M:

$$f_M^W(\vec{r},\vec{k}) = 8g_M e^{-r^2/\sigma^2} e^{-\sigma^2 k^2}, \tag{5.18}$$

which takes into account the spin-color degrees of freedom. For instance, g_M is $1/(2\times3\times2\times3) = 1/36$ for the D meson ground state, and $3/(2\times3\times2\times3) = 1/12$ for the first excited state of D meson.

5.2.2 The ω Parameter in the Wigner Function

In principle, the σ parameter in Eq.(5.18) can be determined by the size (radius) of the formed meson. In the non-relativistic limit, the charge radius of a two particle system (with the same sign of charges) can be defined as

$$\left\langle r_M^2 \right\rangle = \left\langle \frac{Q_1(\vec{r}_1 - \vec{R})^2 + Q_2(\vec{r}_2 - \vec{R})^2}{Q_1 + Q_2} \right\rangle . \tag{5.19}$$

From Eq.(5.5), we have

$$\begin{aligned} \vec{r}_1 &= \vec{R} + \frac{m_2}{m_1 + m_2}\vec{r}, \\ \vec{r}_2 &= \vec{R} - \frac{m_1}{m_1 + m_2}\vec{r}. \end{aligned} \tag{5.20}$$

By substituting Eq.(5.25) into Eq.(5.19), we have

$$\left\langle r_M^2 \right\rangle = \frac{Q_1 m_2^2 + Q_2 m_1^2}{(Q_1 + Q_2)(m_1 + m_2)^2} \left\langle r^2 \right\rangle . \tag{5.21}$$

Meanwhile, we may evaluate the average distance square $\langle r^2 \rangle$ from the Wigner function:

$$\left\langle r^2 \right\rangle = \frac{\int d^3r d^3k r^2 f_M(\vec{r}, \vec{q})}{\int d^3r d^3k f_M(\vec{r}, \vec{q})} = \frac{12\pi^3\sigma^2}{(2\pi)^3} = \frac{3}{2}\sigma^2. \tag{5.22}$$

Therefore we have,

$$\left\langle r_M^2 \right\rangle = \frac{3}{2}\frac{1}{\mu\omega}\frac{Q_1 m_2^2 + Q_2 m_1^2}{(Q_1 + Q_2)(m_1 + m_2)^2}. \tag{5.23}$$

For instance, one may take 0.184 fm^2 for $D^+(c\bar{u})$ and 0.378 fm^2 for $B^+(\bar{b}d)$ as the charge radii square predicted by the light-front quark model [205]. In this work, we take thermal masses of 300 MeV for u and d quarks and 475 MeV for s quarks. On the other hand, heavy quarks are not required to be thermal in this coalescence model and their masses are taken as 1.27 GeV for c and 4.19 GeV for b quarks. These

yield $\omega \approx 0.32$ GeV for both D^+ and B^+. However, as discussed in Ref.[105], in order to convert as many heavy quarks at small $p_{\rm T}$ into heavy hadrons via coalescence as possible, smaller oscillator frequencies are needed. We use the parameters tuned in that reference – $\omega_c = 0.106$ GeV for c quark and $\omega_b = 0.059$ GeV for b quark – for our calculation. These smaller oscillator frequencies may partly result from larger radii of mesons in a de-confined QGP matter than in vacuum. Note that in principle, the oscillator frequency could depend on the type of hadrons. However, for a "minimal model", we only use one overall tuned parameter for charm hadrons and one for bottom hadrons as shown above.

5.2.3 A Relativistic Correction

The above Wigner function is constructed in a classical framework, when applying it to the heavy-light quark coalescence in relativistic heavy-ion collisions, we implement a correction to the transformation Eq.(5.5) as follows. We first define the velocity of the center-of-mass frame of the heavy-light quark system as

$$\beta = \frac{\vec{k}_1 + \vec{k}_2}{E_1 + E_2}. \tag{5.24}$$

Then, we boost both the 4-space and 4-momentum vector into this center-of-mass frame and re-define Eq.(5.5) as

$$\begin{aligned} \vec{K} &= \vec{k}'_1 + \vec{k}'_2, \\ \vec{k} &= \frac{E'_2\vec{k}'_1 - E'_1\vec{k}'_2}{E'_1 + E'_2}, \\ \vec{R} &= \frac{E'_1\vec{r}'_1 + E'_2\vec{r}'_2}{E'_1 + E'_2}, \\ \vec{r} &= \vec{r}'_1 - \vec{r}'_2. \end{aligned} \tag{5.25}$$

Note that all the variables with "prime" in Eq.(5.25) are defined in the center-of-mass frame of the heavy-light quark system, i.e., the meson system. With these

definitions, the construction of the Wigner function is the same as that in Sec.5.2.1. This Wigner function method can be easily generalized to a three parton system for baryon formation, which will also be incorporated in our implementation as described in the following section.

5.3 A Hybrid Fragmentation plus Coalescence Model

5.3.1 Fragmentation vs. Coalescence Probability

In the "instantaneous coalescence" model introduced above, the momentum distributions of produced mesons and baryons can be determined by the following expressions,

$$\frac{dN_M}{d^3p_M} = \int d^3p_1 d^3p_2 \frac{dN_1}{d^3p_1}\frac{dN_2}{d^3p_2} f_M^W(\vec{p}_1,\vec{p}_2)\delta(\vec{p}_M - \vec{p}_1 - \vec{p}_2), \tag{5.26}$$

$$\frac{dN_B}{d^3p_B} = \int d^3p_1 d^3p_2 d^3p_3 \frac{dN_1}{d^3p_1}\frac{dN_2}{d^3p_2}\frac{dN_3}{d^3p_3} f_B^W(\vec{p}_1,\vec{p}_2,\vec{p}_3)\delta(\vec{p}_M - \vec{p}_1 - \vec{p}_2 - \vec{p}_3). \tag{5.27}$$

dN_i/d^3p_i represents the momentum distribution of the i-th valence parton in the recombined meson or baryon. The distribution of heavy quarks can be directly obtained after their Langevin evolution through the thermalized medium. For light quarks and anti-quarks from the QGP medium, we take the Fermi-Dirac distribution in the local cell frame [1]:

$$\frac{dN_q}{d^3p} = \frac{g_q V}{e^{\sqrt{p^2+m^2}/T_c}+1}, \tag{5.28}$$

where a uniform distribution in the position space is assumed inside a volume V and $g_q = 6$ denotes the degrees of freedom for each quark flavor. f^W is the Wigner function constructed in the previous section. For a two particle system, we have

$$f_M^W(\vec{r},\vec{k}) = 8N g_M e^{-r^2/\sigma^2} e^{-\sigma^2 k^2}. \tag{5.29}$$

[1] To be rigorous, viscous corrections should be introduced for the momentum distribution of thermal partons if one uses a viscous hydrodynamic medium. However, it has been verified that non-negligible effects on the final state spectra only appear for light partons with energy greater than 2 GeV, which is beyond the dominant regime of our coalescence model.

Note that compared with Eq.(5.18), an overall normalization factor N has been added, which will be discussed later. The relative position $\vec{r}$ and momentum $\vec{k}$ are defined as before [Eq.(5.25)]:

$$\begin{aligned} \vec{r} \equiv & \vec{r}_1' - \vec{r}_2', \\ \vec{k} \equiv & \frac{1}{E_1' + E_2'}(E_2'\vec{p}_1' - E_1'\vec{p}_2'), \end{aligned} \tag{5.30}$$

in which the variables on the right-hand side are defined in the center of mass frame of the two-particle system, i.e., the meson frame. With the assumption that thermal partons have a uniform spatial distribution in the cell frame of the medium, one may average over the position space of Eq.(5.29) and obtain the following momentum space Wigner function:

$$f_M^W(k^2) = \frac{1}{V}\int d^3r f_M^W(\vec{r}, \vec{k}) = N g_M \frac{(2\sqrt{\pi}\sigma)^3}{V} e^{-k^2\sigma^2}. \tag{5.31}$$

From Eq.(5.31) and the definition of $\vec{k}$ in Eq.(5.30), we note that in this instantaneous coalescence model, quarks with similar velocities are most probable to combine to form new hadrons.

The Wigner function can be straightforwardly generalized to a three particle system for baryon production by recombining two particles first and then using their center of mass to recombine with the third one. This yields:

$$f_B^W(k_1^2, k_2^2) = N g_B \frac{(2\sqrt{\pi})^6(\sigma_1\sigma_2)^3}{V^2} e^{-k_1^2\sigma_1^2 - k_2^2\sigma_2^2}, \tag{5.32}$$

where the relative momenta are defined in the center of mass frame of the produced baryon as

$$\begin{aligned} \vec{k}_1 \equiv & \frac{1}{E_1' + E_2'}(E_2'\vec{p}_1' - E_2'\vec{p}_2'), \\ \vec{k}_2 \equiv & \frac{1}{E_1' + E_2' + E_3'}\left[E_3'(\vec{p}_1' + \vec{p}_2') - (E_1' + E_2')\vec{p}_3'\right]; \end{aligned} \tag{5.33}$$

and the width parameters σ_i's are given by $\sigma_i = 1/\sqrt{\mu_i \omega}$ with

$$\mu_1 = \frac{m_1 m_2}{m_1 + m_2}, \qquad \mu_2 = \frac{(m_1 + m_2) m_3}{m_1 + m_2 + m_3}. \tag{5.34}$$

This is known as the "three quark model" for baryon formation. An alternative way – the "diquark model" – has also been discussed in Ref. [105] and may result in slightly different spectra of heavy flavor hadrons at low $p_{\rm T}$.

As discussed in Sec.5.2.2, the oscillator frequency ω can in principle be calculated with the charge radius and is different for each hadron. Here, for a minimal model, we adopt the average values of 0.106 GeV for charm hadrons and 0.059 GeV for bottom hadrons as tuned in Ref. [105].

We use the Wigner functions Eqs.(5.31) and (5.32) to calculate the probability for a heavy quark after its in-medium evolution to produce a hadron through coalescence with light quarks from the QGP medium at $T_{\rm c}$. The overall normalization factor N is determined by requiring the recombination probability to be 1 for a zero-momentum heavy quark to all possible heavy flavor meson and baryon channels (we include both ground states and first excited states of D/B, Λ_Q, Σ_Q, Ξ_Q and Ω_Q). The value of the normalization factor is obtained using a static medium with an effective temperature of $T_{\rm eff} = 175$ MeV. This effective temperature is chosen to take into account the effect of radial flow (around $0.6c$ at $T_{\rm c}$) developed in the hydrodynamic model, and obtained according to the following equation,

$$\sum_{\rm flavors} \int d^3p \frac{g_q V}{e^{E/T_{\rm eff}} + 1} = \sum_{\rm flavors} \int d^3p \frac{g_q V}{e^{p\cdot u/T_{\rm c}} + 1}. \tag{5.35}$$

With the choice of $T_{\rm eff} = 175$ MeV and $T_{\rm c} = 165$ MeV, both sides of Eq.(5.35) lead to the same parton density: a number density around 0.24 fm^{-3} for u and d, and 0.13 fm^{-3} for s quark. More discussions about this effective temperature can be found in Refs. [105, 206].

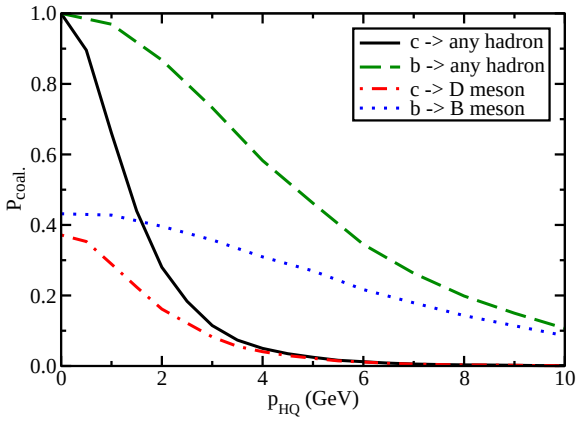

FIGURE 5.1: The coalescence probabilities for heavy-light quarks as a functions of the heavy quark momentum.

Now we may calculate the coalescence probability as a function of the heavy quark momentum as shown in Fig. 5.1. The recombination probabilities for a charm or bottom quark to all heavy flavor hadron channels and to only D or B meson are shown for comparison. One observes that for the same $p_{\rm T}$, bottom quarks have larger recombination probability than charm quarks to produce heavy flavor hadrons due to their larger masses. The curves in the figure separate the hadronization of a charm or bottom quark into three possibilities: recombination to D or B meson, recombination to other hadron channels and fragmentation. In the numerical implementation, a random number between 0 and 1 is generated. If it is greater than the probability of "$Q \to$ any hadron", the heavy quark will not hadronize via coalescence, instead, it fragments through PYTHIA as discussed in Sec.5.1, where the relative ratios between different hadronization channels have been properly calculated and normalized. However, if this random number is smaller than the probability of "$Q \to D/B$", then a D or B meson is formed via the heavy-light quark coalescence. In that case, a u or d quark is generated according to Eq.(5.28) in the cell frame of the medium and then boosted back into the lab frame to combine with the given heavy quark according to the probability governed by Eq.(5.31) – if they do not combine, another light quark

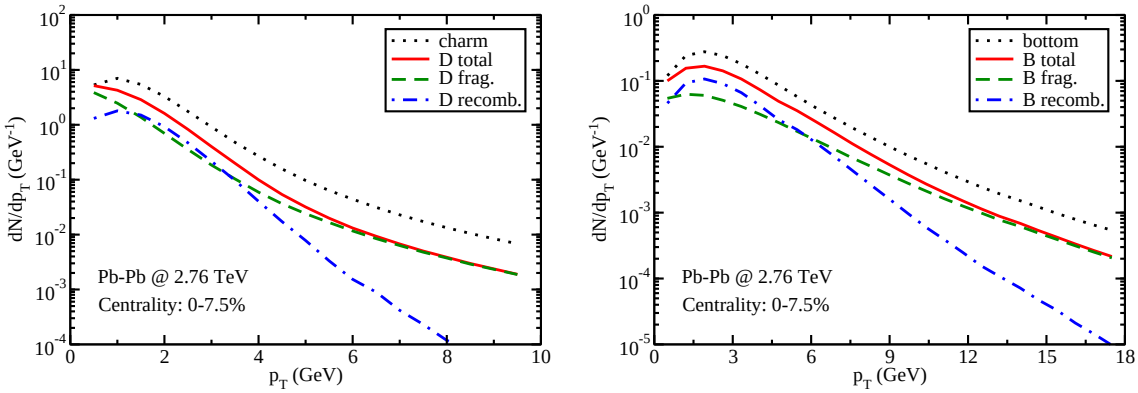

FIGURE 5.2: The relative contributions from different hadronization mechanisms to (a) D and (b) B meson production from heavy quarks (normalized to one heavy quark).

will be generated until the meson is formed. In the end, if the random number resides in the range in between, this heavy quark will hadronize through coalescence, but to other hadrons than D or B meson. In this work, we concentrate on the ground states and the first excited states of D^0, D^+, B^0, B^+ and their anti-particles. A detailed analysis of heavy flavor strange mesons and baryons will be left for a future effort.

5.3.2 Heavy Meson Spectra

With the hybrid model developed in the previous subsection, we may calculate the spectra of heavy mesons formed from heavy quarks after their in-medium evolution. The initialization of heavy quarks and the QGP, the hydrodynamical evolution of the medium and the Langevin evolution of heavy quarks inside QGP will all be calculated as discussed in Chapter 4. Figure 5.2 illustrates the relative contributions from recombination and fragmentation mechanisms to the production of heavy flavor mesons from charm and bottom quarks created in 2.76 TeV central Pb-Pb collisions. One can see that while the fragmentation dominates the D/B meson production at high p_{T}, the inclusion of the recombination mechanism greatly increases their yield at intermediate p_{T}. As the recombination mechanism adds a thermal parton to a

heavy quark, the momentum distribution of D/B mesons through recombination is shifted to the right (higher momenta) compared to charm/bottom quark distribution. Consequently, its contribution to D/B meson production at low $p_{\rm T}$ is not as significant as at intermediate $p_{\rm T}$. Furthermore, due to the larger mass of b-quarks, the contribution from the recombination mechanism to the B meson production is more prominent than to the D meson over a wider $p_{\rm T}$ range. These effects will significantly influence heavy meson suppression and flow as will be shown in the following section.

5.4 Heavy Flavor Suppression and Flow at RHIC and LHC

In this section, we combine our models of heavy flavor initial production, in-medium evolution and fragmentation plus coalescence hadronization from Chapter 2 through Chapter 5 and calculate the heavy flavor suppression and elliptic flow. The nuclear modification factor $R_{\rm AA}$ and the elliptic flow v_2 will be analyzed according to definitions in Eqs.(3.55) and (3.56). We will first compare our numerical results for the D meson suppression and flow with existing data from RHIC and LHC experiments. After that, we will also display some of our predictions for the future measurements, or measurements that are still in progress at this moment. If not otherwise specified, we analyze our results in the mid-rapidity region as $-0.5 < y < 0.5$ for LHC experiments and $-1 < y < 1$ for RHIC experiments.

5.4.1 D Meson Suppression and Flow

In this subsection, we show our numerical results of the D meson suppression and flow, and compare them with experimental data from both RHIC and LHC.

In Fig.5.3, we display our calculation of the D meson $R_{\rm AA}$ for central Pb-Pb collisions at LHC. Contributions from different energy loss mechanisms are shown. One observes that while the collisional energy loss dominates the low $p_{\rm T}$ regime, gluon

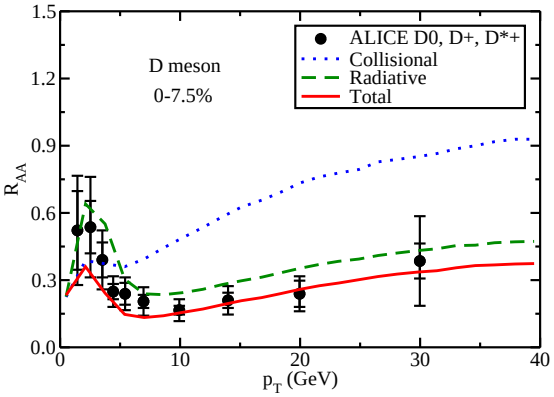

FIGURE 5.3: The nuclear modification factor $R_{\rm AA}$ of D mesons in central Pb-Pb collisions at 2.76 TeV, compared between different energy loss mechanisms.

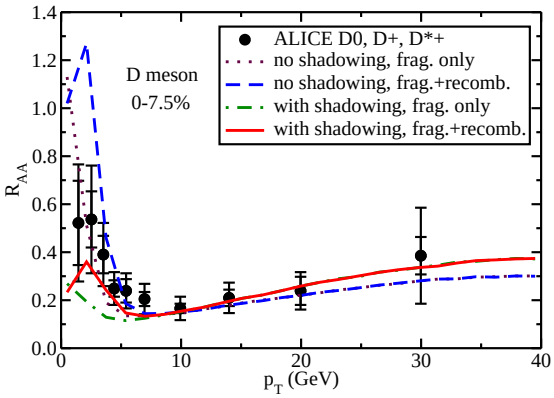

FIGURE 5.4: The $R_{\rm AA}$ of D mesons in central Pb-Pb collisions at 2.76 TeV, compared between different initial production and hadronization mechanisms.

radiation dominates at high $p_{\rm T}$. This is consistent with our findings in Sec.4.2. Our combination of the two mechanisms provides a good description of the experimental data from the ALICE collaboration.

In Fig. 5.4 we show a closer investigation of the D meson nuclear modification factor. The impact of the nuclear shadowing in the initial production of the heavy quark and the contribution from the coalescence mechanism on the D meson $R_{\rm AA}$ can be clearly seen in our result. With the inclusion of the shadowing effect, we obtain a factor of four decrease in the D meson $R_{\rm AA}$ at low $p_{\rm T}$, while a mild increase is observed at high $p_{\rm T}$. This is due to the fact that the charm quark production is significantly suppressed at low $p_{\rm T}$ and slightly enhanced at high $p_{\rm T}$ in Pb-Pb collisions relative to binary collision number scaled proton-proton collisions, as shown in Fig. 2.5(a) [2]. Meanwhile, we also observe that the fragmentation mechanism alone is sufficient to describe heavy quark hadronization above 8 GeV. In the low and intermediate $p_{\rm T}$ region, however, the recombination of heavy quarks and light thermal partons becomes important, due to the coalescence mechanism converting low $p_{\rm T}$

[2] Note that this suppression at low $p_{\rm T}$ resulting from the nuclear shadowing effect might be reduced by half if one adopts a newer tuning of the parametrization of the parton distribution function (EPS09). However, the effect still remains significant.

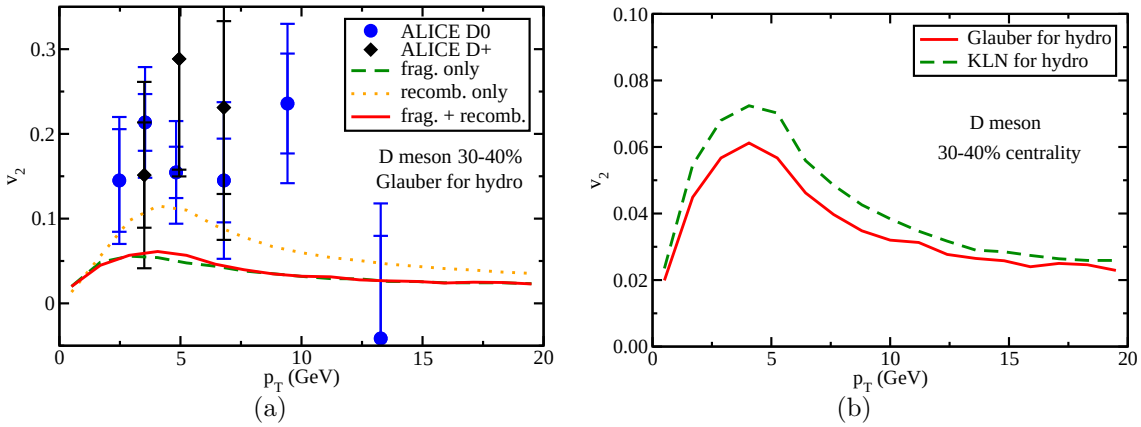

FIGURE 5.5: The elliptic flow v_2 of D mesons at the LHC: (a) compares between different hadronization mechanisms and (b) compares between different initial conditions of the hydrodynamic medium.

heavy quarks into medium $p_{\rm T}$ hadrons by combining with a thermal parton from the QGP, and therefore decreasing the D meson $R_{\rm AA}$ near zero $p_{\rm T}$ but significantly increasing it in the intermediate regime (2-5 GeV).

In Fig. 5.5, we show our calculation of the D meson elliptic flow v_2. Contributions from different hadronization mechanisms are presented for comparison in Fig. 5.5(a). For the pure fragmentation scenario, we set the Wigner function f^W to be 0 to remove hadronization through coalescence, while f^W is taken as 1 for the pure recombination scenario. One sees that the recombination mechanism results in a much larger D meson v_2 than fragmentation due to the fact that the recombination process brings the anisotropic flow of light quarks from the hydrodynamic medium into the formation of heavy flavor hadrons. Note that in our result, we do not observe a significant increase of the D meson v_2 when combining fragmentation and recombination mechanisms. This may be due to a combinational effect of the initial parton spectra, the momentum dependence of the Wigner function, and the radial flow developed in the QGP medium.

While our calculation seems to underestimate the data of the D meson elliptic flow v_2, many uncertainties still exist. For instance, as discussed in Sec.3.3, if we

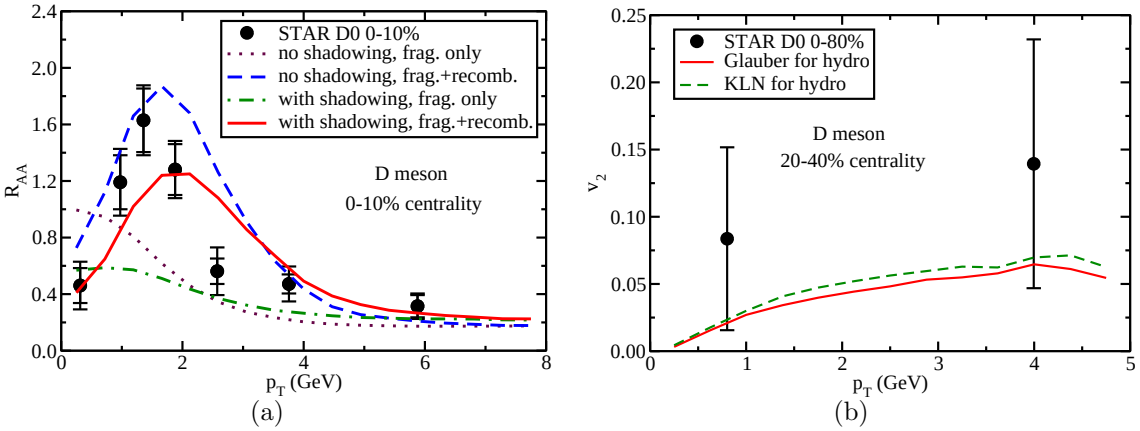

FIGURE 5.6: The D meson $R_{\rm AA}$ (a) and v_2 (b) at RHIC.

adopt the KLN initial condition for the hydrodynamical evolution, we would obtain a larger eccentricity of the QGP profile and therefore a larger v_2 for D meson as well. In Fig. 5.5(b), we find an increase of the D meson flow by 25% when switching from the Glauber to the KLN initial condition of the hydrodynamic background. Note that changing initial conditions with a larger eccentricity does not affect the overall suppression of D mesons in the central collision region. In addition, in this calculation, the heavy flavor evolution ceases after the QGP hadronizes and heavy mesons are formed; the subsequent hadronic interactions between D mesons and the hadron gas have not been included yet. This process will be discussed in the next chapter.

In Fig. 5.6 we present our results of the D meson $R_{\rm AA}$ and v_2 at RHIC (Au-Au collisions at $\sqrt{s_{NN}} = 200$ GeV) in comparison with the data measured by the STAR collaboration. We observe that the influence of the nuclear shadowing at RHIC is not as significant as at LHC. The coalescence mechanism, on the other hand, is found to be more important in the low $p_{\rm T}$ regime measured at RHIC; one observes the "bump" structure of the D meson suppression after the incorporation of recombination mechanism in the hadronization process. Our result is consistent with data from the STAR Collaboration. The results of the D meson v_2 at RHIC are shown in

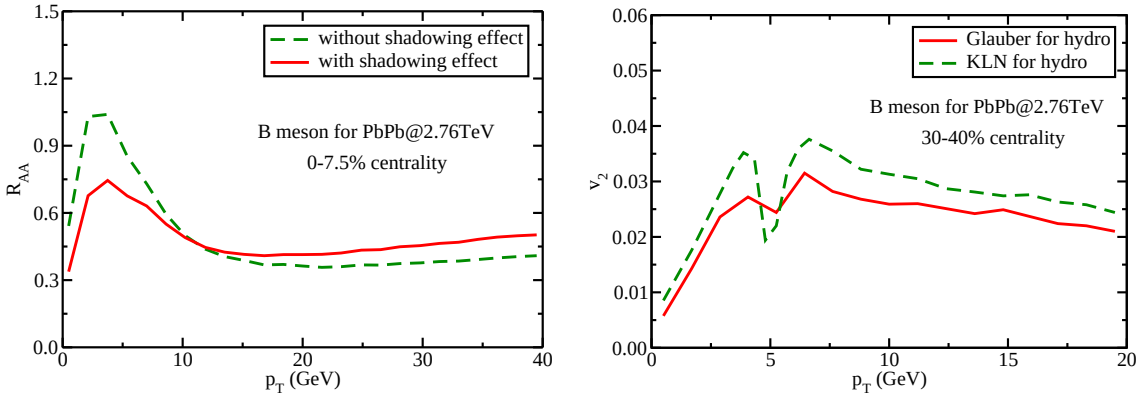

FIGURE 5.7: Predictions of the B meson $R_{\rm AA}$ (a) and v_2 (b) for 2.76 TeV Pb-Pb collisions.

Fig. 5.6(b), where the the Glauber and the KLN hydrodynamic initial conditions are compared. Overall, our model provides descriptions of the D meson nuclear modification and elliptic flow that are consistent with the RHIC observations after we take into account the nuclear shadowing effect in the initial heavy quark production, incorporate gluon radiation and elastic collisions for heavy quark evolution and energy loss inside the QGP, and utilize a hybrid model of fragmentation and recombination for the heavy quark hadronization process.

5.4.2 Predictions for the Future Observations

In Fig. 5.7 and Fig. 5.8, we provide predictions for the nuclear modification factor and the elliptic flow of B mesons at LHC and RHIC energies. In these two figures, we have included both fragmentation and coalescence mechanisms for bottom quark hadronization. The effects of the nuclear shadowing and different hydrodynamic initial conditions on the final B meson $R_{\rm AA}$ and v_2 are shown for comparison. Due to the larger mass of the bottom quark than that of the charm quark, the coalescence mechanism plays a more crucial role in its hadronization process. This can be clearly seen in Fig. 5.1 and Fig. 5.2: bottom quarks have much larger recombination probability over a wider $p_{\rm T}$ range than charm quarks. As a result, we observe a

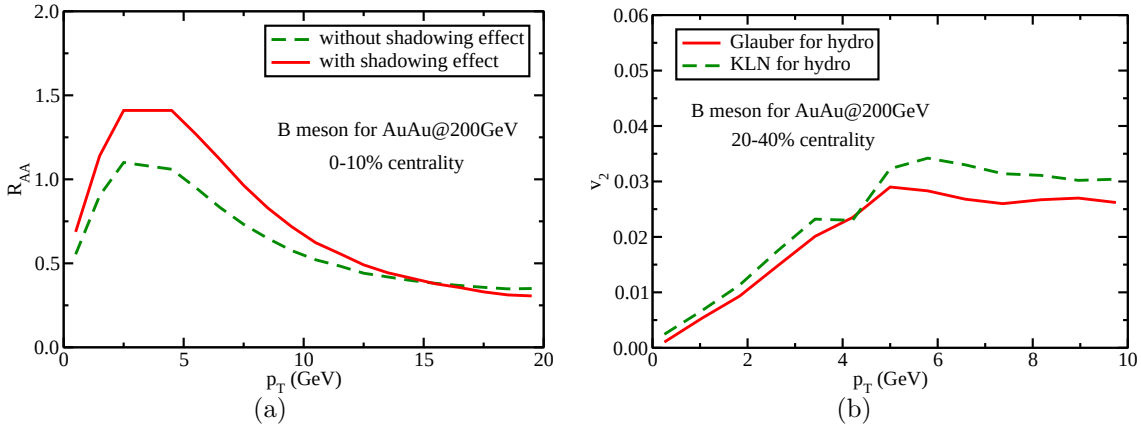

FIGURE 5.8: Predictions of the B meson $R_{\rm AA}$ (a) and v_2 (b) for 200 GeV Au-Au collisions.

"bump" structure of the B meson $R_{\rm AA}$ for both LHC and RHIC. The slight "dips" in the B meson v_2 around 5 GeV in Fig. 5.7(b) and Fig. 5.8(b) result from the transition from the regime where collisional energy loss dominates the heavy quark motion to the regime where radiative energy loss takes over. For more details about the relative contributions from different energy loss mechanisms to v_2, one may refer to our previous calculation in Ref. [134].

In Fig.5.9, we show our predictions of the D meson $R_{\rm AA}$ for 30-50% Pb-Pb collisions at the LHC energy, in which the in-plane and the out-of-plane results are compared. Here, "in-plane" is defined as the region within $\pm\pi/4$ from the event plane, while "out-of-plane" is the remaining region. We observe that because of a longer path length traversed by heavy quarks in the out-of-plane region, D mesons display a larger suppression, i.e., a smaller $R_{\rm AA}$ than those in the in-plane region.

Finally, we also provide predictions for $R_{\rm AA}$ and v_2 of non-photonic electrons emitted in heavy meson decays for 62.4 GeV Au-Au collisions at RHIC. As discussed in Sec.3.3.3, large uncertainties remaining in the ratio between the initial production rates of charm and bottom quarks may lead to significant uncertainties in the final state spectra of their decay electrons. Here, we show results both for the

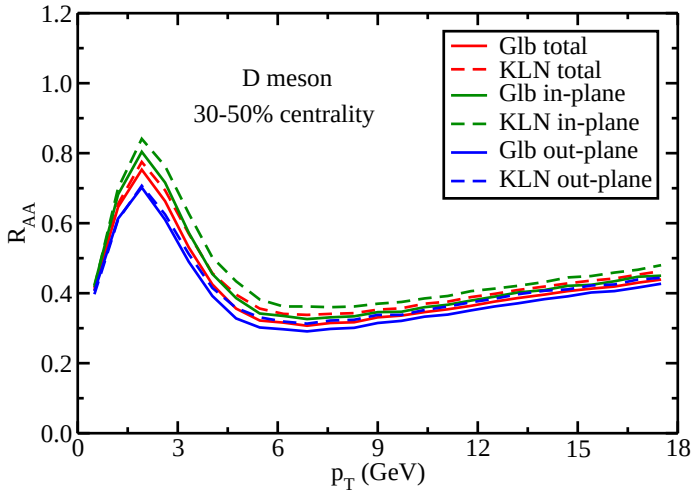

FIGURE 5.9: Predictions of the D meson $R_{\rm AA}$ for 30-50% 2.76 TeV Pb-Pb collisions, compared between the in-plane and the out-of-plane results.

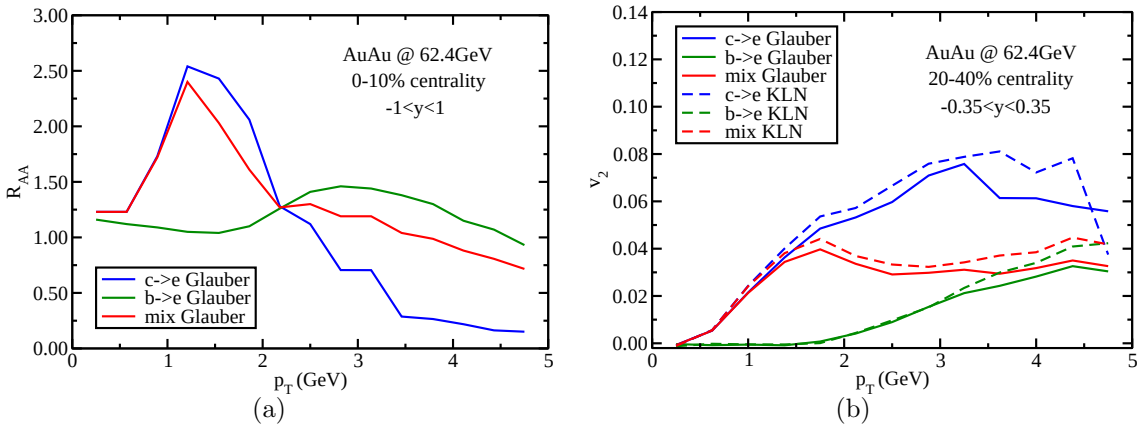

FIGURE 5.10: Predictions of $R_{\rm AA}$ (a) and v_2 (b) of heavy flavor decay electrons for 62.4 GeV Au-Au collisions at RHIC.

combined electrons and separately for c-decay and b-decay electrons. When mixing electrons from the two sources, we use the production ratio between charm and bottom quarks directly given by the leading-order pQCD calculation as described in Chapter 2, which is $b/c \approx 0.004$ at 62.4 GeV. As shown by Fig.5.10(a), at this relatively low energy of Au-Au collisions, no suppression of b-decay electrons is observed below 5 GeV. Instead, an enhancement due to the initial cold nuclear matter effect

may exist. Although charm quarks are still suppressed, no significant suppression would be observed for the mixed electrons if the production rate above is correct. On the other hand, in Fig.5.10(b), we see that the collective flow of non-photonic electrons still exists at this collisional energy. These calculations were performed one year ago and have recently been confirmed by experimental results of the PHENIX collaboration [113].

To conclude this section, we have combined our models of the heavy flavor initial production, the in-medium scattering and gluon radiation, and the hybrid fragmentation plus coalescence hadronization. Within this numerical framework, we have studied the evolution of heavy flavor produced in relativistic heavy-ion collisions and have calculated their suppression and flow that are observed at RHIC and LHC. Our calculations indicate that medium-induced gluon radiation contributes significantly to heavy quark energy loss especially at high energies. The nuclear shadowing has been shown to suppress the D meson $R_{\rm AA}$ at low $p_{\rm T}$ and enhance it at high $p_{\rm T}$. The heavy-light quark coalescence is found to increase both $R_{\rm AA}$ and v_2 of D mesons at intermediate $p_{\rm T}$. The effect of different choices of hydrodynamic initial conditions on the final D and B meson elliptic flow has also been investigated. Utilizing our improved Langevin approach together with a hybrid model for heavy quark hadronization, we have presented the nuclear modification and the elliptic flow of D mesons, which are consistent with the experimental measurements at both LHC and RHIC. Predictions for the future measurements have also been provided, such as the B meson suppression and flow at both RHIC and LHC energies, the D meson $R_{\rm AA}$ for the in-plane and the out-of-plane regions for 30-50% Pb-Pb collisions at $\sqrt{s_{NN}} = 2.76$ TeV, and the medium modification of non-photonic electrons produced at 62.4 GeV Au-Au collisions.

6

Hadronic Interaction of Heavy Mesons inside the Hadron Gas

At this moment, with the combination of the Cold Nuclear Matter Effect in the initial production of heavy quarks, collisional plus radiative energy loss during their transport inside the QGP matter, and a hybrid fragmentation plus coalescence model to describe their hadronization process, we are already able to provide good descriptions of D meson suppression and collective flow observed in relativistic heavy-ion collisions at both RHIC and LHC. Nevertheless, in a realistic scenario, the strong interactions do not cease immediately when the temperature of the system drops below $T_{\rm c}$. Instead, the hadrons that are regenerated from the color-deconfined state of quarks and gluons will continue scattering off each other for approximately another10 fm/c until this hadron gas is so dilute that no more interactions occur. In this chapter, in order to complete our understanding of the full time evolution of heavy flavor dynamics in heavy-ion collisions, the hadronic interactions between open heavy flavor mesons formed from heavy quarks and soft hadrons produced by the QGP matter will be studied in the framework of the Ultra-relativistic Quantum Molecular Dynamics (UrQMD) model. We will demonstrate that such interactions in

the afterburner phase further suppress D meson $R_{\rm AA}$ in the high transverse momentum regime and enhances its v_2. With the incorporation of this additional process into our numerical framework, we refit our theoretical calculations to the experimental data and extract the gluon transport coefficient $\hat{q}$ of the QGP matter with a value of around 2.6 GeV^2/fm at the LHC energy. This is consistent with the values constrained by a recent work [95] that uses a systematic comparison between various energy loss formalisms of light partons.

This chapter is organized as follows. In Sec.6.1, we will discuss about how we apply the UrQMD model to study heavy meson interaction with the hadron gas after the QGP freezes out – including the formation of the hadron gas based on the Cooper-Frye formula, a brief review of the UrQMD model and how the charm meson scattering cross sections are introduced into the UrQMD model. In Sec.6.2, we will present our numerical results of D meson suppression and flow after the inclusion of the UrQMD model into our framework and investigate how the hadronic interaction in the afterburner stage further affects the heavy meson spectra one observes. Finally in Sec.6.3, we go beyond the current widely used heavy flavor observables ($R_{\rm AA}$ and v_2) and apply our updated framework of heavy flavor dynamics to explore a new set of quantities – heavy-flavor-tagged angular correlation functions – and find them to be potential candidates for distinguishing different energy loss mechanisms of heavy quarks inside a QGP.

6.1 D Meson Transport in a Hadron Gas

6.1.1 Formation of the Hadron Gas – The Cooper-Frye Formula

In order to describe the interactions between heavy mesons with the soft hadron gas in the following subsections, it is first necessary to understand how the hadron gas forms from the QGP matter. One general approach to obtain the hadron distributions is applying the Cooper-Frye formula [28, 207] at the hypersurface of the chemical

freeze-out, i.e., at T_c.

To determine the total number of particles of species i (N_i) produced by the decaying QGP, we need to define a 3-dimensional hypersurface $\Sigma(x)$ in the 4-dimensional space-time along which the QGP decays. For instance, one may take a picture of the system at time t and count N_i in the frozen 3-dimensional space we obtain. However, a real detector does not perform in the way. An ideal detector would be a closed 2-dimensional surface (e.g. a sphere) that covers the regions of our heavy-ion collisions. In this case, different final-state hadrons reach the detector at different times based on their production space-time and velocity, and one may perform the counting from $t = -\infty$ to ∞ and collect the information of all produced hadrons. Note that in this scenario we have defined the hypersurface as a 2-dimensional space that extends over all possible time – still 3-dimensional. Therefore, we see that it is possible to choose different hypersurfaces for the counting as long as they entirely separate the collision point from the future light cone.

Let us first define the number current density of hadron i as

$$j_i^\mu(x) = \int \frac{d^3p}{(2\pi)^3 E} p^\mu f_i(x,p), \tag{6.1}$$

in which $f_i(x,p)$ represents the phase space distribution of hadron i. Then, we can calculate the total particle number by integrating the normal component of this current over a chosen hypersurface $\Sigma(x)$:

$$N_i = \int_\Sigma d^3\sigma_\mu(x)\, j_i^\mu(x) = \int_\Sigma d^3\sigma_\mu(x) \left[\frac{1}{(2\pi)^3}\int \frac{d^3p}{E}\, p^\mu\, f_i(x,p)\right]. \tag{6.2}$$

Here, $d^3\sigma_\mu(x)$ is an infinitesimal element of $\Sigma(x)$ with its direction perpendicular to the hypersurface. If we have two different hypersurfaces Σ_1 and Σ_2 with their sum $\Sigma_1 - \Sigma_2$ closing a certain region of the 4-dimensional space-time, then according to

the Gauss theorem and the conservation of current $\partial_\mu j_i^\mu(x) = 0$, we have

$$\int_{\Sigma_1 - \Sigma_2} d^3\sigma_\mu(x)\, j_i^\mu(x) = \int_V d^4x \partial_\mu j_i^\mu(x) = 0. \tag{6.3}$$

Note that in this specific case, the relative minus sign between Σ_1 and Σ_2 results from the positive direction of a hypersurface being defined as pointing outward from the region containing the collision point and V represents the 4-dimensional region closed by the two hypersurfaces. And Eq.(6.3) indicates that $\int_{\Sigma_1} d^3\sigma_\mu(x)\, j_i^\mu(x) = \int_{\Sigma_2} d^3\sigma_\mu(x)\, j_i^\mu(x)$, i.e., the number of hadrons is independent of the choice of the hypersurface as long as the multiplicity of various particle species is conserved during the evolution. However, since hydrodynamics is not a good approximation of the system below T_c where the mean free path is no longer small enough, we calculate the process of hadron production at the hypersurface of chemical freeze-out Σ_f, and then apply the UrQMD model (discussed below) for the subsequent hadronic evolution.

The differential form of Eq.(6.2) reads

$$E\frac{dN_i}{d^3p} = \frac{dN_i}{dy p_\mathrm{T} dp_\mathrm{T} d\phi_p} = \frac{dN_i}{dy m_\mathrm{T} dm_\mathrm{T} d\phi_p} = \frac{1}{(2\pi)^3}\int_{\Sigma_\mathrm{f}} p^\mu d^3\sigma_\mu(x)\, f_i(x,p). \tag{6.4}$$

This is known as the Cooper-Frye formula. The following definitions and relative relations between different variables have been used in Eq.(6.4):

$$m_\mathrm{T} \equiv \sqrt{p_\mathrm{T}^2 + m^2}, \quad y \equiv \frac{1}{2}\ln\frac{E+p_z}{E-p_z}, \quad E = m_\mathrm{T}\cosh y, \quad p_z = m_\mathrm{T}\sinh y. \tag{6.5}$$

Three pieces of information are required for the evaluation of this Cooper-Frye integral: (1) the freeze-out hypersurface Σ_f, (2) the phase distribution of hadron $f_i(x,p)$, and (3) how to evaluate the scalar product of $p^\mu d\sigma_\mu(x)$.

To obtain the freeze-out hypersurface Σ_f, one follows the hydrodynamical evolution of the medium background and records the proper time $\tau(\equiv\sqrt{t^2-z^2})$ of each

fluid cell when its local temperature drops below T_c. Thus we obtain $\tau_f = \tau_f(x, y, \eta_s)$ in which the space-time rapidity η_s is defined as $\eta_s \equiv \frac{1}{2}\ln[(t+z)/(t-z)]$ (similar to Eq.(6.5), we have the inverse transformations $t = \tau\cosh\eta_s$ and $z = \tau\sinh\eta_s$ here). This reduces the 4-dimensional space-time to the 3-dimensional hypersurface Σ_f we seek. Note that in principle, apart from these hadrons emitted from the freeze-out hypersurface, there also exist "colder" hadrons produced directly from the pre-equilibrium stage of the heavy-ion collisions without experiencing the QGP evolution. These hadrons mainly form from the "corona" regime of the overlapping region of the two colliding nuclei and their contribution to the total multiplicity of the final state can be considered small especially in the mid-rapidity region. More discussions about these corona hadrons can be found in Ref. [37].

In general, for a particle residing in a thermal reservoir, the phase space distribution can be written in terms of:

$$f_i(x,p) = f_{i,\mathrm{eq}} + \delta f_i(x,p). \tag{6.6}$$

Here, $f_{i,\mathrm{eq}}$ represents the distribution function for a set of particles in local thermal equilibrium

$$f_{i,\mathrm{eq}}(x,p) = \frac{g_i}{e^{[p\cdot u(x)-\mu_i(x)]/T(x)} \pm 1} = g_i \sum_{n=1}^{\infty} (\mp)^{n+1}\, e^{-n[p\cdot u(x)-\mu_i(x)]/T(x)}, \tag{6.7}$$

in which g_i denotes the degeneracy of spin, color, flavor, etc., μ_i is the chemical potential of hadron i, $T(x)$ and $u^\mu(x)$ represent the local temperature and the 4-velocity of the fluid cell, and ± 1 in the denominator accounts for the proper quantum statistics – upper (lower) sign for fermions (bosons). In a non-perfect fluid, i.e., a viscous hydrodynamic medium, the coupling strength is not infinitely large and a finite relaxation time is required for the system to go back to local thermal equilibrium during its expansion. This leads to a deviation $\delta f_i(x,p)$ from the equilibrium limit

in the hadron distribution function as shown in Eq.(6.6). The exact relation between viscosity and δf requires an approximate solution of the Boltzmann equation. There are two forms of δf for the case where the bulk viscosity does not contribute and only the shear stress tensor ($\pi^{\mu\nu}$) is non-zero (a more general solution is an open topic of research itself at this moment) [37]. One of them reads

$$\delta f(x,p) = f_{\rm eq}(x,p)\left[1 \pm f_{\rm eq}(x,p)\right] \cdot \frac{1}{2}\frac{\pi^{\mu\nu}(x)\hat{p}_\mu \hat{p}_\nu}{e+p}\chi\left(\frac{p}{T}\right), \tag{6.8}$$

in which $\hat{p}^\mu = p^\mu/p$, with $p = \sqrt{-p_\mu \Delta^{\mu\nu} p_\nu}$ ($\Delta^{\mu\nu} \equiv g^{\mu\nu} - u^\mu u^\nu$) being the magnitude of the spatial momentum in the local rest frame of the fluid cell. And

$$\chi\left(\frac{p}{T}\right) = \left(\frac{p}{T}\right)^\alpha, \quad (1 \le \alpha \le 2), \tag{6.9}$$

with the power α depending on the details of the collision term and the ansatz used for solving the Boltzmann equation. The other form of δf reads [208]

$$\delta f(x,p) = f_{\rm eq}(x,p)\left[1 \pm f_{\rm eq}(x,p)\right] \cdot \frac{1}{2}\frac{\pi^{\mu\nu}(x)p_\mu p_\nu}{\beta_\pi(T)T(x)(p\cdot u)}\left[1 + \mathcal{O}(\pi^{\mu\nu})\right], \tag{6.10}$$

in which $\beta_\pi(T)$ is a thermodynamic integral that can be reduced to $\beta_\pi = (e+p)/s$ for massless particles. Note that at large p, Eq.(6.10) is linear with respect to p.

In the end, the only piece left in calculating the Cooper-Frye integral Eq.(6.4) is the evaluation of the infinitesimal element $p^\mu d\sigma_\mu(x)$. In general, any 3-dimensional space can be parametrized using three locally orthogonal variables u, v, w and then the points on the surface $\Sigma(x)$ can be represented by $\Sigma^\mu(u,v,w)$. With this setup, the normal vector on the curved manifold of $\Sigma(x)$ can be calculated with the following formula known from the theory of general relativity:

$$d^3\sigma_\mu(u,v,w) = -\epsilon_{\mu\nu\lambda\rho}\frac{\partial\sigma^\nu}{\partial u}\frac{\partial\sigma^\lambda}{\partial v}\frac{\partial\sigma^\rho}{\partial w}dudvdw, \tag{6.11}$$

where $\epsilon_{\mu\nu\lambda\rho}$ is the completely antisymmetric Levi-Civita tensor in a 4-dimensional space with $\epsilon^{0123} = -\epsilon_{0123} = 1$. As discussed earlier, the (τ, x, y, η_s) coordinate is adopted for the hydrodynamical evolution and we choose (x, y, η_s) as the three orthogonal components to represent the freeze-out hypersurface. $\Sigma(t, x, y, z)$ in the Minkowski space is then represented as $\Sigma(\tau(x, y, \eta_s)\cosh\eta_s, x, y, \tau(x, y, \eta_s)\cosh\eta_s)$. With the help of Eq.(6.11), we find

$$d^3\sigma_\mu(\vec{r}_{\rm T}, \eta_s) = \left(\cosh\eta_s + \frac{1}{\tau}\frac{\partial\tau}{\partial\eta_s}\sinh\eta_s, -\frac{\partial\tau}{\partial x}, -\frac{\partial\tau}{\partial y}, -\sinh\eta_s - \frac{1}{\tau}\frac{\partial\tau}{\partial\eta_s}\cosh\eta_s\right) \times \tau(\vec{r}_{\rm T}, \eta_s)d\eta_s d^2r_{\rm T} \tag{6.12}$$

in which we have represented the transverse components (x, y) with $r_{\rm T}$. Recall that with $p^\mu = (m_{\rm T}\cosh y, p_x, p_y, m_{\rm T}\sinh y)$, we have

$$\begin{aligned} p^\mu d^3\sigma_\mu =& \Big(m_{\rm T}\cosh y\cosh\eta_s + \frac{m_{\rm T}}{\tau}\frac{\partial\tau}{\partial\eta_s}\cosh y\sinh\eta_s - p_x\frac{\partial\tau}{\partial x} - p_y\frac{\partial\tau}{\partial y} \\ & - m_{\rm T}\sinh y\sinh\eta_s - \frac{m_{\rm T}}{\tau}\frac{\partial\tau}{\partial\eta_s}\sinh y\cosh\eta_s\Big) \times \tau(\vec{r}_{\rm T}, \eta_s)d\eta_s d^2r_{\rm T} \\ =& \left[m_{\rm T}\cosh(y-\eta_s) - \frac{m_{\rm T}}{\tau}\frac{\partial\tau}{\partial\eta_s}\sinh(y-\eta_s) - \vec{p}_{\rm T}\cdot\bigtriangledown_{\rm T}\tau(\vec{r}_{\rm T}, \eta_s)\right] \\ & \times \tau(\vec{r}_{\rm T}, \eta_s)d\eta_s d^2r_{\rm T}. \end{aligned} \tag{6.13}$$

If we assume the hydrodynamic medium is boost-invariant in the longitudinal direction, i.e., the longitudinal proper time τ is independent of the space-time rapidity η_s, Eq.(6.13) can be simplified to

$$p^\mu d^3\sigma_\mu(\vec{r}_{\rm T}) = \left[m_{\rm T}\cosh(y-\eta_s) - \vec{p}_{\rm T}\cdot\bigtriangledown_{\rm T}\tau(\vec{r}_{\rm T})\right]\tau(\vec{r}_{\rm T})d\eta_s d^2r_{\rm T}. \tag{6.14}$$

With the above evaluations of the freeze out hypersurface $\Sigma_{\rm f}(x)$, the phase space distribution of formed hadrons $f_i(x, p)$ and the infinitesimal integral element $p^\mu d\sigma_\mu(x)$, one is able to calculate the hadron spectra produced from the QGP matter according to the Cooper-Frye formula Eq.(6.4). This process is incorporated in

almost all of the current computational codes of hydrodynamics. In our calculation, we use the numerical tool "iSS" – developed by the Ohio State University Group together with their hydrodynamic model [38] – to sample the hadron distribution at QGP freeze-out.

6.1.2 Application of the UrQMD Model to Hadronic Scatterings

In Chapter 5, we discussed the formation of open heavy mesons from heavy quarks, and in the previous subsection, the production of soft hadrons from a decaying QGP was illustrated. Now we feed all these hadrons together into the UrQMD model to simulate the subsequent processes of hadronic re-scattering.

The Ultra-relativistic Quantum Molecular Dynamics (UrQMD) model [36] is a microscopic model that simulates many body interactions in heavy-ion reactions on an event by event basis. It may either start the simulation from the two colliding nuclei or import the phase space distributions of a list of hadrons as an initial condition and simulate the subsequent interactions. We utilize the latter process for our purpose of studying D meson evolution inside a hadron gas.

Various baryons species (including nucleon, delta and hyperon resonances with masses up to 2.25 GeV) and meson species (including strange meson resonances) and their corresponding anti-particles are included in the collision term of the UrQMD model. New states can be produced during interactions via string decays, s-channel collisions or resonance decays. The required cross sections are parametrized or tabulated either according to existing experimental data or available theoretical calculations. We will discuss the scattering cross sections of charm mesons separately in the next subsection, and detailed information about light hadron interactions can be found in the original literature [36].

In UrQMD, the collisions between hadrons are performed with a stochastic method. At the beginning of each time step, the relative distance d_{trans} between each pair of

particles is calculated. This relative distance $d_{\rm trans}$ is defined as the closest distance the selected pair of particles approach each other (in the local rest frame of the two particles) if they stream freely. If this closest distance satisfies the semi-classical criterion $d_{\rm trans} \leq d_0 \equiv \sqrt{\sigma_{\rm tot}/\pi}$, then a scattering may happen. Here, $\sigma_{\rm tot}$ is the total scattering cross section which depends on the species and the center of mass energy $\sqrt{s}$ of the two colliding particles. UrQMD scans all possible two-particle scatterings and orders the qualified pairs according to the collision times. Then the scattering between the first pair (with the shortest colliding time Δt) is selected to take place while all the other particles stream freely during this Δt. For the chosen scattering, the species of the daughter particles are determined according the relative branching ratio of the scattering process. UrQMD then samples the scattering angles of the final states either (for most elastic scatterings) according to an analytical expression [209, 210] or (for inelastic processes like annihilations and decays) by empirical interpolation between forward peaked, isotropic scattering and other parametrizations. This scheme is repeated for subsequent scatterings until the hadron gas is so dilute that none of the particle pairs satisfies the scattering criterion $d_{\rm trans} \leq d_0$ and therefore all interactions cease – this is known as the "kinetic freeze-out".

6.1.3 Scattering Cross Sections of Charm Mesons in a Hadron Gas

One of the most important ingredients of the UrQMD model are the hadronic scattering cross sections. To simulate the interactions of D mesons with the hadron gas, we introduce the scattering cross sections of charm mesons with pions and rho mesons calculated in Ref. [143] into UrQMD. In this reference paper, to describe a hadronic system composed of 4 quark flavors (u, d, s, c), the author starts with the following free Lagrangian for pseudoscalar and vector mesons

$$\mathcal{L}_0 = \mathrm{Tr}\left(\partial_\mu P^\dagger \partial^\mu P\right) - \frac{1}{2}\mathrm{Tr}\left(F^\dagger_{\mu\nu} F^{\mu\nu}\right), \tag{6.15}$$

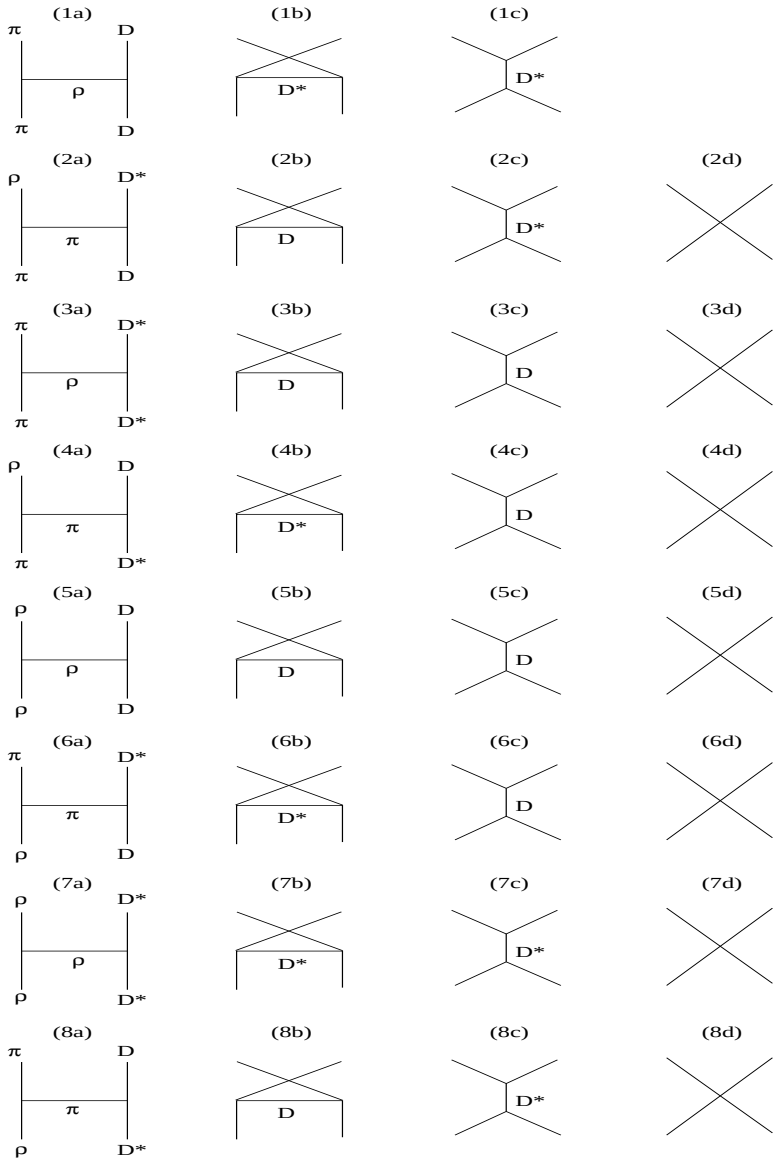

FIGURE 6.1: Diagrams for charm meson scatterings with π and ρ mesons: the numbers represents different scattering processes while the Roman letters distinguishes between different amplitudes in a given process. This figure is taken from Ref. [143].

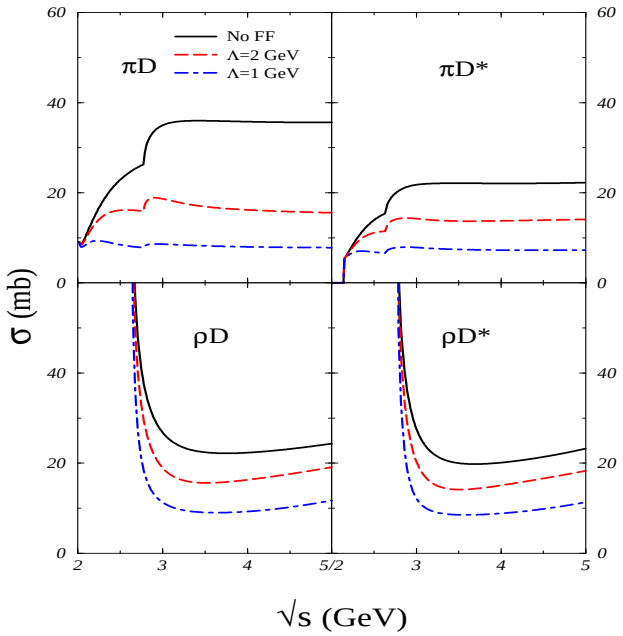

FIGURE 6.2: Total cross sections of charm meson scatterings with π and ρ mesons, compared between different form factors. This figure is taken from Ref. [143].

in which $F_{\mu\nu} \equiv \partial_\mu V_\nu - \partial_\nu V_\mu$, and P and V are the 4×4 matrices for pseudoscalar and vector mesons in SU(4) respectively. With the introduction of the standard minimum substitution

$$\partial_\mu P \to \mathcal{D}_\mu P = \partial_\mu P - \frac{ig}{2}\left[V_\mu, P\right], \tag{6.16}$$

$$F_{\mu\nu} \to \partial_\mu V_\nu - \partial_\nu V_\mu - \frac{ig}{2}\left[V_\mu, V_\nu\right], \tag{6.17}$$

one obtains the Lagrangian for interacting hadrons as follows:

$$\begin{aligned}\mathcal{L} = \mathcal{L}_0 &+ ig\mathrm{Tr}\left(\partial^\mu P\left[P, V_\mu\right]\right) - \frac{g^2}{4}\mathrm{Tr}\left(\left[P, V_\mu\right]^2\right) \\ &+ ig\mathrm{Tr}\left(\partial^\mu V^\nu\left[V_\mu, V_\nu\right]\right) + \frac{g^2}{8}\mathrm{Tr}\left(\left[V_\mu, V_\nu\right]^2\right).\end{aligned} \tag{6.18}$$

This Lagrangian implies 8 processes of charm meson scatterings with π and ρ mesons – $\pi D \leftrightarrow \rho D^*$, $\pi D \to \pi D$, $\pi D^* \to \pi D^*$, $\pi D^* \leftrightarrow \rho D$, $\rho D \to \rho D$, $\rho D^* \to \rho D^*$ – which can be represented by diagrams in Fig.6.1.

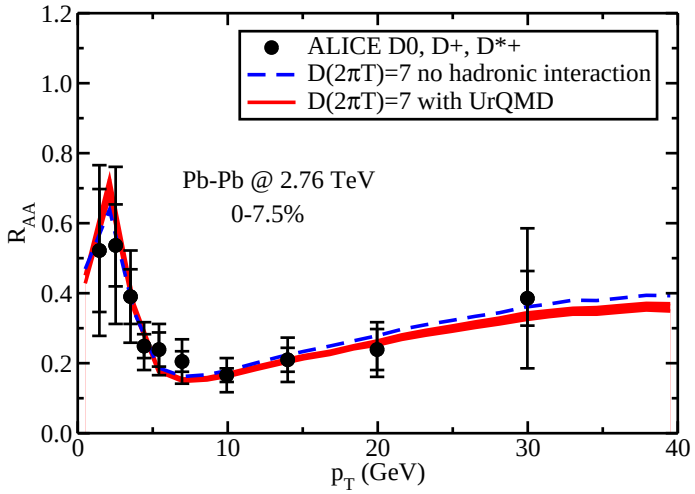

FIGURE 6.3: Effect of hadronic interaction on the D meson suppression in central Pb-Pb collisions.

One may refer to the original work [143] for details regarding the calculation of these diagrams. Here in Fig.6.2 we directly cite the corresponding numerical results for the total cross sections of charm meson scattering with π and ρ mesons as functions of the center of mass energy $\sqrt{s}$. Note that in Fig.6.2, different choices of the cutoff parameter Λ in the form factor for the hadron structure are compared, which significantly affect the scattering cross sections of charm mesons. This will be treated as a systematic uncertainty in our later UrQMD simulation.

6.2 Effects of Hadronic Scattering on D Meson Suppression and Flow

In this section, we apply the above mentioned UrQMD model to simulate the hadronic interactions between D mesons and the hadron gas and explore how these scatterings may further affect the D meson spectra that we observe at LHC and RHIC.

In Fig.6.3, we investigate how the hadronic interactions further affect the D meson $R_{\rm AA}$. We observe that due to additional energy loss that the D meson suffers inside the hadron gas, its $R_{\rm AA}$ is further decreased at large $p_{\rm T}$. Consequently, due

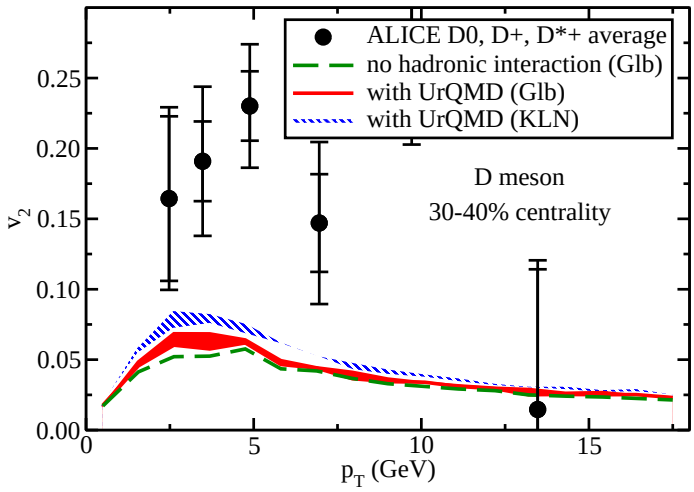

FIGURE 6.4: Effect of hadronic interaction on the collective flow of D mesons observed at LHC.

to the conservation of the number of charmed hadrons, the D meson $R_{\rm AA}$ is slightly enhanced at low $p_{\rm T}$ after the UrQMD evolution. As discussed in Sec.6.1.3, we show an error band in Fig.6.3 for our theoretical calculation which signifies the uncertainty in the choice of the cutoff parameter Λ of the hadron form factor. Note that starting from this point, our calculations adopt a new version of the EPS parametrizations of the nuclear shadowing effect in the initial state (EPS09), which reduces the amount of "shadowing" at low $p_{\rm T}$: this yields less suppression of $R_{\rm AA}$ compared to our earlier results presented in Sec.5.4. With our comprehensive framework that incorporates heavy flavor evolution in both QGP and hadronic phases, we provide good description of the D meson suppression as observed in Pb-Pb central collisions at LHC. By comparing with experimental data, we find the final spatial diffusion coefficient of heavy quarks in the QGP extracted from our model to be around $7/(2\pi T)$, which corresponds to a gluon transport coefficient $\hat{q}$ of around 2.6 GeV^2/fm. This is consistent with the constraints suggested in a recent work [95] by systematically comparing various energy loss formalisms of light partons.

Apart from $R_{\rm AA}$, another important observable for heavy mesons is its the collec-

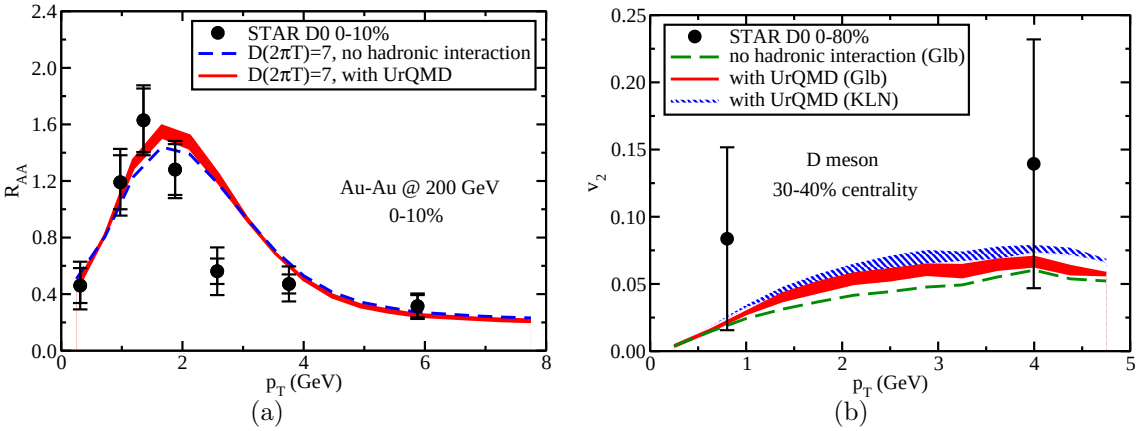

FIGURE 6.5: Comparison of the D meson $R_{\rm AA}$ (a) and v_2 (b) with RHIC data.

tive flow coefficient v_2. As displayed in Fig.6.4, additional scatterings of D mesons in an anisotropic hadron gas further enhance the v_2 value by over 30%. As already discussed in Sec.5.4, we also present here the difference between two hydrodynamic initial conditions. Since the KLN model provides a larger eccentricity of the initial entropy density profiles than the Glauber model, this may cause another 30% difference in the collective flow of heavy mesons after their evolutions inside the QGP and the hadron gas. However, after taking all effects into account, our calculation still underestimates the D meson v_2 compared to the latest ALICE data.

In Fig.6.5, we provide our calculations of D meson suppression and flow in Au-Au collisions at RHIC energy. Similar to the above LHC scenario, the hadronic interaction simulated with the UrQMD model suppresses D meson $R_{\rm AA}$ at large $p_{\rm T}$ and enhances its v_2. Our numerical results are consistent with the experimental data measured by the STAR collaboration.

Furthermore, in Fig.6.6 we provide D meson $R_{\rm AA}$ for different centrality regions as observed at RHIC. And we also calculate the integrated $R_{\rm AA}$ of D meson over given $p_{\rm T}$ regions as functions of the participant number in Fig.6.7. Due to a smaller geometric size and a shorter life time of the hot and dense nuclear matter created in more peripheral collisions, the D meson $R_{\rm AA}$ increases with larger centrality, or

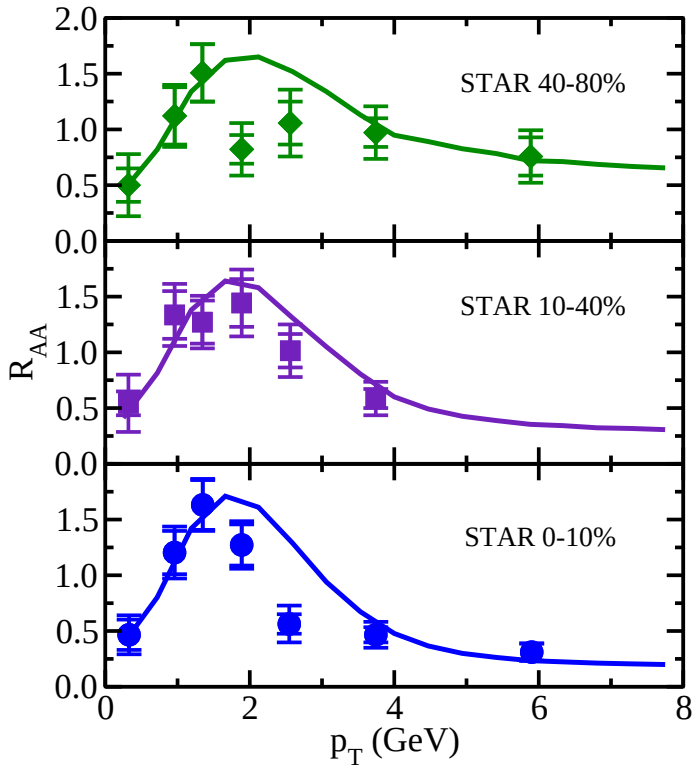

FIGURE 6.6: Comparison of the D meson $R_{\rm AA}$ with RHIC data for different centrality regions.

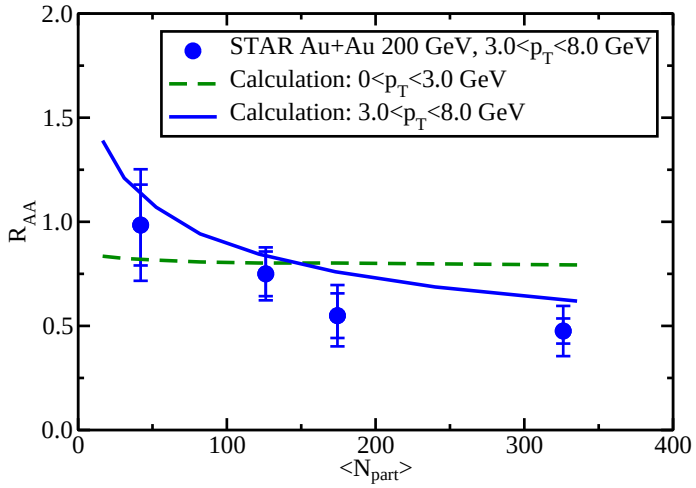

FIGURE 6.7: Dependence of the D meson $R_{\rm AA}$ on the participant number in Au-Au collisions at RHIC.

decreases with larger number of participant nucleons in nucleus-nucleus collisions. In Fig.6.6 and Fig.6.7, $\Lambda = 1$ is adopted for the hadron form factor. Our theoretical calculations are consistent with all the available data from RHIC and a prediction for the participant number dependence of the D meson $R_{\rm AA}$ is also provided for a smaller $p_{\rm T}$ region – the value of $R_{\rm AA}$ is expected to be larger in $0 < p_{\rm T} < 3$ GeV than in $3 < p_{\rm T} < 8$ GeV due to a combined effect of heavy flavor energy loss and the recombination mechanism in heavy meson formation.

6.3 Exploration of New Observables

We have developed a comprehensive framework to describe the full time evolution of heavy flavor produced in relativistic heavy-ion collisions, including its initial production, evolution in the QGP, hadronization and scattering inside the hadron gas. This newly developed tool provides heavy meson suppression and flow consistent with most existing experimental data. However, up till now, all of our study concentrates on the single particle spectra. On the other hand, exclusive spectra, or correlation functions may also be interesting and provide us with new insights regarding heavy flavor dynamics and the QGP properties. In this section, we will apply our updated model of heavy flavor dynamics to explore such heavy-flavor-tagged correlation functions and show that they are indeed useful new observable that helps us distinguish between different energy loss mechanisms of heavy quarks inside a QGP medium. Some of our preliminary results on this subject have been published in [211, 212, 213].

6.3.1 Motivation: Ambiguity of Single Particle Spectrum

As we discussed in Chapter 3 and Chapter 4, there are two major mechanisms for heavy quarks to lose energy in a hot and dense QCD medium – quasi-elastic scattering and gluon radiation. Although these two mechanisms possess different properties such as the length dependence of the amount of energy loss (see Sec.4.3.1), it may

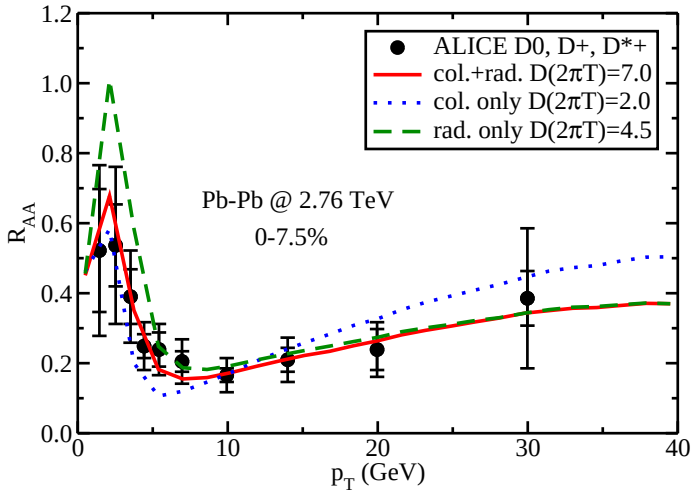

FIGURE 6.8: Fitting each energy loss mechanism of heavy quark to the observed D meson $R_{\rm AA}$ by tuning the transport coefficient.

not be easy to distinguish between them by using the single particle spectra alone.

As shown in Fig.6.8, one is able to fit experimental data of D meson $R_{\rm AA}$ with each energy loss mechanism alone by tuning the coupling strength. Although the combination of collisional and radiative energy loss provides the best $p_{\rm T}$ dependence of D meson suppression and leads to the most reasonable extraction of the gluon transport coefficient $\hat{q}$ according to Ref. [95], the collisional energy loss alone or gluon radiation alone may also fit the data within the current experimental uncertainty as long as one increases the $\hat{q}$, i.e., reduces the heavy quark diffusion coefficient D. Note that the microscopic structure of the heavy quark scattering cross section still remains largely unknown and different approaches – such as pQCD calculations [214], the heavy-light quark resonant scattering approach [215], AdS/CFT based calculations [216], lattice QCD calculations [217], etc. – may yield values of D varying from less than $D = 2/(2\pi T)$ to greater than $D = 5/(2\pi T)$. From this point of view, it is hard to determine which extraction in Fig.6.8 is correct and therefore which energy loss mechanism is dominant. The use of single particle spectra alone to study heavy

quark energy loss is therefore insufficient and this motivates the necessity to explore new observables that may provide better insight into the heavy flavor dynamics in heavy-ion collisions.

6.3.2 Angular Correlation Functions between Heavy Quark Pairs

In this subsection, we show that while it is difficult for single particle spectra to distinguish between different energy loss mechanisms of heavy quarks inside QGP, angular correlation functions related to heavy flavor pairs may serve as better and more discriminatory observables.

We start with the simplest scenario in which an leading order pQCD approximation is applied for the initial production of heavy flavor so that heavy quark Q and anti-heavy-quark $\bar{Q}$ paris are produced back to back with the same magnitude of momentum. After they travel through the medium, their momenta will change and the angle between them will no longer remains π. One may then measure the angular distribution and determine how much angular correlation between the $Q\bar{Q}$ pairs remains after they have traversed the medium.

In Fig.6.9, we examine how this angular de-correlation behavior depends on different energy loss mechanisms. While different energy loss mechanisms may independently describe the D meson $R_{\rm AA}$ for different values of the transport coefficients (Fig.6.8), they lead to significantly different angular correlation functions of the final state $c\bar{c}$ pair. As can be observed in Fig.6.9, pure radiative energy loss does not change the angular correlation function significantly after heavy quarks travel through the medium – the function still peaks around π. To the contrary, pure collisional energy loss leads to a peak around 0, indicating that low energy $c\bar{c}$ pair tends to move collinearly in the end because of the radial flow effect of the QGP medium – this is known as the "partonic wind effect" [218] and might be crucial for the enhancement of J/ψ regeneration in a QGP matter. Combining radiative and

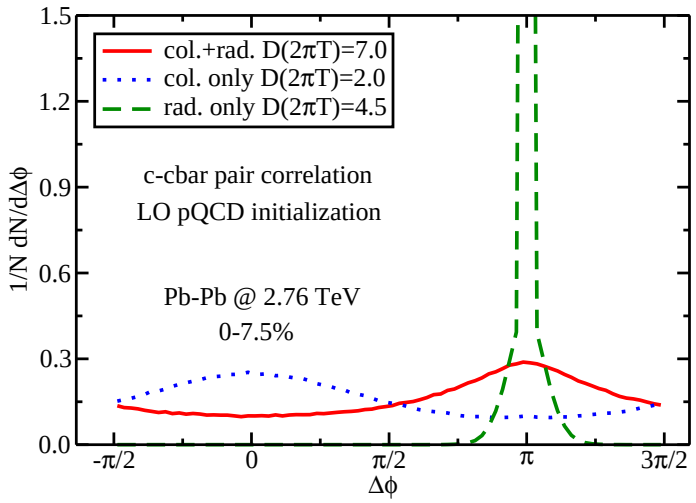

FIGURE 6.9: Comparison of the angular correlation functions of $c\bar{c}$ pair between different heavy quark energy loss mechanisms – back-to-back approximation for the heavy quark initial production.

collisional energy loss results in a correlation function in between the previous two situations. The different angular de-correlation behavior observed results from the qualitatively different momentum broadening mechanisms for heavy quarks caused by different energy loss mechanisms: medium-induced gluon radiation favors small angle emission but quasi-elastic scattering yields a fast isotropization of heavy quarks in the momentum space.

As the next step, we replace the leading order approximation of the initial production of heavy quark pairs by adopting an improved initialization method: a Monte-Carlo next-to-leading order (MCNLO) production of heavy quark pairs plus the Herwig vacuum radiation before they enter the QGP medium [132]. In this approach, the processes of gluon splitting and three particle production are incorporated and the p_{T} broadening of heavy quarks due to vacuum radiation is also considered. Therefore, as shown by the black dot-dashed curve in Fig.6.10, instead of the back-to-back picture, the angular correlation function of initial $c\bar{c}$ pairs is already double peaked around 0 and π in the mid-rapidity region ($1 < y < 1$). This provides a more realis-

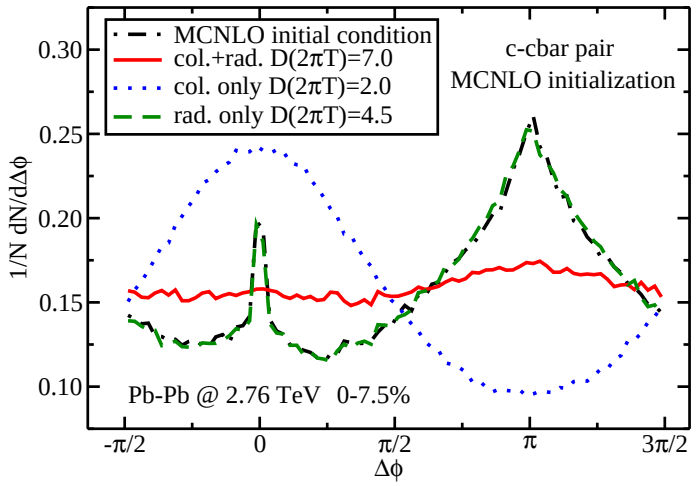

FIGURE 6.10: Comparison of the angular correlation function of $c\bar{c}$ pair between different heavy quark energy loss mechanisms – MCNLO + Herwig initialization of heavy quarks.

tic description of heavy flavor exclusive spectra observed in proton-proton collisions [219].

We present angular correlation functions of these $c\bar{c}$ pairs after they travel through the QGP medium in Fig.6.10. The qualitative conclusions drawn from the previous ideal scenario (Fig.6.9) still remains valid with the improved initialization scheme: while the pure radiative energy loss does not change the $c\bar{c}$ angular correlation function compared with its initial spectrum, pure collisional energy loss isotropizes the momentum space distribution of heavy quark much faster and leads to a peak around 0 due to the "partonic wind effect".

6.3.3 D-$\bar{D}$ Correlation and D-Hadron Correlation

Based on the results of the previous subsection, we find that the angular correlation function of $c\bar{c}$ pair is sensitive to the energy loss mechanism of heavy quarks inside the QGP. However, in reality, we are not able to measure bare quarks directly. Even if we could reconstruct them based on their decay products, it would still not be

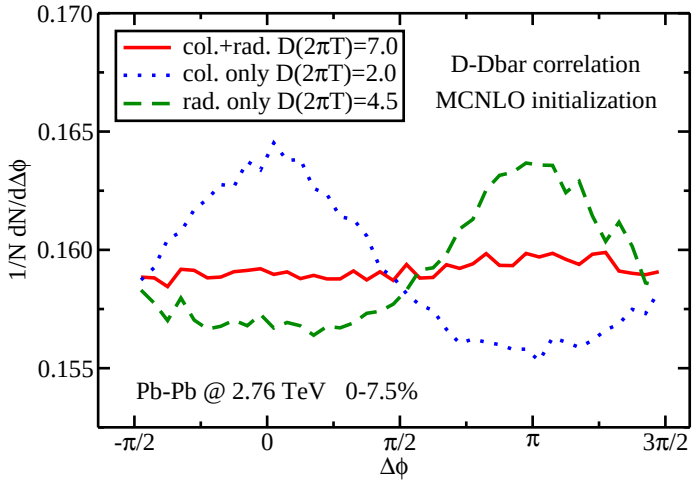

FIGURE 6.11: The D-$\bar{D}$ correlation in Pb-Pb central collisions ($-1 < y < 1$).

possible for experimentalists to identify which c and which $\bar{c}$ are correlated due to their large number in each collisional event (especially for central Pb-Pb collisions at LHC). In this subsection, we attempt to implement more realistic analysis techniques for this correlation function and investigate whether its dependence on the energy loss mechanism found in Fig.6.9 and Fig.6.10 still holds true for D mesons.

In Fig.6.11, we study the D-$\bar{D}$ correlation in the mid-rapidity region of central Pb-Pb collisions at LHC. Instead of tracking each heavy flavor pair from their initial production, we loop each D meson over all $\bar{D}$'s within a collisional event and pair up all of them. Figure 6.11 displays the correlation functions we obtain, once more compared between different energy loss mechanisms. We find that the shapes of these functions are similar to those of $c\bar{c}$ in the Fig.6.10 – peaking around π for pure radiative energy loss but peaking around 0 for collisional energy loss, except that they are on top of a large background. This background is contributed by all un-correlated D and $\bar{D}$ mesons. If the future experiment can measure such angular correlation function of heavy meson pairs or their decay products, it will provide us with a better understanding of the heavy quark energy loss mechanism inside QGP.

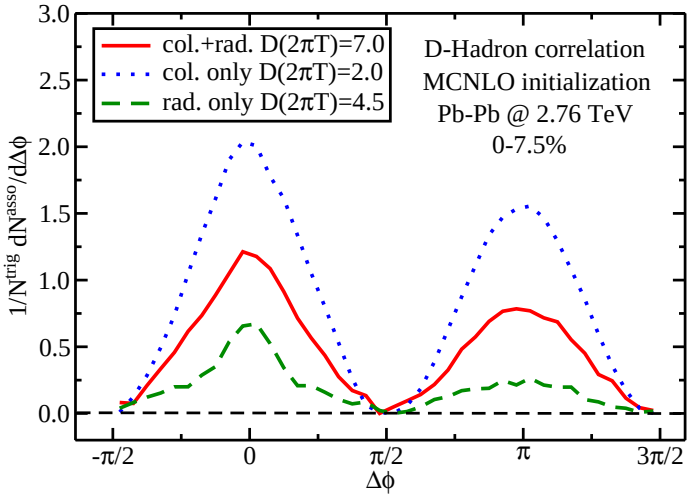

FIGURE 6.12: The D-hadron correlation in Pb-Pb central collisions. The backgrounds are subtracted at the minimum values of the correlation functions.

While it is relatively easy to calculate D-$\bar{D}$ correlation functions in heavy-ion collisions, it appears much harder to measure them due to the limited statistics of the reconstructed $D/\bar{D}$ mesons at this moment. However, the measurement of such a correlation function between heavy flavor decay electrons and all soft hadrons has already been attempted at the LHC experiment [220]. As a first step, we present our calculation of D-hadron correlation functions in Fig.6.12. A more direct comparison with the experimental data of electron-hadron correlation functions requires tracking all possible decay products of D mesons in our simulation and will be deferred to our future effort. Note that in Fig.6.12, we analyze the correlation between D meson and "all" soft hadrons after their hadronic interactions through UrQMD, and the latter part includes both the daughter soft hadrons produced by charm quark fragmentation and hadrons directly emitted from the QGP medium according to the Cooper-Frye formula. We observe the double peak structure around 0 and π in the D-hadron correlation functions and different energy loss mechanisms lead to different strengths of the peak structure. However, since now we are analyzing all possible hadrons, the

correlation function in the final state is no longer merely contributed by the heavy flavor initial production that we aim for in Fig.6.9 - Fig.6.11, but also contributed by the collective flow behavior of the bulk matter. This introduces an additional complication to the overall result. Note that the differences between the three energy loss mechanisms will also depend on different cuts of p_{T} and y regions, which should be investigated in more details in our future work. If the future data statistics allows, one may prefer the analysis of correlation functions between heavy flavor particles themselves such as heavy meson and their decay leptons, since the inclusion of all soft hadrons may introduce two particle correlations from the medium that mask the information we are looking for.

To conclude, in this section we have applied our newly developed framework of heavy flavor evolution that incorporates hadronic interaction in the late reaction stage to explore heavy-flavor-tagged angular correlation functions. We investigate the correlation functions between $c\bar{c}$ pairs, D and $\bar{D}$ mesons, and D and all possible soft hadrons, and find them sensitive to the choice of energy loss mechanism of the heavy quarks inside the QGP: while gluon radiation does not significantly modify the initial angular correlation function, quasi-elastic scattering results in a much faster isotropization of heavy quark momenta. These features can not be distinguished with single particle spectra alone. Thus, if future measurements can provide these correlation functions, we would obtain deeper insight into heavy flavor dynamics and therefore the properties of the QGP matter as well.

7

Conclusions and Outlook

Ultra-relativistic heavy-ion collisions provide the unique opportunity to compress nuclear matter into an extremely hot and dense state of matter to form a color deconfined quark-gluon plasma. Investigating this strongly coupled system provides us with a better understanding of QCD and reveals the state of our universe microseconds after the big bang.

Heavy quarks, including charm and bottom quarks, are dominantly produced in the every early stage of heavy-ion collisions through hard scatterings. They propagate through and observe the full evolution history of the created hot and dense nuclear matter and therefore serve as ideal probes of the medium properties. In this dissertation, we have developed a comprehensive framework that simulates the whole evolution of heavy flavor in heavy-ion collisions, including its initial production, energy loss in a QGP, hadronization at the critical temperature $T_{\rm c}$ from bare quarks to hadronic bound states and the subsequent scattering in a hadron gas to kinetic freeze-out.

We utilize a MC-Glauber model to initialize the position space distribution of heavy quark production. For the momentum space, a leading-order pQCD calcu-

lation is adopted. For nucleon-nucleon collisions, the parton distribution function CTEQ5 is used, whereas in nucleus-nucleus collisions, this distribution function is modified with the EPS parametrizations of the shadowing effect of the cold nuclear matter in the initial state. We show that this nuclear shadowing effect significantly suppresses the production rate of charm quarks at low p_{T} but slightly enhances it at larger p_{T} at both RHIC and LHC energies and therefore greatly reduces the D meson R_{AA} we observe at low p_{T} but slightly increases it at higher p_{T}. Compared to charm quarks, the impact of this shadowing effect appears weaker for bottom quarks but is still non-negligible.

To study the transport of heavy quarks inside a QGP medium, we have separated their energy loss processes into two parts: quasi-elastic scattering with light partons residing in the medium and medium-induced gluon radiation. In general, the former mechanism can be described using a Boltzmann equation with collision terms for $2 \to 2$ processes. We have demonstrated that in the limit of small momentum change during each interaction – which should be a good approximation for heavy-light interaction – the Boltzmann equation can be reduced to the Fokker-Plank equation and therefore be stochastically realized by the Langevin equation. In order to investigate heavy quark motion inside a dynamic QGP fireball, we couple the Langevin equation to hydrodynamic models that simulate the space-time evolution of the QGP by solving the equation in the local rest frame of the fluid cell. In this framework, we have studied the thermalization process of charm quarks inside QGP and found that with collisional energy loss alone, heavy quarks may not be able to approach local thermal equilibrium with the medium background within the QGP lifetime despite their strong response to the surrounding medium as revealed by their large suppression and collective flow behavior. Furthermore, we have investigated the model and parameter dependence of heavy quark energy loss within this Langevin approach. We have focused on the effects of two particular medium

properties – geometric anisotropy and its collective flow – and found that while the geometric anisotropy dominates the final heavy quark distributions in the high p_{T} region, the collective flow of the medium dominates at low p_{T}. The impact of the QGP geometry on heavy flavor observables has been further explored by comparing the Glauber and the KLN initializations of the hydrodynamic medium. We have shown that while the choice of initial conditions does not significantly affect the overall suppression of heavy quark, the larger geometric eccentricity given by the KLN initial condition results in a larger heavy flavor v_2 than that with the Glauber model by approximately 30%. Last but not least, the observed spectra of heavy flavor decay electrons are sensitive to the relative contributions from charm and bottom quarks. It has been found that a less than 1% difference in the initial charm-to-bottom ratio can lead to more than 30% variation of the non-photonic electron spectra. Therefore, narrowing down these uncertainties is necessary for a quantitative understanding of heavy quark dynamics inside QGP.

To incorporate gluon radiation into the heavy quark evolution, we have introduced a new term into the classical Langevin equation to describe the recoil force experienced by heavy quarks while radiating gluons. This force term is calculated according to the distribution function of medium-induced gluon taken from the Higher-Twist energy loss formalism. We have found that while the collisional energy loss dominates the observed heavy flavor spectra at low p_{T}, gluon radiation dominates the high p_{T} regime. The crossing point is around 6 GeV for charm quarks but 16 GeV for bottom quarks due to the larger mass of the latter. Thus, although the collisional energy loss mechanism alone may work well to describe the low p_{T} data of heavy flavor measured at RHIC, it is insufficient to describe observations at LHC. With this improved Langevin approach, we have studied the impact of initial state fluctuations in heavy-ion collisions on the heavy quark in-medium evolution. Our calculations have shown that although the total energy loss of heavy quarks is not very sensitive

to the sizes of local fluctuations in a 2-dimensional system, it increases significantly with the number of hot spots. Our simulations in a realistic QGP medium have demonstrated that fluctuating initial conditions may bring about 10% more suppression for the inclusive charm quark production at high p_{T} in central Pb-Pb collisions but the effect tends to diminish for more peripheral collisions. These results suggest that jet modification might be utilized to probe the fluctuations of QGP medium, such as the degree of inhomogeneity or the number of hot spots.

At the critical temperature T_{c}, both the bulk of the QGP and the heavy quarks need to hadronize into color neutral bound states. We utilize the Cooper-Frye formula to convert the QGP matter into soft hadrons and our hybrid fragmentation plus coalescence model to simulate the hadronization process of heavy quarks. We have demonstrated in detail how the 2-particle and 3-particle Wigner functions are constructed and how they are applied to the coalescence model for heavy meson and baryon formation respectively. Our numerical results display a significant enhancement of heavy meson spectra at medium p_{T} (around 2-4 GeV) when the coalescence model is introduced. Moreover, compared with the pure fragmentation mechanism, the introduction of heavy-light coalescence increases both R_{AA} and v_2 of the final state heavy mesons.

After the QGP freezes out, we collect both soft hadrons produced from the QGP and heavy mesons formed from heavy quarks, and use the UrQMD model to simulate the subsequent hadronic interactions among them until the hadron gas is so dilute that all interactions cease. Our calculations have indicated that the additional scattering and energy loss experienced by heavy mesons inside the hadron gas further suppress their nuclear modification factor R_{AA} at high p_{T} and increase their collective flow coefficient v_2 by over 30%.

With a combination of all the above mentioned ingredients, we have developed a framework for the full time evolution of heavy flavor produced in heavy-ion collisions.

Within this newly developed framework, our description of the D meson suppression and anisotropic flow is in good agreement with most of the existing experimental data from both RHIC and LHC. Furthermore, we have provided various predictions for experimental observations in the near further, such as the B meson suppression and flow, the dependence of the D meson $R_{\rm AA}$ on the participant number, and the non-photonic electron $R_{\rm AA}$ and v_2 observed at relatively low energy (62.4 GeV) Au-Au collisions.

In the end, we have applied our framework to explore new observables – heavy-flavor-tagged angular correlation functions – and show that while inclusive spectra may not be able to help us distinguish between different energy loss mechanisms of heavy quark inside QGP, the correlation functions may provide us with better insights. Our calculations have illustrated that gluon radiation does not significantly modify the initial angular correlation function of heavy flavor pairs, but quasi-elastic scattering results in a much faster isotropization of heavy quark momenta. Thus, if future experiments measure these correlation functions of heavy flavor pairs or of their decay products, we will be able to obtain a better understanding of the heavy flavor dynamics inside the QGP.

Our study has constituted an important step forward in the quantitative understanding of the heavy flavor dynamics in heavy-ion collisions. Nevertheless, it can be further improved in several directions, which we leave for future work. For instance, on the theoretical side, instead of implementing a lower cutoff of radiated gluon energy in our modified Langevin equation to guarantee heavy quarks can approach thermal equilibrium limit, a more rigorous treatment of the detailed balance between gluon radiation and absorption should be incorporated in the gluon distribution function emitted from heavy quarks. In addition, the current calculation of medium-induced gluon radiation only includes the effect of the momentum broadening in the transverse directions. Scatterings in the longitudinal direction may also

affect the gluon radiation pattern and influence final-state observables. On the phenomenology side, recent studies [221] suggest that apart from the production via initial hard scattering, heavy flavor may also be converted from hard gluons during or after their transport through the QGP medium. In this case, instead of heavy quarks, it is gluons that interact with and lose energy inside the hot and dense nuclear matter. This may affect the observed spectra of heavy mesons and has not been included in most transport model calculations of heavy quarks. Furthermore, our numerical framework can be easily extended from open heavy flavor to the study of heavy quarkonium. As discussed in Sec 6.3, the radial flow of the QGP background may significantly change the direction of heavy quark motion and therefore increases the number of collinear $Q\bar{Q}$ pairs after they travel through the medium. This would enhance the probability of J/ψ regeneration and can be straightforwardly investigated in our framework.

The launch of new heavy flavor detectors at both RHIC and LHC facilities in the upcoming years will certainly bring this field into a new era. Our understanding of heavy flavor dynamics has been greatly improved over the past few decades but many challenges still remain and even more puzzles are expected to emerge. As a clean hard probe, a better understanding of its interaction with the QGP will not only help us reveal more valuable information of a hot and dense QCD system, but also improve our knowledge of the state and evolution history of our early universe.

Appendix A

The Strong Coupling Constant α_s

In this dissertation, we adopt the running coupling constant α_s in the calculation of the spectrum of medium-induced gluon radiation [Eq.(4.6)]. Since this spectrum is obtained within the leading-order approximation, we keep α_s to the leading-order as well. Discussions about higher-order corrections can be found in Refs. [7, 8].

To the leading-order approximation, the strong coupling constant of QCD can be expressed as follows,

$$\alpha_s(k_\perp) = \frac{4\pi}{11 - 2N_f/3} \left(\ln \frac{k_\perp^2}{\Lambda^2} \right)^{-1} \tag{A.1}$$

where $k_\perp$ is the momentum transfer during interaction (transverse momentum of radiated gluon in our calculation), N_f is the number of flavor involved in the calculation, and Λ is a parameter which should be fixed with experimental data. In particle physics, α_s is first measured at high energy scale, such as the mass of Z^0 [4], and then extended to lower energy regime. In contrast, for the study of nucleus-nucleus collisions at relatively low energy region, it is preferred to fix $\Lambda = 200$ MeV with $N_f = 3$ which has been tested to give reasonable behavior of π production in proton-

proton collisions. As we extend to higher energies, N_f becomes 4 when $k_\perp$ exceeds the mass of the charm quark (M_c =1.27 GeV) and becomes 5 when $k_\perp$ exceeds the mass of the bottom quark (M_b =4.19 GeV). The parameter Λ is adjusted in different regions such that α_s is continuous on the boundary of M_c and M_b. To sum up, we use the following parametrization of this strong coupling constant:

$$\begin{cases} \Lambda = 200 \text{ MeV}, \ N_f = 3, & \text{for } k_\perp < M_c; \\ \Lambda = 173 \text{ MeV}, \ N_f = 4, & \text{for } M_c \leq k_\perp < M_b; \\ \Lambda = 131 \text{ MeV}, \ N_f = 5, & \text{for } k_\perp \geq M_b. \end{cases} \tag{A.2}$$

Appendix B

Properties of Gaussian Integrals

In this appendix, we review some algebraic properties of Gaussian integrals, which are useful for understanding the correlation functions of the thermal fluctuations in the Langevin equation [Eq.(3.22)]. One may refer to Ref. [222] for a more detailed summary of Gaussian integrals.

B.1 Gaussian Integrals

The general form of an n-dimensional Gaussian integral over variables x_i ($i = 1, \ldots, n$) can be written as

$$\mathcal{Z}(\tilde{A}) = \int d^n x e^{-A_2(\vec{x})}, \tag{B.1}$$

with

$$A_2(\vec{x}) \equiv \frac{1}{2} \sum_{i,j=1}^{n} x_i A_{ij} x_j, \tag{B.2}$$

in which $\tilde{A}$ (A_{ij}) is a complex symmetric matrix with a non-negative real part and non-vanishing eigenvalues a_i.

When $\tilde{A}$ is real, an orthonormal matrix $\tilde{O}$ can be constructed to diagonalize it with the transformation

$$x_i' = \sum_i O_{ij} x_j, \tag{B.3}$$

whose Jacobian is one. Then, we have

$$\mathcal{Z}(\tilde{A}) = \int d^n x e^{-\frac{1}{2}\sum a_i x_i'^2} = \prod_{i=1}^{n} \sqrt{\frac{2\pi}{a_i}} = (2\pi)^{n/2} \left(\det \tilde{A}\right)^{-1/2}. \tag{B.4}$$

In fact, since both the initial integral and the determinant are analytic functions of the coefficients (A_{ij}) of $\tilde{A}$, this identity can also be applied to the complex case.

One may further generalize the Gaussian integral to

$$\mathcal{Z}(\tilde{A}, \vec{b}) = \int d^n x e^{-A_2(\vec{x}) + \vec{b}\cdot\vec{x}}. \tag{B.5}$$

To evaluate $\mathcal{Z}(\tilde{A}, \vec{b})$, we first locate the minimum of the exponential part:

$$\frac{\partial}{\partial x_i}\left[-A_2(\vec{x}) + \vec{b}\cdot\vec{x}\right] = 0, \tag{B.6}$$

which yields

$$\sum_j A_{ij} x_j = b_i, \tag{B.7}$$

or

$$x_i = \sum_j \left(\tilde{A}^{-1}\right)_{ij} b_j. \tag{B.8}$$

Then we change the variables of Eq.(B.5) as

$$x_i = \sum_j \left(\tilde{A}^{-1}\right)_{ij} b_j + y_i, \tag{B.9}$$

and obtain

$$-A_2(\vec{x}) + \vec{b}\cdot\vec{x} = -A_2(\vec{y}) + w_2(\vec{b}), \tag{B.10}$$

in which we define

$$w_2(\vec{b}) \equiv \frac{1}{2}\sum_{i,j=1}^{n} b_i \left(\tilde{A}^{-1}\right)_{ij} b_j. \tag{B.11}$$

Thus we have

$$\mathcal{Z}(\tilde{A},\vec{b}) = e^{w_2(\vec{b})}\int d^n y e^{-A_2(\vec{y})} = (2\pi)^{n/2}\left(\det\tilde{A}\right)^{-1/2} e^{w_2(\vec{b})}. \tag{B.12}$$

B.2 Gaussian Expectation Values

If x_i's obey the Gaussian distribution, we define the correlation function (or the expectation value) of parts of the variables as follows:

$$\langle x_{k_1} x_{k_2} \dots x_{k_l}\rangle \equiv \mathcal{Z}^{-1}(\tilde{A},0)\int d^n x x_{k_1} x_{k_2}\dots x_{k_l} e^{-A_2(\vec{x})}, \tag{B.13}$$

in which the normalization is chosen such that $\langle 1\rangle = 1$ is satisfied.

To evaluate this expectation value, one may first derive both sides of Eq.(B.5) with respect to b_k and obtain:

$$\frac{\partial}{\partial b_k}\mathcal{Z}(\tilde{A},\vec{b}) = \int d^n x x_k e^{-A_2(\vec{x})+\vec{b}\cdot\vec{x}}. \tag{B.14}$$

By comparing Eq.(B.13) and Eq.(B.14), we find that in the limit of $\vec{b}=0$, we have

$$\langle x_k\rangle = \mathcal{Z}^{-1}(\tilde{A},0)\frac{\partial}{\partial b_k}\mathcal{Z}(\tilde{A},\vec{b})\Big|_{\vec{b}=0}. \tag{B.15}$$

Similarly, if we differentiate Eq.(B.5) repeatedly with respect to components of $\vec{b}$, we have

$$\begin{aligned}\langle x_{k_1} x_{k_2}\dots x_{k_l}\rangle &= \mathcal{Z}^{-1}(\tilde{A},0)\left[\frac{\partial}{\partial b_{k_1}}\frac{\partial}{\partial b_{k_2}}\dots\frac{\partial}{\partial b_{k_l}}\mathcal{Z}(\tilde{A},\vec{b})\right]\Big|_{\vec{b}=0}\\ &= \left[\frac{\partial}{\partial b_{k_1}}\frac{\partial}{\partial b_{k_2}}\dots\frac{\partial}{\partial b_{k_l}}e^{w_2(\vec{b})}\right]\Big|_{\vec{b}=0},\end{aligned} \tag{B.16}$$

in which we have taken Eq.(B.12) into account.

More generally, if $F(\vec{x})$ is a power series of x_i, we have

$$\langle F(\vec{x})\rangle = \left[F\left(\frac{\partial}{\partial\vec{b}}\right)e^{w_2(\vec{b})}\right]\Bigg|_{\vec{b}=0}. \tag{B.17}$$

In the end, we apply these properties of Gaussian integrals to our thermal noise term in the Langevin equation. As described in Eq.(3.22), the thermal fluctuation obeys the following Gaussian distribution:

$$P(\vec{\rho}) = \left(\frac{1}{2\pi}\right)^3 \exp\left(-\frac{\vec{\rho}^2}{2}\right). \tag{B.18}$$

By comparing Eq.(B.18) with the standard form of the Gaussian integral Eq.(B.1)-(B.2), we may set $A_{ij} = \delta_{ij}$ in this special case. Therefore, it follows from Eq.(B.11) that

$$w_2(\vec{b}) = \frac{1}{2}\vec{b}^2. \tag{B.19}$$

By substituting Eq.(B.19) into Eq.(B.16), one obtains

$$\langle\rho_i\rangle = \left(\frac{\partial}{\partial b_i}e^{\vec{b}^2/2}\right)\Bigg|_{\vec{b}=0} = 0, \tag{B.20}$$

$$\langle\rho_i\rho_j\rangle = \left(\frac{\partial}{\partial b_i}\frac{\partial}{\partial b_j}e^{\vec{b}^2/2}\right)\Bigg|_{\vec{b}=0} = \delta_{ij}. \tag{B.21}$$

These are the correlation functions we showed in Eq.(3.23).

Appendix C

The Spatial Diffusion Coefficient of Heavy Quark

C.1 Definition of the Diffusion Coefficient

The standard form of the diffusion equation reads

$$\frac{\partial \rho(\vec{x},t)}{\partial t} = D \bigtriangledown^2 \rho(\vec{x},t), \tag{C.1}$$

where $\rho(\vec{x},t)$ is the density distribution in a d-dimensional space satisfying

$$\int d^d x \rho(\vec{x},t) = 1, \tag{C.2}$$

and D is called the spatial diffusion coefficient. One may check that the solution to Eq.(C.1) with the initial condition $\vec{x}(t=0)=0$ reads

$$\rho(\vec{x},t) = \frac{1}{(4\pi D t)^{d/2}} \exp\left(-\frac{|\vec{x}|^2}{4Dt}\right). \tag{C.3}$$

Furthermore, we may apply Eq.(B.16) to Eq.(C.3) and obtain the expectation value of $|\vec{x}|^2$ as a function of time:

$$\left\langle |\vec{x}|^2 \right\rangle = \int d^d x \, |\vec{x}|^2 \, \rho(\vec{x},t) = 2dDt, \tag{C.4}$$

where we let $A_{ij} = \frac{1}{2Dt}\delta_{ij}$, and thus $w_2(\vec{b}) = \vec{b}^2 Dt$ as respectively defined in Eq.(B.2) and Eq.(B.11).

C.2 Diffusion Coefficient in the Langevin Equation

To investigate the diffusion behavior of heavy quark in a thermal bath, we focus on the low momentum region (the classical limit) and re-write the second line of Eq.(3.44) as

$$\frac{dp_i}{dt} = -\eta_D p_i + \zeta_i(t), \tag{C.5}$$

where $\eta_D = \Gamma(0)$ and is assumed as a good approximation up to the scale of thermal momentum, and $\zeta_i = \sqrt{\kappa}\rho_i/\sqrt{t}$ represents the thermal force satisfying

$$\langle \zeta_i(t)\zeta_j(t')\rangle_\rho = \kappa\delta_{ij}\delta(t-t'). \tag{C.6}$$

In the following discussion, all the average value is taken over the thermal fluctuation and we will drop the subscript ρ for short. One may directly solve Eq.(C.5) with the initial condition $p_i(t=-\infty)=0$ as

$$p_i(t) = \int_{-\infty}^{t} dt' e^{\eta_D(t'-t)}\zeta_i(t'). \tag{C.7}$$

In order to extract the diffusion coefficient in the Langevin equation, we utilize Eq.(C.4) and evaluate $\left\langle |\vec{x}|^2 \right\rangle$ as

$$\langle x_i(t)x_i(t)\rangle = \int_0^t dt_1 \int_0^t dt_2 \frac{1}{M^2}\left\langle p_i(t_1)p_i(t_2)\right\rangle, \tag{C.8}$$

in which we use the initial condition $x_i(t=0)=0$ for the position space.

By using Eq.(C.6) and (C.7), we have

$$\begin{aligned}\langle p_i(t_1)p_i(t_2)\rangle &= \int_{-\infty}^{t_1} dt' \int_{-\infty}^{t_2} dt'' e^{\eta_D(t'-t_1)}e^{\eta_D(t''-t_2)}\langle\zeta_i(t')\zeta_i(t'')\rangle \\ &= \int_{-\infty}^{t_1} dt' \int_{-\infty}^{t_2} dt'' e^{\eta_D(t'+t''-t_1-t_2)}\kappa\delta(t'-t'').\end{aligned} \tag{C.9}$$

One may first consider the case of $t_1 > t_2$ and set $t' = s + t''$. Then we obtain

$$\begin{aligned}\langle p_i(t_1)p_i(t_2)\rangle &= \kappa \int_{-\infty}^{t_2} dt'' \int_{-\infty}^{t_1-t''} ds e^{\eta_D(s+2t''-t_1-t_2)}\delta(s) \\ &= \kappa \int_{-\infty}^{t_2} dt'' e^{\eta_D(2t''-t_1-t_2)} \\ &= \frac{\kappa}{2\eta_D} e^{-\eta_D(t_1-t_2)}. \end{aligned} \tag{C.10}$$

Similarly, for the case of $t_2 > t_1$, one should obtain

$$\langle p_i(t_1)p_i(t_2)\rangle = \frac{\kappa}{2\eta_D} e^{-\eta_D(t_2-t_1)}. \tag{C.11}$$

To sum up, we have

$$\langle p_i(t_1)p_i(t_2)\rangle = \frac{\kappa}{2\eta_D} e^{-\eta_D|t_1-t_2|}. \tag{C.12}$$

Therefore, by substituting Eq.(C.12) back into Eq.(C.8), we have

$$\langle x_i(t)x_i(t)\rangle = \frac{\kappa}{2M^2\eta_D} \int_0^t dt_1 \int_0^t dt_2 e^{-\eta_D|t_1-t_2|}. \tag{C.13}$$

One may let $t_1 = s + t_2$ and separate the above integral into $s > 0$ and $s < 0$ parts, and get

$$\begin{aligned}\langle x_i(t)x_i(t)\rangle &= \frac{\kappa}{2M^2\eta_D} \left(\int_{-t}^{0} ds \int_{-s}^{t} dt_2 e^{\eta_D s} + \int_0^t ds \int_0^{t-s} dt_2 e^{-\eta_D s} \right) \\ &= \frac{\kappa}{2M^2\eta_D} \left(\int_{-t}^{0} ds (t+s) e^{\eta_D s} + \int_0^t ds (t-s) e^{-\eta_D s} \right) \\ &= \frac{\kappa}{M^2\eta_D} \int_0^t ds (t-s) e^{-\eta_D s}, \end{aligned} \tag{C.14}$$

where we have transformed $s \to -s$ in the first ($s < 0$) part. In the end, we obtain

$$\begin{aligned}\langle x_i(t)x_i(t)\rangle &= \frac{\kappa}{M^2\eta_D}\left(t + \frac{\partial}{\partial\eta_D}\right)\int_0^t ds e^{-\eta_D s} \\ &= \frac{\kappa}{M^2\eta_D}\left(t + \frac{\partial}{\partial\eta_D}\right)\left[\frac{1}{\eta_D}\left(1 - e^{-\eta_D t}\right)\right] \\ &= \frac{\kappa}{M^2\eta_D^2}\left[t - \frac{1}{\eta_D}\left(1 - e^{-\eta_D t}\right)\right]. \end{aligned} \tag{C.15}$$

By summing over the three spatial components and taking the large t limit, we have

$$\left\langle |\vec{x}|^2 \right\rangle = \frac{3\kappa}{M^2\eta_D^2}t. \tag{C.16}$$

One may extract the spatial diffusion coefficient by comparing Eq.(C.16) and Eq.(C.4), and obtain

$$D = \frac{\kappa}{2M^2\eta_D^2}. \tag{C.17}$$

Recall that we set $\eta_D = \Gamma(0)$ at the beginning and $\Gamma(\vec{p})$ and κ are related by the fluctuation-dissipation relation $\Gamma = \kappa/2TE$ [Eq.(3.43)], we have

$$D = \frac{T}{M\Gamma(0)} = \frac{2T^2}{\kappa}. \tag{C.18}$$

This is the only transport coefficient (free parameter) we may tune in our Langevin framework.

Bibliography

[1] P. W. Higgs, Phys. Rev. Lett. **13**, 508 (1964).

[2] ATLAS Collaboration, G. Aad *et al.*, Phys. Lett. **B716**, 1 (2012), arXiv:1207.7214.

[3] CMS Collaboration, S. Chatrchyan *et al.*, Phys. Lett. **B716**, 30 (2012), arXiv:1207.7235.

[4] S. Bethke, Prog. Part. Nucl. Phys. **58**, 351 (2007), arXiv:hep-ex/0606035.

[5] D. J. Gross and F. Wilczek, Phys. Rev. Lett. **30**, 1343 (1973).

[6] H. D. Politzer, Phys. Rev. Lett. **30**, 1346 (1973).

[7] K. Chetyrkin, B. A. Kniehl, and M. Steinhauser, Phys. Rev. Lett. **79**, 2184 (1997), arXiv:hep-ph/9706430.

[8] G. Prosperi, M. Raciti, and C. Simolo, Prog. Part. Nucl. Phys. **58**, 387 (2007), arXiv:hep-ph/0607209.

[9] S. Borsanyi *et al.*, JHEP **1011**, 077 (2010), arXiv:1007.2580.

[10] M. Gyulassy and L. McLerran, Nucl. Phys. **A750**, 30 (2005), nucl-th/0405013.

[11] S. Sarkar, H. Satz, and B. Sinha, The Physics of the Quark-Gluon Plasma (Springer, 2010) .

[12] M. G. Alford, A. Schmitt, K. Rajagopal, and T. Schfer, Rev. Mod. Phys. **80**, 1455 (2008), arXiv:0709.4635.

[13] R. J. Glauber and G. Matthiae, Nucl. Phys. **B21**, 135 (1970).

[14] A. Bialas, M. Bleszynski, and W. Czyz, Nucl. Phys. **B111**, 461 (1976).

[15] M. L. Miller, K. Reygers, S. J. Sanders, and P. Steinberg, Ann. Rev. Nucl. Part. Sci. **57**, 205 (2007), arXiv:nucl-ex/0701025.

[16] D. Kharzeev, E. Levin, and M. Nardi, Nucl. Phys. **A747**, 609 (2005), hep-ph/0408050.

[17] H.-J. Drescher and Y. Nara, Phys. Rev. **C76**, 041903 (2007), arXiv:0707.0249.

[18] D. Teaney, J. Lauret, and E. V. Shuryak, Phys. Rev. Lett. **86**, 4783 (2001), arXiv:nucl-th/0011058.

[19] P. Huovinen, P. F. Kolb, U. W. Heinz, P. V. Ruuskanen, and S. A. Voloshin, Phys. Lett. **B503**, 58 (2001), hep-ph/0101136.

[20] T. Hirano and K. Tsuda, Phys. Rev. **C66**, 054905 (2002), nucl-th/0205043.

[21] C. Nonaka and S. A. Bass, Phys. Rev. **C75**, 014902 (2007), nucl-th/0607018.

[22] H. Song and U. W. Heinz, Phys. Lett. **B658**, 279 (2008), arXiv:0709.0742.

[23] M. Luzum and P. Romatschke, Phys. Rev. **C78**, 034915 (2008), arXiv:0804.4015.

[24] Z. Qiu, C. Shen, and U. Heinz, Phys. Lett. **B707**, 151 (2012), arXiv:1110.3033.

[25] L. Pang, Q. Wang, and X.-N. Wang, Phys. Rev. **C86**, 024911 (2012), arXiv:1205.5019.

[26] H. Song, S. A. Bass, U. Heinz, T. Hirano, and C. Shen, Phys. Rev. Lett. **106**, 192301 (2011), arXiv:1011.2783.

[27] P. Kovtun, D. T. Son, and A. O. Starinets, Phys. Rev. Lett. **94**, 111601 (2005), hep-th/0405231.

[28] F. Cooper and G. Frye, Phys. Rev. **D10**, 186 (1974).

[29] D. Molnar and S. A. Voloshin, Phys. Rev. Lett. **91**, 092301 (2003), nucl-th/0302014.

[30] R. J. Fries, B. Müller, C. Nonaka, and S. A. Bass, Phys. Rev. Lett. **90**, 202303 (2003), nucl-th/0301087.

[31] R. J. Fries, B. Müller, C. Nonaka, and S. A. Bass, Phys. Rev. **C68**, 044902 (2003), nucl-th/0306027.

[32] V. Greco, C. M. Ko, and P. Levai, Phys. Rev. Lett. **90**, 202302 (2003), nucl-th/0301093.

[33] B. Andersson, G. Gustafson, G. Ingelman, and T. Sjostrand, Phys. Rept. **97**, 31 (1983).

[34] B. Webber, Nucl. Phys. **B238**, 492 (1984).

[35] J. C. Collins, Nucl. Phys. **B396**, 161 (1993), arXiv:hep-ph/9208213.

[36] S. A. Bass *et al.*, Prog. Part. Nucl. Phys. **41**, 225 (1998), nucl-th/9803035.

[37] U. Heinz, Lecture notes of the 3rd Huada Summer School on QCD (2014) .

[38] Z. Qiu, (2013), arXiv:1308.2182.

[39] M. Luzum and H. Petersen, J. Phys. **G41**, 063102 (2014), arXiv:1312.5503.

[40] B. Alver and G. Roland, Phys. Rev. **C81**, 054905 (2010), arXiv:1003.0194.

[41] H. Petersen, G.-Y. Qin, S. A. Bass, and B. Müller, Phys. Rev. **C82**, 041901 (2010), arXiv:1008.0625.

[42] P. Staig and E. Shuryak, (2010), arXiv:1008.3139.

[43] G.-Y. Qin, H. Petersen, S. A. Bass, and B. Müller, Phys. Rev. **C82**, 064903 (2010), arXiv:1009.1847.

[44] G.-L. Ma and X.-N. Wang, Phys. Rev. Lett. **106**, 162301 (2011), arXiv:1011.5249.

[45] J. Xu and C. M. Ko, Phys. Rev. **C83**, 021903 (2011), arXiv:1011.3750.

[46] D. Teaney and L. Yan, Phys. Rev. **C83**, 064904 (2011), arXiv:1010.1876.

[47] Z. Qiu and U. W. Heinz, Phys. Rev. **C84**, 024911 (2011), arXiv:1104.0650.

[48] R. S. Bhalerao, M. Luzum, and J.-Y. Ollitrault, Phys. Rev. **C84**, 034910 (2011), arXiv:1104.4740.

[49] S. Floerchinger and U. A. Wiedemann, JHEP **1111**, 100 (2011), arXiv:1108.5535.

[50] PHENIX Collaboration, A. Adare *et al.*, Phys. Rev. Lett. **107**, 252301 (2011), arXiv:1105.3928.

[51] STAR Collaboration, L. Adamczyk *et al.*, Phys. Rev. **C88**, 014904 (2013), arXiv:1301.2187.

[52] ATLAS Collaboration, G. Aad *et al.*, Phys. Rev. **C86**, 014907 (2012), arXiv:1203.3087.

[53] C. Gale, S. Jeon, B. Schenke, P. Tribedy, and R. Venugopalan, Phys. Rev. Lett. **110**, 012302 (2013), arXiv:1209.6330.

[54] H. Niemi, G. S. Denicol, P. Huovinen, E. Molnar, and D. H. Rischke, Phys. Rev. Lett. **106**, 212302 (2011), arXiv:1101.2442.

[55] A. Accardi *et al.*, (2004), arXiv:hep-ph/0310274.

[56] V. Gribov and L. Lipatov, Sov. J. Nucl. Phys. **15**, 675 (1972).

[57] V. Gribov and L. Lipatov, Sov. J. Nucl. Phys. **15**, 438 (1972).

[58] G. Altarelli and G. Parisi, Nucl. Phys. **B126**, 298 (1977).

[59] Y. L. Dokshitzer, Sov. Phys. JETP **46**, 641 (1977).

[60] J. D. Bjorken, FERMILAB-PUB-82-059-THY.

[61] B. Müller, J. Schukraft, and B. Wyslouch, Ann. Rev. Nucl. Part. Sci. **62**, 361 (2012), arXiv:1202.3233.

[62] R. Sharma, I. Vitev, and B.-W. Zhang, Phys. Rev. **C80**, 054902 (2009), arXiv:0904.0032.

[63] T. Renk, H. Holopainen, R. Paatelainen, and K. J. Eskola, Phys. Rev. **C84**, 014906 (2011), arXiv:1103.5308.

[64] X.-F. Chen, T. Hirano, E. Wang, X.-N. Wang, and H. Zhang, Phys. Rev. **C84**, 034902 (2011), arXiv:1102.5614.

[65] A. Majumder and C. Shen, Phys. Rev. Lett. **109**, 202301 (2012), arXiv:1103.0809.

[66] K. C. Zapp, F. Krauss, and U. A. Wiedemann, (2011), arXiv:1111.6838.

[67] E. Braaten and M. H. Thoma, Phys. Rev. **D44**, 2625 (1991).

[68] G.-Y. Qin *et al.*, Phys. Rev. Lett. **100**, 072301 (2008), arXiv:0710.0605.

[69] X.-N. Wang and M. Gyulassy, Phys. Rev. Lett. **68**, 1480 (1992).

[70] M. Gyulassy and X.-N. Wang, Nucl. Phys. **B420**, 583 (1994), nucl-th/9306003.

[71] B. G. Zakharov, JETP Lett. **63**, 952 (1996), arXiv:hep-ph/9607440.

[72] B. G. Zakharov, JETP Lett. **65**, 615 (1997), hep-ph/9704255.

[73] B. G. Zakharov, Phys. Atom. Nucl. **61**, 838 (1998), arXiv:hep-ph/9807540.

[74] R. Baier, Y. L. Dokshitzer, A. H. Mueller, S. Peigne, and D. Schiff, Nucl. Phys. **B484**, 265 (1997), hep-ph/9608322.

[75] R. Baier, Y. L. Dokshitzer, A. H. Mueller, S. Peigne, and D. Schiff, Nucl. Phys. **B483**, 291 (1997), hep-ph/9607355.

[76] U. A. Wiedemann, Nucl. Phys. **B588**, 303 (2000), arXiv:hep-ph/0005129.

[77] U. A. Wiedemann, Nucl. Phys. **B582**, 409 (2000), arXiv:hep-ph/0003021.

[78] C. A. Salgado and U. A. Wiedemann, Phys. Rev. Lett. **89**, 092303 (2002), hep-ph/0204221.

[79] C. A. Salgado and U. A. Wiedemann, Phys. Rev. **D68**, 014008 (2003), hep-ph/0302184.

[80] M. Gyulassy, P. Levai, and I. Vitev, Nucl. Phys. **B571**, 197 (2000), arXiv:hep-ph/9907461.

[81] M. Gyulassy, P. Levai, and I. Vitev, Nucl. Phys. **B594**, 371 (2001), arXiv:nucl-th/0006010.

[82] M. Gyulassy, P. Levai, and I. Vitev, Phys. Lett. **B538**, 282 (2002), arXiv:nucl-th/0112071.

[83] M. Djordjevic and M. Gyulassy, Nucl. Phys. **A733**, 265 (2004), arXiv:nucl-th/0310076.

[84] X.-F. Guo and X.-N. Wang, Phys. Rev. Lett. **85**, 3591 (2000), arXiv:hep-ph/0005044.

[85] X.-N. Wang and X.-F. Guo, Nucl. Phys. **A696**, 788 (2001), arXiv:hep-ph/0102230.

[86] B.-W. Zhang and X.-N. Wang, Nucl. Phys. **A720**, 429 (2003), arXiv:hep-ph/0301195.

[87] A. Majumder, E. Wang, and X.-N. Wang, Phys. Rev. Lett. **99**, 152301 (2007), arXiv:nucl-th/0412061.

[88] A. Majumder and B. Müller, Phys. Rev. **C77**, 054903 (2008), arXiv:0705.1147.

[89] A. Majumder, R. J. Fries, and B. Müller, Phys. Rev. **C77**, 065209 (2008), arXiv:0711.2475.

[90] P. Arnold, G. D. Moore, and L. G. Yaffe, JHEP **11**, 001 (2000), hep-ph/0010177.

[91] P. Arnold, G. D. Moore, and L. G. Yaffe, JHEP **11**, 057 (2001), hep-ph/0109064.

[92] S. Jeon and G. D. Moore, Phys. Rev. **C71**, 034901 (2005), hep-ph/0309332.

[93] S. Turbide, C. Gale, S. Jeon, and G. D. Moore, Phys. Rev. **C72**, 014906 (2005), hep-ph/0502248.

[94] S. A. Bass *et al.*, Phys. Rev. **C79**, 024901 (2009), arXiv:0808.0908.

[95] K. M. Burke *et al.*, (2013), arXiv:1312.5003.

[96] H. Zhang, J. F. Owens, E. Wang, and X.-N. Wang, Phys. Rev. Lett. **98**, 212301 (2007), arXiv:nucl-th/0701045.

[97] T. Renk, Phys. Rev. **C78**, 034904 (2008), arXiv:0803.0218.

[98] T. Renk, Phys. Rev. **C74**, 034906 (2006), hep-ph/0607166.

[99] H. Zhang, J. Owens, E. Wang, and X.-N. Wang, Phys. Rev. Lett. **103**, 032302 (2009), arXiv:0902.4000.

[100] G.-Y. Qin, J. Ruppert, C. Gale, S. Jeon, and G. D. Moore, Phys. Rev. **C80**, 054909 (2009), arXiv:0906.3280.

[101] H. van Hees, V. Greco, and R. Rapp, Phys. Rev. **C73**, 034913 (2006), arXiv:nucl-th/0508055.

[102] R. Rapp and H. van Hees, published in R. C. Hwa, X.-N. Wang (Eds.), Quark Gluon Plasma 4 (World Scientific, 2010) , 111, arXiv:0903.1096.

[103] Z.-W. Lin and D. Molnar, Phys. Rev. **C68**, 044901 (2003), nucl-th/0304045.

[104] V. Greco, C. M. Ko, and R. Rapp, Phys. Lett. **B595**, 202 (2004), nucl-th/0312100.

[105] Y. Oh, C. M. Ko, S. H. Lee, and S. Yasui, Phys. Rev. **C79**, 044905 (2009), arXiv:0901.1382.

[106] M. He, R. J. Fries, and R. Rapp, Phys. Rev. **C86**, 014903 (2012), arXiv:1106.6006.

[107] S. Cao, G.-Y. Qin, and S. A. Bass, Phys. Rev. **C88**, 044907 (2013), arXiv:1308.0617.

[108] ALICE Collaboration, A. Grelli, Nucl. Phys. **A904-905**, 635c (2013), arXiv:1210.7332.

[109] ALICE Collaboration, B. Abelev *et al.*, Phys. Rev. Lett. **111**, 102301 (2013), arXiv:1305.2707.

[110] STAR collaboration, D. Tlusty, Nucl. Phys. **A904-905**, 639c (2013), arXiv:1211.5995.

[111] STAR Collaboration, L. Adamczyk *et al.*, (2014), arXiv:1404.6185.

[112] PHENIX Collaboration, A. Adare *et al.*, Phys. Rev. **C84**, 044905 (2011), arXiv:1005.1627.

[113] PHENIX Collaboration, A. Adare *et al.*, (2014), arXiv:1405.3301.

[114] ALICE Collaboration, B. Abelev *et al.*, JHEP **1209**, 112 (2012), arXiv:1203.2160.

[115] S. Wicks, W. Horowitz, M. Djordjevic, and M. Gyulassy, Nucl. Phys. **A784**, 426 (2007), arXiv:nucl-th/0512076.

[116] T. Renk, Phys. Rev. **C76**, 064905 (2007), arXiv:0708.4319.

[117] B. G. Zakharov, JETP Lett. **86**, 444 (2007), arXiv:0708.0816.

[118] G. D. Moore and D. Teaney, Phys. Rev. **C71**, 064904 (2005), hep-ph/0412346.

[119] M. G. Mustafa, Phys. Rev. **C72**, 014905 (2005), hep-ph/0412402.

[120] Y. L. Dokshitzer and D. E. Kharzeev, Phys. Lett. **B519**, 199 (2001), arXiv:hep-ph/0106202.

[121] N. Armesto, A. Dainese, C. A. Salgado, and U. A. Wiedemann, Phys. Rev. **D71**, 054027 (2005), arXiv:hep-ph/0501225.

[122] B.-W. Zhang, E. Wang, and X.-N. Wang, Phys. Rev. Lett. **93**, 072301 (2004), arXiv:nucl-th/0309040.

[123] B. Svetitsky, Phys. Rev. **D37**, 2484 (1988).

[124] Y. Akamatsu, T. Hatsuda, and T. Hirano, Phys. Rev. **C79**, 054907 (2009), arXiv:0809.1499.

[125] P. B. Gossiaux *et al.*, (2011), arXiv:1102.1114.

[126] C. Young, B. Schenke, S. Jeon, and C. Gale, Phys. Rev. **C86**, 034905 (2012), arXiv:1111.0647.

[127] W. Alberico *et al.*, Eur. Phys. J. **C71**, 1666 (2011), arXiv:1101.6008.

[128] T. Lang, H. van Hees, J. Steinheimer, and M. Bleicher, (2012), arXiv:1211.6912.

[129] R. Abir, U. Jamil, M. G. Mustafa, and D. K. Srivastava, Phys. Lett. **B715**, 183 (2012), arXiv:1203.5221.

[130] J. Xu, A. Buzzatti, and M. Gyulassy, (2014), arXiv:1402.2956.

[131] P. Gossiaux, J. Aichelin, T. Gousset, and V. Guiho, J. Phys. **G37**, 094019 (2010), arXiv:1001.4166.

[132] M. Nahrgang, J. Aichelin, P. B. Gossiaux, and K. Werner, (2013), arXiv:1305.3823.

[133] J. Uphoff, O. Fochler, Z. Xu, and C. Greiner, Phys. Lett. **B717**, 430 (2012), arXiv:1205.4945.

[134] S. Cao, G.-Y. Qin, S. A. Bass, and B. Müller, Nucl. Phys. **A904-905**, 653c (2013), arXiv:1209.5410.

[135] A. Majumder, Phys. Rev. **D85**, 014023 (2012), arXiv:0912.2987.

[136] G.-Y. Qin and A. Majumder, Phys. Rev. **C87**, 024909 (2013), arXiv:1205.5741.

[137] T. Sjostrand, S. Mrenna, and P. Z. Skands, JHEP **0605**, 026 (2006), arXiv:hep-ph/0603175.

[138] C. B. Dover, U. W. Heinz, E. Schnedermann, and J. Zimanyi, Phys. Rev. **C44**, 1636 (1991).

[139] V. Greco, C. M. Ko, and P. Levai, Phys. Rev. **C68**, 034904 (2003), nucl-th/0305024.

[140] L.-W. Chen and C. M. Ko, Phys. Rev. **C73**, 044903 (2006), arXiv:nucl-th/0602025.

[141] K. C. Han, R. J. Fries, and C. M. Ko, J. Phys. Conf. Ser. **420**, 012044 (2013), arXiv:1209.1141.

[142] H. van Hees, M. Mannarelli, V. Greco, and R. Rapp, Phys. Rev. Lett. **100**, 192301 (2008), arXiv:0709.2884.

[143] Z.-W. Lin, T. Di, and C. Ko, Nucl. Phys. **A689**, 965 (2001), arXiv:nucl-th/0006086.

[144] T. Matsui and H. Satz, Phys. Lett. **B178**, 416 (1986).

[145] F. Karsch and H. Satz, Z. Phys. **C51**, 209 (1991).

[146] CMS Collaboration, S. Chatrchyan *et al.*, Phys. Rev. Lett. **109**, 222301 (2012), arXiv:1208.2826.

[147] CMS Collaboration, S. Chatrchyan *et al.*, Phys. Rev. Lett. **107**, 052302 (2011), arXiv:1105.4894.

[148] F. Karsch, M. Mehr, and H. Satz, Z. Phys. **C37**, 617 (1988).

[149] H. Satz, J. Phys. **G32**, R25 (2006), arXiv:hep-ph/0512217.

[150] T. Umeda, R. Katayama, O. Miyamura, and H. Matsufuru, Int. J. Mod. Phys. **A16**, 2215 (2001), arXiv:hep-lat/0011085.

[151] M. Asakawa and T. Hatsuda, Phys. Rev. Lett. **92**, 012001 (2004), arXiv:hep-lat/0308034.

[152] S. Datta, F. Karsch, P. Petreczky, and I. Wetzorke, Phys. Rev. **D69**, 094507 (2004), arXiv:hep-lat/0312037.

[153] H. Iida, T. Doi, N. Ishii, and H. Suganuma, PoS **LAT2005**, 184 (2006), arXiv:hep-lat/0509129.

[154] A. Jakovac, P. Petreczky, K. Petrov, and A. Velytsky, Phys. Rev. **D75**, 014506 (2007), arXiv:hep-lat/0611017.

[155] R. Morrin *et al.*, PoS **LAT2005**, 176 (2006), arXiv:hep-lat/0509115.

[156] G. Aarts *et al.*, Nucl. Phys. **A785**, 198 (2007), arXiv:hep-lat/0608009.

[157] PHENIX Collaboration, A. Adare *et al.*, Phys. Rev. Lett. **98**, 232301 (2007), arXiv:nucl-ex/0611020.

[158] STAR Collaboration, B. Abelev *et al.*, Phys. Rev. **C80**, 041902 (2009), arXiv:0904.0439.

[159] ALICE Collaboration, H. Yang, Nucl. Phys. **A904-905**, 673c (2013), arXiv:1211.0799.

[160] ALICE Collaboration, E. Scomparin, Nucl. Phys. **A904-905**, 202c (2013), arXiv:1211.1623.

[161] R. L. Thews, M. Schroedter, and J. Rafelski, Phys. Rev. **C63**, 054905 (2001), arXiv:hep-ph/0007323.

[162] A. Andronic, P. Braun-Munzinger, K. Redlich, and J. Stachel, Phys. Lett. **B652**, 259 (2007), arXiv:nucl-th/0701079.

[163] X. Zhao and R. Rapp, Phys. Lett. **B664**, 253 (2008), arXiv:0712.2407.

[164] L. Yan, P. Zhuang, and N. Xu, Phys. Rev. Lett. **97**, 232301 (2006), arXiv:nucl-th/0608010.

[165] Y.-P. Liu, Z. Qu, N. Xu, and P. Zhuang, Phys. Lett. **B678**, 72 (2009), arXiv:0901.2757.

[166] K. Zhou, N. Xu, Z. Xu, and P. Zhuang, Phys. Rev. **C89**, 054911 (2014), arXiv:1401.5845.

[167] R. Vogt, S. J. Brodsky, and P. Hoyer, Nucl. Phys. **B383**, 643 (1992).

[168] Z.-W. Lin and M. Gyulassy, Phys. Rev. **C51**, 2177 (1995), arXiv:nucl-th/9409007.

[169] P. Levai, B. Müller, and X.-N. Wang, Phys. Rev. **C51**, 3326 (1995), arXiv:hep-ph/9412352.

[170] B.-W. Zhang, C.-M. Ko, and W. Liu, Phys. Rev. **C77**, 024901 (2008), arXiv:0709.1684.

[171] M. Younus and D. K. Srivastava, J. Phys. **G37**, 115006 (2010), arXiv:1008.1120.

[172] W. Liu and R. Fries, Phys. Rev. **C78**, 037902 (2008), arXiv:0805.1093.

[173] B. Combridge, Nucl. Phys. **B151**, 429 (1979).

[174] CTEQ, H. L. Lai *et al.*, Eur. Phys. J. **C12**, 375 (2000), arXiv:hep-ph/9903282.

[175] K. J. Eskola, H. Paukkunen, and C. A. Salgado, JHEP **0807**, 102 (2008), arXiv:0802.0139.

[176] K. Eskola, H. Paukkunen, and C. Salgado, JHEP **0904**, 065 (2009), arXiv:0902.4154.

[177] D. Kharzeev, C. Lourenco, M. Nardi, and H. Satz, Z. Phys. **C74**, 307 (1997), arXiv:hep-ph/9612217.

[178] D. Kharzeev and M. Nardi, Phys. Lett. **B507**, 121 (2001), arXiv:nucl-th/0012025.

[179] R. Placakyte, (2011), arXiv:1111.5452.

[180] V. Guzey, Talk given at Jefferson Lab on 09/16-06/17 (2009) .

[181] European Muon Collaboration, J. Aubert *et al.*, Phys. Lett. **B123**, 275 (1983).

[182] A. Bodek and J. Ritchie, Phys. Rev. **D23**, 1070 (1981).

[183] K. Saito and T. Uchiyama, Z. Phys. **A322**, 299 (1985).

[184] S. Cao and S. A. Bass, Phys. Rev. **C84**, 064902 (2011), arXiv:1108.5101.

[185] S. Cao, G.-Y. Qin, and S. A. Bass, J. Phys. **G40**, 085103 (2013), arXiv:1205.2396.

[186] J. Zinn-Justin, Chapter 4 of Quantum Field Theory and Critical Phenomena (Oxford University Press, 2002) .

[187] J. Dunkel and P. Hnggi, Phys. Rept. **471**, 1 (2009).

[188] H. Song and U. W. Heinz, Phys. Rev. **C77**, 064901 (2008), arXiv:0712.3715.

[189] K. Geiger and B. Müller, Nucl. Phys. **B369**, 600 (1992).

[190] S. A. Bass, B. Müller, and D. K. Srivastava, Phys. Lett. **B551**, 277 (2003), nucl-th/0207042.

[191] M. Bowler, Z. Phys. **C11**, 169 (1981).

[192] N. Armesto, M. Cacciari, A. Dainese, C. A. Salgado, and U. A. Wiedemann, Phys. Lett. **B637**, 362 (2006), arXiv:hep-ph/0511257.

[193] S. Cao, Y. Huang, G.-Y. Qin, and S. A. Bass, (2014), arXiv:1404.3139.

[194] E. Wang and X.-N. Wang, Phys. Rev. Lett. **87**, 142301 (2001), arXiv:nucl-th/0106043.

[195] G.-Y. Qin and B. Müller, Phys. Rev. **C85**, 061901 (2012), arXiv:1109.5961.

[196] Z. Qiu and U. Heinz, Phys. Lett. **B717**, 261 (2012), arXiv:1208.1200.

[197] L. Pang, Q. Wang, and X.-N. Wang, Nucl. Phys. **A904-905**, 811c (2013), arXiv:1211.1570.

[198] K. Dusling and D. Teaney, Phys. Rev. **C77**, 034905 (2008), arXiv:0710.5932.

[199] R. P. G. Andrade, J. Noronha, and G. S. Denicol, (2014), arXiv:1403.1789.

[200] R. Rodriguez, R. J. Fries, and E. Ramirez, Phys. Lett. **B693**, 108 (2010), arXiv:1005.3567.

[201] T. Renk, H. Holopainen, J. Auvinen, and K. J. Eskola, Phys. Rev. **C85**, 044915 (2012), arXiv:1105.2647.

[202] H. Zhang, T. Song, and C. M. Ko, Phys. Rev. **C87**, 054902 (2013), arXiv:1208.2980.

[203] B. Andersson, G. Gustafson, and B. Soderberg, Z. Phys. **C20**, 317 (1983).

[204] C. Peterson, D. Schlatter, I. Schmitt, and P. M. Zerwas, Phys. Rev. **D27**, 105 (1983).

[205] C.-W. Hwang, Eur. Phys. J. **C23**, 585 (2002), arXiv:hep-ph/0112237.

[206] Y. Oh and C. M. Ko, Phys. Rev. **C76**, 054910 (2007), arXiv:0707.3332.

[207] U. W. Heinz, p. 165 (2004), arXiv:hep-ph/0407360.

[208] R. S. Bhalerao, A. Jaiswal, S. Pal, and V. Sreekanth, Phys. Rev. **C89**, 054903 (2014), arXiv:1312.1864.

[209] G.-J. Mao, Z. Li, and Y. Zhuo, Phys. Rev. **C53**, 2933 (1996).

[210] G.-J. Mao, L. Neise, H. Stoecker, W. Greiner, and Z.-X. Li, Phys. Rev. **C57**, 1938 (1998), arXiv:nucl-th/9709047.

[211] S. Cao, G.-Y. Qin, S. A. Bass, and B. Müller, J. Phys. Conf. Ser. **446**, 012035 (2013).

[212] S. Cao, G.-Y. Qin, and S. A. Bass, (2014), arXiv:1404.1081.

[213] S. Cao, G.-Y. Qin, and S. A. Bass, (2014), arXiv:1408.0503.

[214] S. Caron-Huot and G. D. Moore, Phys. Rev. Lett. **100**, 052301 (2008), arXiv:0708.4232.

[215] H. van Hees and R. Rapp, Phys. Rev. **C71**, 034907 (2005), nucl-th/0412015.

[216] J. Casalderrey-Solana and D. Teaney, Phys. Rev. **D74**, 085012 (2006), arXiv:hep-ph/0605199.

[217] H. Ding *et al.*, J. Phys **G38**, 124070 (2011), arXiv:1107.0311.

[218] X. Zhu, N. Xu, and P. Zhuang, Phys. Rev. Lett. **100**, 152301 (2008), arXiv:0709.0157.

[219] LHCb Collaboration, R. Aaij *et al.*, JHEP **1206**, 141 (2012), arXiv:1205.0975.

[220] E. Pereira, Talk presented at Hard Probes 2013 Conference .

[221] J. Huang, Z.-B. Kang, and I. Vitev, Phys. Lett. **B726**, 251 (2013), arXiv:1306.0909.

[222] J. Zinn-Justin, Chapter 1 of Quantum Field Theory and Critical Phenomena (Oxford University Press, 2002) .

[223] S. Cao, G.-Y. Qin, and S. A. Bass, J. Phys. Conf. Ser. **420**, 012022 (2013), arXiv:1209.5405.

Biography

Shanshan Cao was born in Nanjing, China on April 15, 1987. He got his high school education at Nanjing Foreign Language School from September 1999 to June 2005. After that, he was admitted to the Kuang Yaming Hornors School, Nanjing University, where he received his Bachelor Degree of Science (physics major) in June, 2009. In August 2009, he entered the Graduate Program at Duke University and joined the QCD Theory Group in the Department of Physics, working with Prof. Steffen Bass. He passed the preliminary exam and became a doctoral candidate in February, 2012, and is expected to receive the Doctor Degree of Philosophy in Fall 2014. As a graduate student, he has published articles listed in [184, 185, 134, 223, 107, 211, 212, 193, 213].